NEAR MILLIMETER WAVE CMOS RECEIVER AND TRANSMITTER

by

Qian Zhong

APPROVED BY SUPERVISORY COMMITTEE:

_____

Dr. Kenneth K. O, Chair

_____

Dr. Wooyeol Choi

_____

Dr. Rashaunda M. Henderson

_____

Dr. Mark Lee

To my parents and fiancée for their love and support

NEAR MILLIMETER WAVE CMOS RECEIVER AND TRANSMITTER

by

QIAN ZHONG, BSEE

DISSERTATION

Presented to the Faculty of

The University of Texas at Dallas

in Partial Fulfillment

of the Requirements

for the Degree of

DOCTOR OF PHILOSOPHY IN

ELECTRICAL ENGINEERING

THE UNIVERSITY OF TEXAS AT DALLAS

August 2018

ACKNOWLEDGMENTS

NEAR MILLIMETER WAVE CMOS RECEIVER AND TRANSMITTER

Qian Zhong, PhD
The University of Texas at Dallas, 2018

Supervising Professor: Kenneth K. O

Electromagnetic waves in the millimeter (mm) and sub-millimeter wave (sub-mm) frequency ranges have caught a lot of attention. The waves at these frequencies can interact with gas molecules possessing dipole moments and change their rotational states. This phenomenon can be utilized for fast scan rotational spectroscopy to detect gas molecules and measure their concentrations. Rotational spectrometers have a wide range of applications including indoor air quality monitoring, detection of harmful gas leaks, breath analyses for monitoring bodily conditions and many others. At the mm and sub-mm wave frequencies, a large bandwidth is available for extremely high data rate communication. Communication over a dielectric waveguide at these frequencies with a loss less than 10dB/m has been proposed to mitigate the complexity of communication over copper wires as well as the integration challenges for optical communication that are being developed to meet the ever-increasing bandwidth demand.

The advances of complementary metal-oxide-semiconductor (CMOS) technology have enabled the implementation of mm-wave and sub-mm wave frequency circuits with reduced cost and increased system integration and complexity. A receiver with a radio frequency front-end bandwidth of 95 GHz and noise figure of 13.9 -19 dB for a rotational spectrometer is demonstrated

in 65-nm CMOS. In addition, a 300-GHz QPSK transmitter with a 30-Gbps data rate is demonstrated that consumes 180mW for dielectric waveguide communication.

The system level tradeoff of a receiver for rotational spectroscopy is first analyzed with a focus on the noise mechanism. A detailed signal-noise interaction derivation due to a 2nd order non-linearity is presented and signal to noise ratio degradation is shown for different modulation scenarios. A receiver front-end using a broadband antenna backed by a phase compensated artificial magnetic conductor reflector, a floating body antiparallel diode pair as the mixing device and a multi-mode isolated broadband hybrid is demonstrated. The receiver also includes an on-chip LO generator using frequency multipliers and capacitive neutralized power amplifiers, an IF cascode low noise amplifier and a baseband power detector. The receiver exhibits a responsivity of 400-1200 kV/W and noise equivalent power of 0.4 to 1.2 pW/√Hz at 225 to 280 GHz. Detection of Ethanol, Propionitrile (EtCN), Acetonitrile (CH_3CN) and Acetone in a mixture is demonstrated using the receiver in a rotational spectroscopy setup. This is the first demonstration that a CMOS receiver can be used for rotational spectroscopy and that a CMOS integrated circuit can support an existing application at frequencies above 200 GHz.

A heterodyne transmitter with a current mode logic modulator, a multi-stage constant gain and group delay wideband data buffer using coupled resonators, a double balance passive up-conversion mixer using a Marchand balun which acts as built-in LO spur traps, and a quadrature oscillator with quadrature calibration are demonstrated. The transmitter generates the required RF power for the system of -6 dBm and supports a maximum data rate of 30Gbps while consuming 180mW of power resulting in an energy efficiency of 6 pJ/bit. The single channel data rate is almost 2X higher than that of the previously reported CMOS QPSK transmitter and the energy

efficiency is among the highest of CMOS QPSK transmitters operating at the similar frequency

range.

TABLE OF CONTENTS

LIST OF FIGURES

LIST OF TABLES

CHAPTER 1

INTRODUCTION

Electromagnetic waves in the millimeter (mm) and sub-millimeter wave (sub-mm) frequency ranges have received a lot of attention. The waves at these frequencies can interact with gas molecules with dipole moments and change their rotational states. This phenomenon can be utilized for fast scan rotational spectroscopy to detect gas molecules and measure their concentrations. The rotational spectrometers have a wide range of applications including indoor air quality monitoring, detection of harmful gas leaks, breath analyses for monitoring bodily conditions and many others. At the mm and sub-mm wave frequencies, a large bandwidth is available for extremely high data rate communication. Communication over a dielectric waveguide at mm and sub-mm wave frequencies with a loss less than 10dB/m has been proposed to mitigate the complexity of communication over copper wires as well as the integration challenges for optical communication that are being developed to meet the ever-increasing bandwidth demand. The advances of complementary metal-oxide semiconductor (CMOS) technology have enabled the implementation of mm-wave and sub-mm wave frequency circuits with reduced cost, and increased system integration and complexity.

1.1 Motivation for Rotational Spectroscopy

With the increasing health care cost and the world population, there are increasing needs to provide affordable and reliable preventitive care and early diagnoses. A key for this is to routinely and frequently monitor health. To address this, the ubiquitous healthcare (UHC) [1] is introduced. It aims to find a way to provide healthcare services that are available to everyone,

independent of time and location. This requires building a personal sensor and a diagnosis system which can partially or even fully replace the role of a doctor for diagnoses and chronic disease monitoring.

In recent years, a wide variety of personal monitoring devices has become available. FitBit^{TM}, Apple Watch^{TM}, and Nike+Fuleband^{TM} are some examples. These devices use the electronic technology to help track multiple key health-related data. For example, pulse oximeters/skin electrodes are used to monitor heart rates, accelerometers are used to track body movements, and piezo-resistive sensors are used to track respiration rates. However, the data are rudimentary and it is difficult to link the data to diseases. It is most appropriate to categorize these devices as fitness monitors instead of health monitors.

To fully realize UHC vision, the devices should be able to collect a more complete set of direct disease-related data and analyze them. Many types of data (e.g. heart rate, temperature, movement) can be collected. However, the ability to routinely collect health-related chemical data critical for reliable diagnoses is not available. Therefore, making health-related chemical detecting affordable chemical sensors is a key to realize the UHC vision.

1.2 Spectrometer System for Gas and Human Breathe Analysis

Exhaled breath analyses are becoming an increasingly important non-invasive diagnostic method that can be used to evaluate health status and diagnose diseases. As a person breathes out, thousands of molecules which can be put into three general categories are expelled [2] :1) inorganic gases (e.g., NO, CO_2, CO and others), 2) volatile organic compounds (VOCs) (e.g., isoprene, ethane, pentane, acetone and others), and 3) some of the other typical non-volatile substances (e.g., isoprostanes, peroxynitrite, cytokines, nitrogen, and others). Some of these gas molecules are

important biomarkers that can be directly linked to diseases or disorders. For example, exhaled NO is a key biomarker for sorting out normal persons with respiratory symptoms from asymptomatic positive asthmatic patients (with 90% specificity) [3] and exhaled acetone concentration levels can be related to the metabolic activity of Type-I diabetes patients [2]. Although various methods [4] have been developed to support breath analysis, the existing methods such as gas chromatography (GC), proton-transfer reaction-mass spectrometry (PTR-MS), and selected ion flow tube-mass spectrometry (SIFT-MS) that can analyze a variety of gases, are expensive and difficult or requiring professional knowledge to operate. In addition, most of these techniques lack the specificity to unambiguously identify chemical compounds.

More recently, with the development of laser technology, laser spectroscopy has become a promising candidate for breath analysis as this method does not need any special chemical treatment to breath samples and has sufficiently high specificity for some chemicals. However, its ability to detect a variety of compounds largely depends on the availability of wideband lasers. The system is still bulky and expensive.

1.3 Sub-millimeter Wave Rotational Spectroscopy

Laser spectroscopy is based on absorption of light by gas molecule. Millimeter and sub-millimeter (sub-mm) wave rotational spectroscopy is built on the same concept but at much lower frequencies usually ranging from 100 GHz to 10 THz. At this frequency range, gas molecule rotational energy transitions occur. As shown in Figure 1.3(a) [5], molecules rotate around a rotational axis. The rotational energy is quantized, which means that only certain energy levels are

Figure 1.1   (a) Gas Chromatography (picture: www.wikipedia.org/mass spectrometry), (b) Flow tube-mass spectrometry (picture: www.syft.com/sift-ms/).

permitted. Incident electromagnetic (EM) waves can excite molecules to absorb waves and change their rotational states provided they have an electric dipole moment. As shown in Figure 1.3(b), when an incoming EM radiation is incident on a gas molecule, the electric field of EM wave exerts a torque on the molecule and changes its rotational state. Because of the quantized rotational energy levels of gas molecules, a given type of molecule only absorbs EM waves with certain energy or specific frequencies. These frequencies are different for different kinds of molecules. Therefore, by identifying the frequencies of the EM wave that are absorbed, gas molecules are identified. An example of absorption versus frequency is shown in Figure 1.2(a) [3]. The spikes at different frequencies are known as power absorption lines. The spectrum of gas molecules is redundant and completely resolvable which lead to almost absolute specificity. A block diagram of the rotational spectrometer demonstrated by a research team from the Ohio State University is
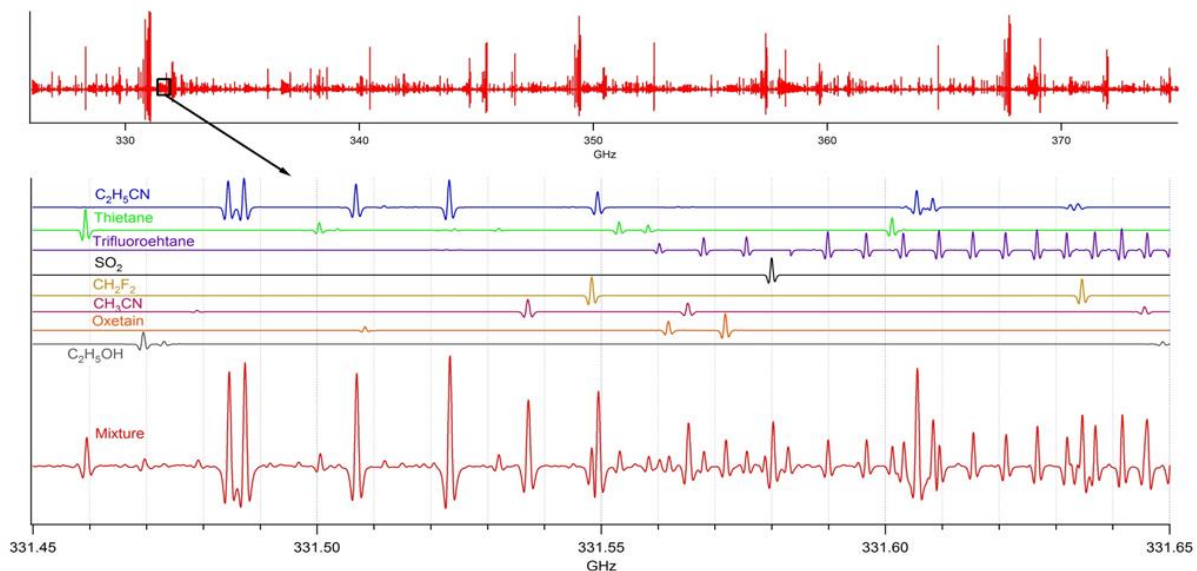
(a)
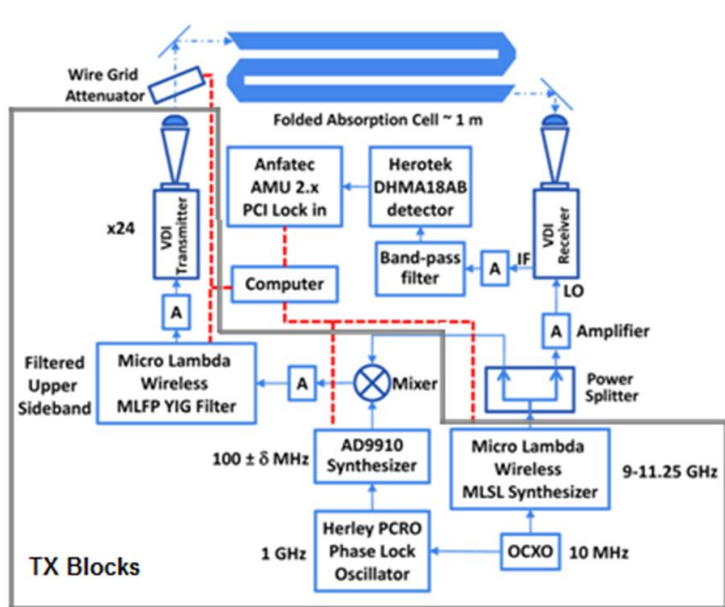
(b)

Figure 1.2   (a) Rotational absorption spectrum [3], (b) rotational spectrometer system [3].
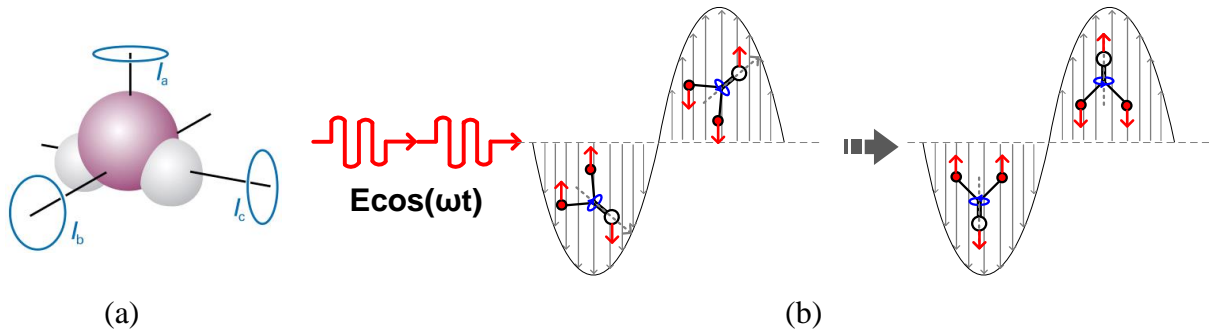
Figure 1.3　(a) Rotation of a molecule along x,y,z axes [5],　(b) molecule interaction with EM radiation.

shown in Figure 1.2(b). The architecture is based on a heterodyne transceiver and is built with commercially available discrete components. A 1-m long folded absorption cell holds the gas molecules under test. A pumping system lowers the pressure in the absorption cell down to a mTorr level. The demonstration of spectrometer system is a breakthrough in many ways. Firstly, the scan is performed electronically. With the help of modern computation and signal processing techniques, the scan can be fast compared to all the previously mentioned techniques. Secondly, it is not hard for modern frequency synthesizers to have a sub-Hz resolution even at mm-wave frequencies. The ultra-fine frequency scan step enables capturing closely spaced lines of different gas molecules.

1.4 Motivation for Dielectric Wave Guide Communication

According to a May 2013 report on disruptive technologies [6], the top four technologies are likely to have a significant economic impact by 2025: 1) mobile internet, 2) automation of knowledge work, 3) the internet of things, and 4) cloud computing. All these need data centers which are capable of processing huge amounts of data generated. Communication in data centers is either through optical fiber based systems or through copper electrical links on printed circuit

boards. With an estimated over 1000x data capacity increase over the next five years, the data rate will reach the point at which the electrical link on printed circuit board cannot support the required data rate. Although an optical link can support the high data rate, the complicated optic-electronic interface makes it not a cost-effective solution.

Radio frequency (RF) communication through a dielectric/plastic waveguide is an interesting and promising alternative to optical and electrical links [7],[8],[9]. First, it operates at the millimeter wave or even terahertz frequency range where large bandwidths are available. Its data rate can surpass that of electrical links on printed circuit board. Secondly, compared to optical systems, it can be integrated into current available electronic systems without additional optical devices. More importantly, the transmission medium is made of inexpensive plastic.

1.5 Dielectric Waveguide Communication System

Communication over a long distance at millimeter wave (mm-wave) frequencies is challenging. Firstly, energy efficient electronics are challenging to realize. Secondly, traditional metallic waveguides or coaxial lines suffer from high skin depth loss. Therefore, there is a need to develop a new low-loss waveguide structure which can operate in the mm-wave frequency range. In 1969, researchers from Bell Labs proposed a waveguide structure [10] based on a dielectric rod with a rectangular cross-section, surrounded by several layers of dielectric cladding with smaller refractive indices (Figure 1.4). Due to its high dielectric constant, this waveguide can confine mm-wave signals, resulting mostly one-dimensional transmission. Compared to the free space three-dimensional radiation, the low loss advantage of dielectric waveguide resulting from field confinement is clear. Moreover, compared to electrical copper electrical links, the dielectric waveguide has a larger bandwidth due to lower loss. In 1989, researchers from the University of

California Los Angeles (UCLA) further refined the structure [11] and introduced a new family of ultra-low-loss dielectric ribbon based waveguide structures which provide attenuation constants that are more than 100 times less than that of a conventional dielectric or a metallic waveguide [12]. As shown in Figure 1.5, from 30 GHz to 1 THz, the proposed silicon ribbon based interconnect has attenuation factors of 0.01 dB/m to 0.5 dB/m, which are significantly less than those of metallic based waveguide structures. These low loss dielectric waveguides open the door to low-loss mm-wave long-range communication.

With the rapid development of mm-wave CMOS integrated circuits, implementation of a complete transmit-receive link using a dielectric waveguide has become feasible. Many research groups started to exploit the unique characteristics of the dielectric waveguides for the next generation of high-speed communication. In 2011, Sony together with California Institute of Technology demonstrated a full duplex serial link with 12.5+12.5 Gb/s data rates in two mm-wave frequency bands at 57GHz and 80GHz, achieving a total data rate of 25 Gb/s through a single transmission medium without using an equalization technique [13].

The circuit diagram is shown in Figure 1.6(a). Two transmitter (TX) and receiver (RX) sets are designed using a 40-nm CMOS process. 5mmx5mm dipole antennas are formed on a printed circuit board (PCB) as chip-to-waveguide launches. A 12-cm waveguide made of plastic is used as the transmitting medium. Not only the data rate of this link easily matched the state-of-art electrical high-speed link at that time, but also the chip interface and link connectivity were much more simplified compared to high speed electrical and optical links. Figure 1.6(a) shows a setup for demonstration of uncompressed real-time video transmission using this chipset. In 2013, a research team of UCLA demonstrated a similar link in [14]. As shown in Figure 1.6(b), TX and

RX are connected by a plastic tube to form a link. Off-chip antennas are used to excite the waves in the dielectric tube. Unlike that in [13], the tube has an air core, and a special coupler is designed to ensure proper transition to the hollow tube. This communication system was used to demonstrate a data rate of 3.3 Gb/s. In 2015, researchers from KU Leuven (KUL) demonstrated another link using a dielectric waveguide [15]. As shown in Figure 1.7, they investigated the use of both off-chip antennas (bond-wire antenna) and on-chip antennas (collinear broadside dipole) to excite the dielectric waveguide and detect the waves in the dielectric waveguide. At 120-GHz carrier frequency, they achieved a data rate of 12.7 Gb/s.

Though dielectric waveguide links have been demonstrated many times in literature, the communication systems used are all quite rudimentary. All of the previous works used simple and bandwidth-inefficient modulation schemes, for example, on-off keying (OOK) in [13],[14]. Amplitude shift keying (ASK) in [15] does not take advantage of the broadband capability of dielectric waveguides and the carrier frequencies of these systems reside at the lower end of sub-millimeter wave spectrum making a high data rate difficult to support. To make a dielectric
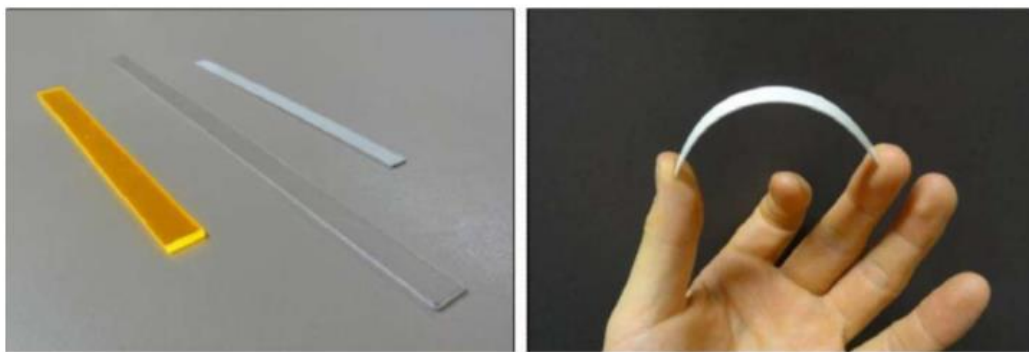
Figure 1.4   Plastic dielectric waveguide [13] .

9

waveguide communication system rival the performance of commercial optical links, higher carrier frequency, and more complex modulation scheme must be employed.

1.6 Scope and Organization of the Dissertation

This dissertation focuses on the detailed design of 200-300 GHz receiver for rotational spectroscopy and 315-GHz transmitter for dielectric waveguide communication. The rest of the thesis is organized as follows. Chapter 2 discusses a 200-300 GHz receiver for rotational spectroscopy including its circuit building blocks and the final demonstration with a transmitter in a complete rotational spectroscopy setup. Chapter 3 presents the detailed design and demonstration of a transmitter for dielectric waveguide communication. It starts with an introduction to minimum shift keying (MSK) modulation and MSK transmitter architecture. Then each circuit building blocks are discussed in detail. Finally, simulation and measurement results of the entire system are presented. Chapter 4 summaries the works and suggests future works.
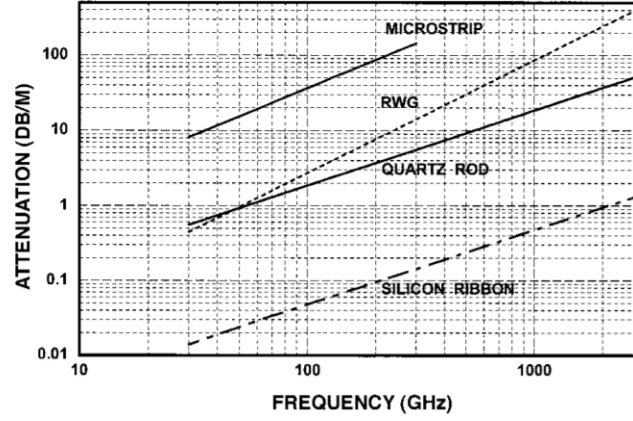
Figure 1.5   Performance comparison among several waveguide structures [12].

(a)   (b)
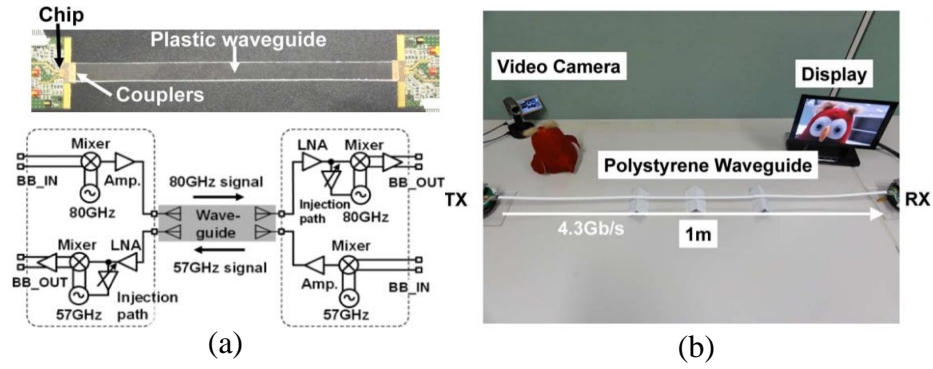
Figure 1.6   (a) TX and RX circuit diagram [13], (b) uncompressed video transmission [13].

(a)   (b)
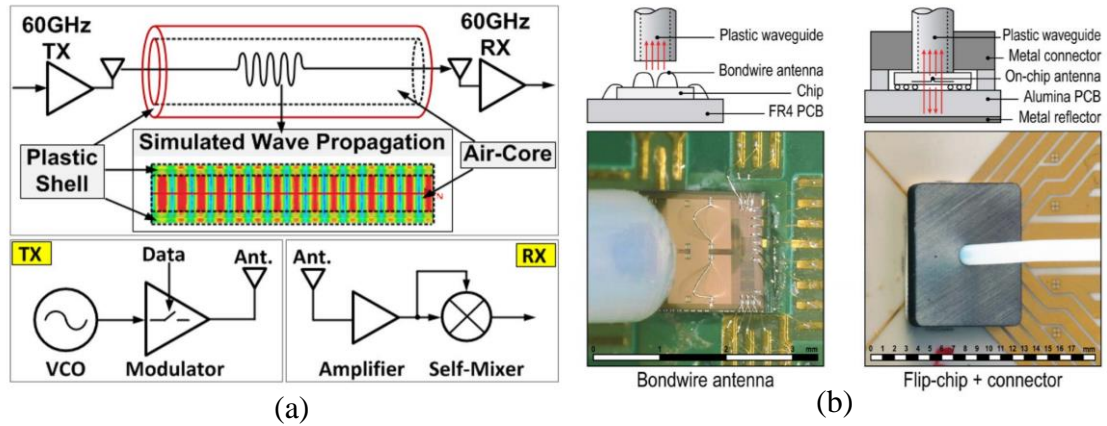
Figure 1.7   (a) UCLA system [14], (b) KUL system [15].

CHAPTER 2

DEMONSTRATION OF 200-300 GHZ RECEIVER FOR ROTATIONAL

SPECTROSCOPY

2.1 Introduction

Electromagnetic waves in the millimeter and sub-millimeter wave frequency ranges can be utilized for fast scan rotational spectroscopy to detect gas molecules and measure their concentrations [3]. The principle behind rotational spectroscopy is depicted in Figure 2.1. When electromagnetic-waves within a certain frequency range are radiated into an absorption cell containing gas molecules, the waves change the rotational state of gas molecules and a part of its power is lost in this interaction. These results in a drop of power picked up at the receiver or a line. By sweeping the transmitter output frequency, the frequency response of absorption cell is measured. Looking at the frequencies the waves are absorbed and the depth of absorption line, the identity of the molecule and its concentration are determined. In general, the spectrometer system is electronically equivalent to a communication system with a communication channel modeled
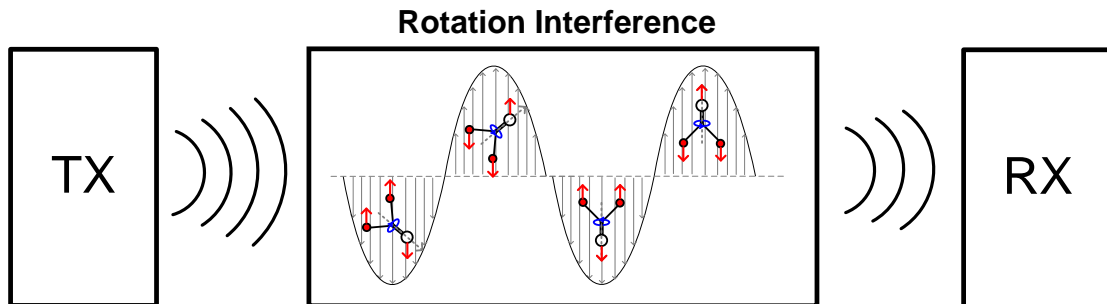
Figure 2.1   Conceptual diagram of spectrometer system
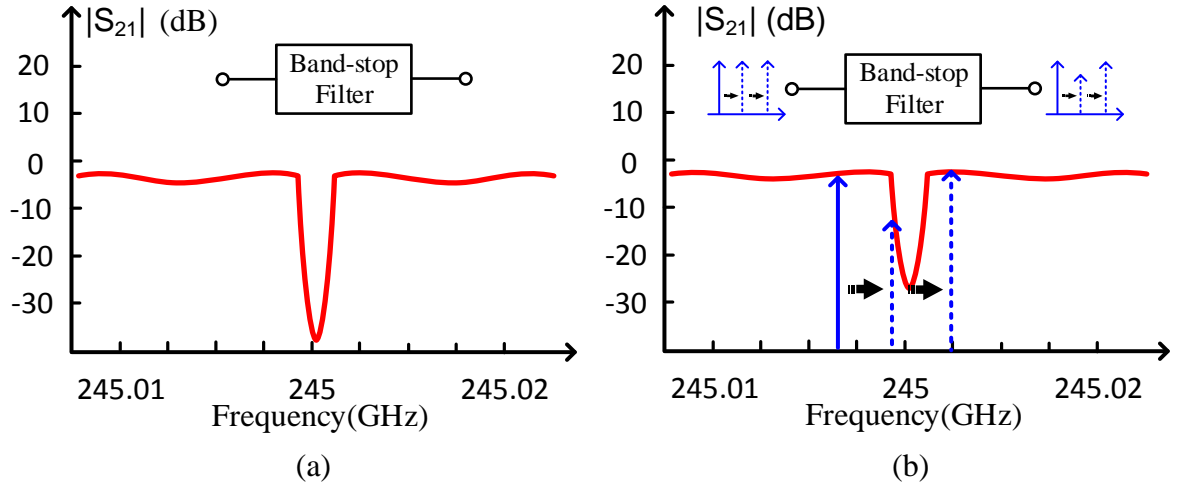
Figure 2.2   (a) Gas tube represented as band stop filters (b) frequency sweeping over a band stop filter to emulate spectrometer frequency response

with multiple band-stop filters. As shown in Figure 2.2(a), the gas molecule measuring process can be analogous to finding the band-stop filter "dip" from the spectrum. Figure 2.2(b) shows the dynamic process of frequency sweeping across the stop band of the band-stop filter to find the line.

Presently, rotational spectrometers utilize a frequency multiplier chain driven by a signal a synthesizer to generate the transmitted signal, and a diode based sub-harmonic mixer followed by an amplifier and a diode amplitude detector to measure the received signal amplitude [3]. The frequency multiplier chain, mixer, and diode are fabricated using compound semiconductor technologies [3]. Recently, rotational spectroscopy at 240-250 GHz has been demonstrated using SiGe HBT based RF front-ends for transmission and reception [16]. Additionally, a 210-to-305 GHz RF front-end for rotational spectroscopy fabricated in 65-nm CMOS has been reported [17]. The front-end included a sub-harmonic mixer, an on-chip antenna, and an intermediate frequency amplifier.

13

2.2 Spectrometer System Noise Analysis

Based on the rotational spectrometer system described in Section 2.1, a rotational spectrometer receiver is mainly doing the job of monitoring the power of waves from the gas molecule cell over a large bandwidth. In that sense, it is an amplitude modulation (AM) receiver. There are two general categories to implement an AM receiver, coherent detection, and noncoherent detection. For incoherent detection, the receiver operates without a local oscillator (LO). In its simplest form, an incoherent receiver would be just a rectifier implemented with a zero-biased Schottky Barrier Diode (SBD). For coherent detection, the receiver uses a synchronized local oscillator to perform the down-conversion and demodulate the carrier. Although simple to implement, incoherent detection usually suffers from poor noise performance compared to coherent detection. To choose the proper architecture, the noise mechanisms in a rotational spectrometer and the corresponding noise requirement for the receiver must first be understood.

2.2.1 Phase Locked Loop (PLL) Phase Noise Effect

The PLL phase noise plays a critical role in determining the final noise behavior of spectrometer. As shown in Section 2.1, and Figure 2.1 and Figure 2.2, the spectrum is constructed using frequency domain scanning using a PLL. Sweeping with a non-ideal PLL is shown in Figure 2.3. Instead of a single sharp tone, the sweeping tone shows a significant frequency span due to the phase noise. This will smear the absorption line shape and the fine details and transitions of absorption lines can be buried in the phase noise and no longer be recoverable. Secondly, in a case where two lines are extremely close to each other, excessive phase noise when sweeping will make

them indistinguishable, resulting in loss of a line. For incoherent detection, the transmitter phase noise must be taken care of properly. For coherent detection, the local oscillators of transmitter and receiver are synchronized to the same reference frequency. The degradation due to PLL phase noise can be mitigated since part of phase noise that comes from the reference signal of RX and TX are essentially correlated. The requirements of PLL phase noise is still stringent even for coherent detection because the two LOs in TX and RX are still generating uncorrelated phase noise that cannot be canceled.

| (a) | (b) |
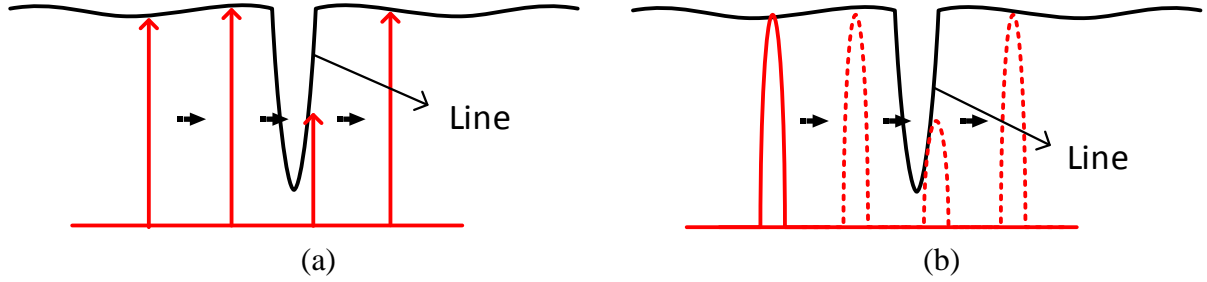
Figure 2.3   (a) Ideal sweeping, (b) non-ideal sweeping with phase noise

2.2.2   Townes Noise

A major source of noise in a receiver using an amplitude detection is Townes noise. This noise is named after C. H .Townes [18]. The Townes noise process can be understood as follows, when a transmitting a signal with an amplitude of V and power of P is present in a waveguide with impedance Z, then

$$V^2 = 2ZP. \tag{2.1}$$

The noise fluctuation with an amplitude V_n is

$$V_n^2 = 4ZkT\Delta f. \tag{2.2}$$

when k is the Boltzmann constant, T is the temperature in degree, and Δf is the bandwidth. The total power in this waveguide is [18]

$$\frac{(V \pm V_n)^2}{2Z} = P \pm 2\sqrt{2kTP\Delta f} + 2kT\Delta f \tag{2.3}$$

The cross term in Eqn. (2.3) is the geometrical average between the transmitted signal power P and thermal noise power. In a conventional communication system, this term can be safely disregarded because in these systems, the received power is tiny and this small amount of power is measured against background noise. However, in a spectrometer, the transmitted/received power is large which makes the cross term not negligible and the signal measured is a small fraction of this large power and the noise induced by this large signal cannot be neglected. Although the conclusion is verified, the derivation is misleading in many ways. A more rigorous derivation of this noise mechanism is done by first considering the detector and mathematical model shown in Figure 2.4, the input signal V(t) to the detector is defined in a sum of a sinusoidal signal V_s(t) and noise voltage V_n(t) as shown in Eqn. (2.4).

$$
\begin{aligned}
V_s(t) &= V_0 \sin(\omega_s t), \\
\overline{V_n^2} &= kTR_s\Delta f_i, \\
V(t) &= V_n(t) + V_s(t).
\end{aligned}
\tag{2.4}
$$

It is assumed that the noise is generated from source resistance R_s and that the noise power delivered from the source to the detector is the available power (e.g. the detector and source are power matched). The input bandwidth of the detector is band limited to Δf_i using an ideal bandpass filter and the output is band limited to Δf_o using an ideal low pass filter. The input sinusoidal signal has an amplitude of V_0 and frequency in radians of ω_s. The noise is Gaussian white noise.
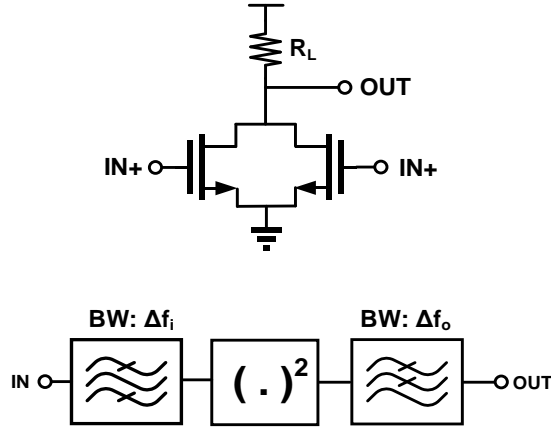
Figure 2.4   Amplitude detector transistor model and mathematical model

V_o is RMS voltage. The detector is assumed to be an ideal square law device and the detector itself does not generate noise. The gain of the detector is

$$\alpha = a_2[A/V^2]R_L[\Omega] = a_2 R_L[1/V],\tag{2.5}$$

where a_2 is the 2nd order non-linear coefficient for the current. In MOS transistors, a_2 can be written as

$$a_2 \approx \mu_0 C_{ox}\frac{W}{L}\left[1-3\left(\frac{\mu_0}{2v_{sat}L}+\theta\right)\left(V_{GS0}-V_{TH}\right)\right],\tag{2.6}$$

where μ_0 is the carrier mobility, V_{TH} is the threshold voltage, W and L are the channel width and length, and C_{ox} is the oxide capacitance per unit gate area. R_L in Eqn. (2.5) is the total detector loading resistance. The detector output voltage is thus

$$V_{\mathrm{det\_out}}(t) = \alpha V^2(t) = \alpha(V_n(t)+V_s(t))^2.\tag{2.7}$$

17

Eqn. (2.7) provides little information about the statistical characteristics of noise. For the statistical characteristics of detector output, a power spectral density (PSD) is needed. To compute the PSD of detector output, autocorrelation is first calculated (Eqn. (2.8)).

$$
\begin{aligned}
R_{V_{det\_out}V_{det\_out}}(\tau) = \alpha^2 \Big\{ & E(V_s^2(t)V_s^2(t+\tau)) + E(V_n^2(t)V_s^2(t+\tau)) \\
& + E(V_s^2(t)V_n^2(t+\tau)) + E(V_n^2(t)V_n^2(t+\tau)) \\
& + 2E(V_n(t)V_n^2(t+\tau)V_s(t)) \\
& + 2E(V_s^2(t)V_s(t+\tau)V_n(t+\tau)) \\
& + 2E(V_n^2(t)V_s(t+\tau)V_n(t+\tau)) \\
& + 2E(V_n(t)V_s^2(t+\tau)V_s(t)) \\
& + 4E(V_s(t)V_s(t+\tau)V_n(t)V_n(t+\tau)) \Big\}.
\end{aligned}
\tag{2.8}
$$

Because the signal and noise are independent,

$$
\begin{aligned}
E(V_n(t)V_s^2(t+\tau)V_s(t)) &= E(V_n(t))E(V_s^2(t+\tau)V_s(t)), \\
E(V_s^2(t)V_s(t+\tau)V_n(t+\tau)) &= E(V_s^2(t)V_s(t+\tau))E(V_n(t+\tau)).
\end{aligned}
\tag{2.9}
$$

For Gaussian white noise, the mean values of terms in Eqn. (2.9) are zero, since

$$
E(V_n(t)) = E(V_n(t+\tau)) = 0.
\tag{2.10}
$$

Furthermore, the third moment of zero mean value Gaussian random process is zero and

$$
2E(V_n(t)V_n^2(t+\tau)V_s(t)) = 2E(V_n^2(t)V_s(t+\tau)V_n(t+\tau)) = 0.
\tag{2.11}
$$

Using the results in Eqns. (2.10) and (2.11), Eqn. (2.8) can be simplified to

$$
\begin{aligned}
R_{V_{det\_out}V_{det\_out}}(\tau) \approx \alpha^2 \Big\{ & E(V_s^2(t)V_s^2(t+\tau)) \\
& + E(V_n^2(t)V_n^2(t+\tau)) \\
& + E(V_n^2(t)V_s^2(t+\tau)) \\
& + E(V_s^2(t)V_n^2(t+\tau)) \\
& + 4E(V_s(t)V_s(t+\tau)V_n(t)V_n(t+\tau)) \Big\}.
\end{aligned}
\tag{2.12}
$$

Finally, the fourth moment of zero mean value Gaussian random process is

$$
\begin{aligned}
2E(V_n^{\,2}(t)V_n^{\,2}(t+\tau)) &= 2E(V_n(t)V_n(t+\tau))^2 \\
&+ E(V_n^{\,2}(t))E(V_n^{\,2}(t+\tau)).
\end{aligned}
\tag{2.13}
$$

Substituting Eqn. (2.4) into Eqn. (2.12), the autocorrelation is

$$
\begin{aligned}
R_{V_{det\_out}V_{det\_out}}(\tau) &= \alpha^2 V_0^4 \left\{ \frac{1}{4} + \frac{1}{8}\cos(2\omega_s\tau) \right\} + \alpha^2 V_0^2 R_{nn}(0) \\
&+ \alpha^2 2V_0^2 \left\{ \cos(\omega_s\tau)R_{nn}(\tau) \right\} + \alpha^2 R_{nn}(0)^2 \\
&+ 2\alpha^2 R_{nn}(\tau)R_{nn}(\tau),
\end{aligned}
\tag{2.14}
$$

where $R_{nn}(\tau)$ is the autocorrelation of input Gaussian white noise, and $R_{nn}(0)$ is $kTR_s\Delta f_i$, which becomes a deterministic quantity in the limit the integration time, τ_o goes to infinity. According to the Wiener-Khinchin relation, for a wide sense stationary process, the power spectral density is the Fourier transform of autocorrelation. The PSD by applying a Fourier transform to Eqn. (2.14) is

$$
\begin{aligned}
S_{V_{det\_out}V_{det\_out}}(f) &= \\
\alpha^2 V_0^4 &\left\{ \frac{1}{4}\delta(f) + \frac{1}{16}\delta(f-2f_s) + \frac{1}{16}\delta(f+2f_s) \right\} \\
&+ \alpha^2 2V_0^2 \left[\frac{1}{2}\delta(f-f_s) + \frac{1}{2}\delta(f+f_s) \right] * S_{nn}(f) \\
&+ \alpha^2 V_0^2 kTR_s\Delta f_i\delta(f) + \alpha^2 (kTR_s\Delta f_i)^2\delta(f) \\
&+ 2\alpha^2 S_{nn}(f) * S_{nn}(f),
\end{aligned}
\tag{2.15}
$$

Where $S_{nn}(f)$ is the PSD of Gaussian white noise with a bandwidth Δf_i around f_s. The PSD of detector output is illustrated in Figure 2.5. The power output resulting from squaring contains a signal at DC which is the desired detector output and another signal at the twice the input signal frequency. The input Gaussian white noise multiplied with the input signal generates noise

spectrum at the output that is centered around $2f_s$ and DC. This makes the input noise appear as being "up-converted" to twice of the
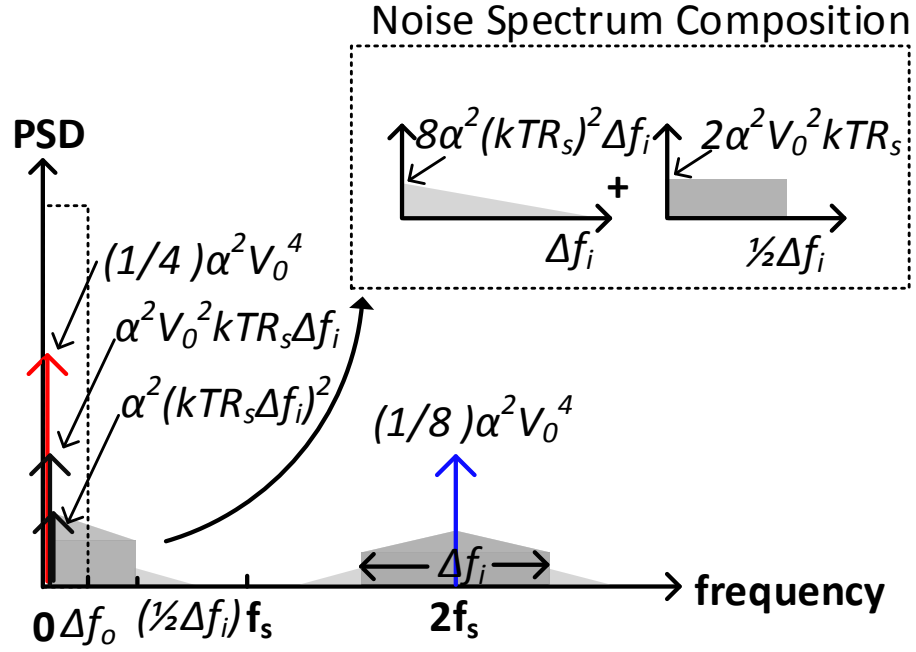
Figure 2.5   Single sideband PSD of ideal square law detector (unmodulated input)

signal frequency and "down-converted" to DC with an "amplified" spectral density equal to $2\alpha_2 V_0^2 kTR_s$. The square of detected signal and noise around DC for an integration time of τ_o with a corresponding bandwidth Δf_o are

$$\frac{1}{4}\alpha^2 V_0^4 + \alpha^2 2V_0^2 kTR_s\Delta f_o + \alpha^2 V_0^2 kTR_s\Delta f_i$$
$$+\alpha^2 (kTR_s\Delta f_i)^2 + 4\alpha^2 (kTR_s)^2 \Delta f_i\Delta f_o (2 - \frac{\Delta f_o}{\Delta f_i}).$$

(2.16)

To input refer the noise using a responsivity, the output power must be expressed in terms of voltage. The corresponding noise and signal voltages cannot be simply separated because this process involves a square root. The second term in Eqn.(2.14) is the dominant one when the signal

is much larger than the noise. The input referred noise power for the second term [V^2] in Eqn. (2.16) is

$$\frac{1}{\alpha}\sqrt{\alpha^2 2V_0^2 kTR_s \Delta f_o} = \sqrt{2V_0^2 kTR_s \Delta f_o} \tag{2.17}$$

The equivalent noise power delivered to the input is

$$\frac{1}{R_s}\sqrt{2V_0^2 kTR_s \Delta f_o} = 2\sqrt{2PkT\Delta f_o}$$

$$P = \frac{\left(\frac{1}{2}V_0\right)^2}{R_s}, \tag{2.18}$$

where P is the available power since the detector input was assumed to be matched. This expression has the exact same form as the Townes noise except that the bandwidth is Δf_o. This is a significant distinction since the input signal bandwidth, Δf_i can be on the order of GHz while the output bandwidth, Δf_o is on the order of kHz. This, more importantly, indicates an inconsistency for the formulation of Townes noise.

Another term in Eqn. (2.16) is $\alpha_2 V_0^2 kTR_s \Delta f_i = \alpha_2 V_0^2 R_{nn}(0)$ at DC. Although it is proportional to the input noise power, as mentioned, this is a deterministic term in the limit Δf_i becomes small. When V_0^2 is much smaller than $kTR_s \Delta f_i$ and Δf_i is much larger than Δf_o, $\alpha_2 V_0^2 kT\Delta f_i$ term dominates, and increasing $R_{nn}(0)$ by increasing noise or stochastic resonance can increase this DC term proportional to the input signal power.

When the signal strength of the carrier is much higher than noise, the $\alpha_2 V_0^2 R_{nn}(0)$ term is negligible since $\alpha_2 V_0^4$ will be much larger. Neglecting this and the much smaller noise square term, the signal to noise ratios at the output and input of an ideal square law detector are related by

21

$$SNR_{\text{output}} = \frac{\sqrt{\frac{1}{4}V_0^4}}{\sqrt{2V_0^2 kTR_s \Delta f_o}} = \sqrt{\frac{1}{8}\frac{V_0^2}{kTR_s \Delta f_o}}$$

$$= \frac{1}{2}\frac{\frac{V_0}{\sqrt{2}}}{\sqrt{kTR_s \Delta f_o}} = \frac{1}{2}\sqrt{\frac{\Delta f_i}{\Delta f_o}}SNR_{\text{input}}.$$

(2.19)

The output noise is from the convolution term (2nd) in Eqn. (2.15). Eqn. (2.19) suggests that

SNR_{output} can be higher than that of SNR_{input} if Δf_i is sufficiently higher than Δf_o. This is due to the

fact that the noise of the detector is not considered thus far. In Eqn. (2.19), the signal to noise ratio

degrades by 6 dB passing through an ideal square-law detector with the assumption that the input

and output bandwidths are the same. Specifically, 3 dB is due to the 3-dB difference of conversion

loss of ideal square law detector for signal and noise, and the other 3 dB results from the raised

noise floor. This signal to noise ratio degradation is systematic and cannot be alleviated by using

a low noise amplifier preceding the detector.

The above calculations and analysis are further verified in Matlab[TM]. To simplify the

simulation, the input noise source is assumed to be of a zero-mean normal distribution with a

standard deviation σ. The noise power ($kTR_s\Delta f_i = R_{nn}(0)$) is thus represented by the variance σ^2. The

total input signal can be written as

$$V(t) = V_0 \sin(\omega_s t) + \sigma \times randn,$$
$$\sigma^2 = kTR_s \Delta f,$$

(2.20)

$$\sigma \times randn \text{ has pdf of } f(V) = \frac{1}{\sigma\sqrt{2\pi}}e^{\frac{-V^2}{2\sigma^2}}.$$

All the parameters are kept the same except the input signal amplitude (2V and 0.1V),

while α and σ are set to 1 and 2.03x10^{-6} (the noise power equivalent to the thermal noise of 1Ω

resistor at 300°K with a 1-GHz bandwidth), respectively. The detector output PSD's when the

input signal amplitude is 2V and 0.1V are overlaid and shown in Figure 2.6. It is clear that the output noise floor is raised up if the input signal amplitude is raised. In this case, the noise floor increase is exactly

$$20\log(\frac{2V}{0.1V}) = 26dB. \tag{2.21}$$

Next, at the same signal and noise settings, the noise converted to DC is examined. The noise variance σ^2 is swept from 1µW to 100mW with a fixed signal amplitude $V_0=1$V and the resulting power at DC is shown in Figure 2.7. For low input noise power ($\sigma^2 =1$µW), the majority of power at DC is due to the signal and the corresponding power is 0.25W (y-intercept). With increasing input noise power (variance), the power at DC linearly increases with a slope equal to $\alpha V_0^2=1$ due to the third term in Eqn. (2.14). An expression, $0.25+1.009\sigma^2$ fits the data with 95% confidence. It is important to point out that the noise power of $\sigma^2 =10$µW in this example is high, which is only possible with a large Δf_i. In most practical systems, this effect should be negligible.

Finally, the input amplitude is swept from 0.1V to 2V with σ=2.03x10^{-6} and α=1. The expected total output noise is thus

$$2\alpha^2V_0^2kTR_s\Delta f = 2\alpha^2V_0^2\sigma^2 = 8.24\cdot10^{-12}V_0^2. \tag{2.22}$$

The simulated output noise versus input signal amplitude V_s is shown in Figure 2.8. An expression, 8.186x10^{-12} $V_s^{2.03}$, which is close to the expected fits with 95% confidence.
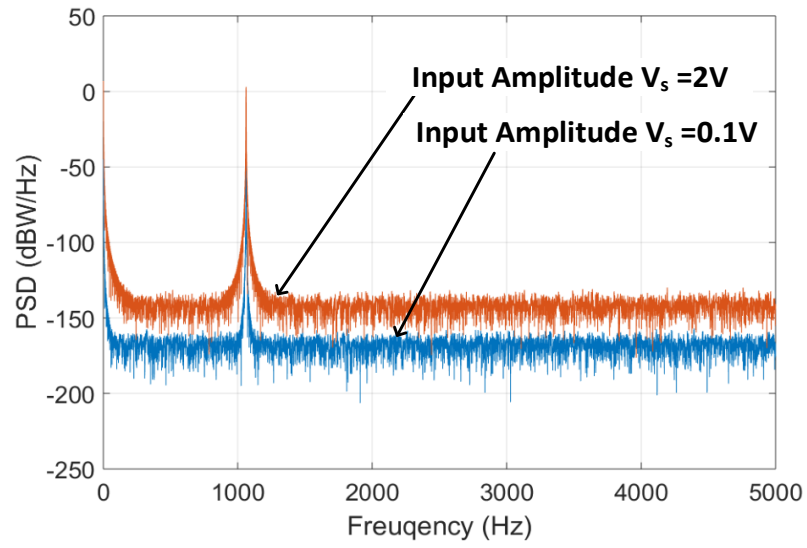
Figure 2.6   Detector output noise floor with V_s=2V and V_s=0.1V.
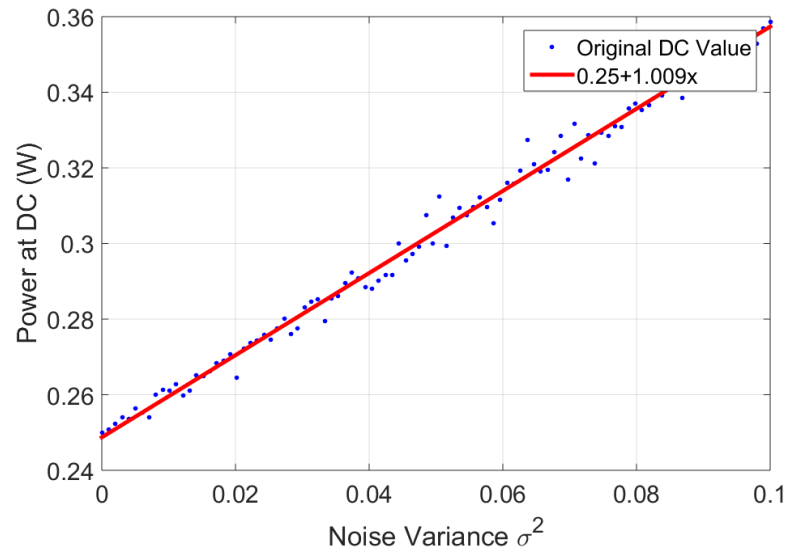
Figure 2.7   DC power versus noise variance (solid line is a fitted curve).
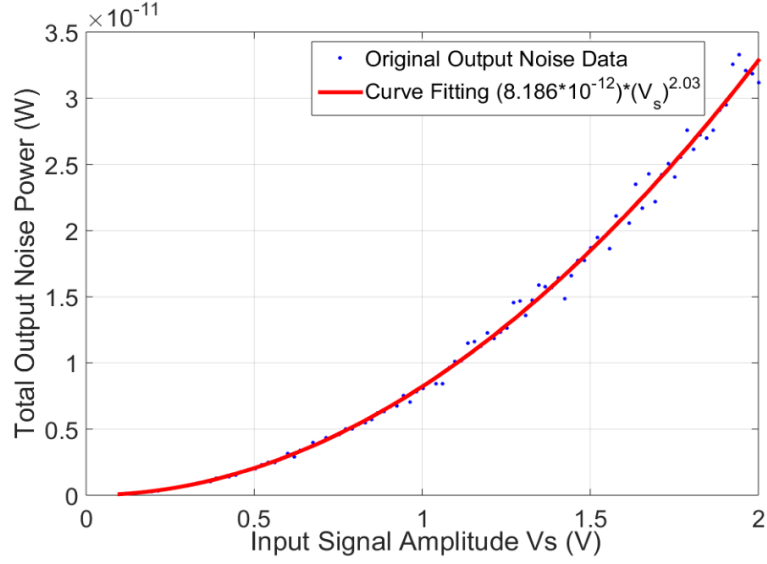
Figure 2.8   Total output noise versus input signal amplitude (solid line is a curve fitted line).

In terahertz imaging and spectroscopy systems, amplitude modulation (AM modulation) is often used to mitigate the deleterious effects of noise using lock-in techniques. In the following, the impact of AM modulation on the noise of square law detectors is discussed. The amplitude of the signal voltage term $V_s(t)$ is now time-varying as in Eqn. (2.23)

$$\overline{V_n^2} = kTR_s\Delta f,$$
$$V_s(t) = V_0(1 + m\cos(\omega_m t))\sin(\omega_s t), \qquad (2.23)$$
$$V(t) = V_n(t) + V_s(t),$$

where m is the AM modulation index (the ratio of modulation amplitude and carrier amplitude), and ω_m is the AM modulation frequency. All other parameters remain the same as that for Eqn.(2.4). The derivation is repeated with this new signal. The PSD of the ideal square law detector output with the AM modulated input is shown in Figure 2.9 and its expression is Eqn.(2.24). In this case, the output signal of interest is at the modulation frequency, f_m instead of

25

DC, and the noise converted to DC in Eqn. (2.14) can be isolated from the wanted signal at f_m.
However, the AM modulation also generates two additional "up-converted" noise sidebands
located at f_s-f_m and f_s+f_m. The detector output noise figure for the AM modulated input is Eqn.(2.25).
The signal at f_m can be extracted using a lock-in technique while rejecting the noise at DC.
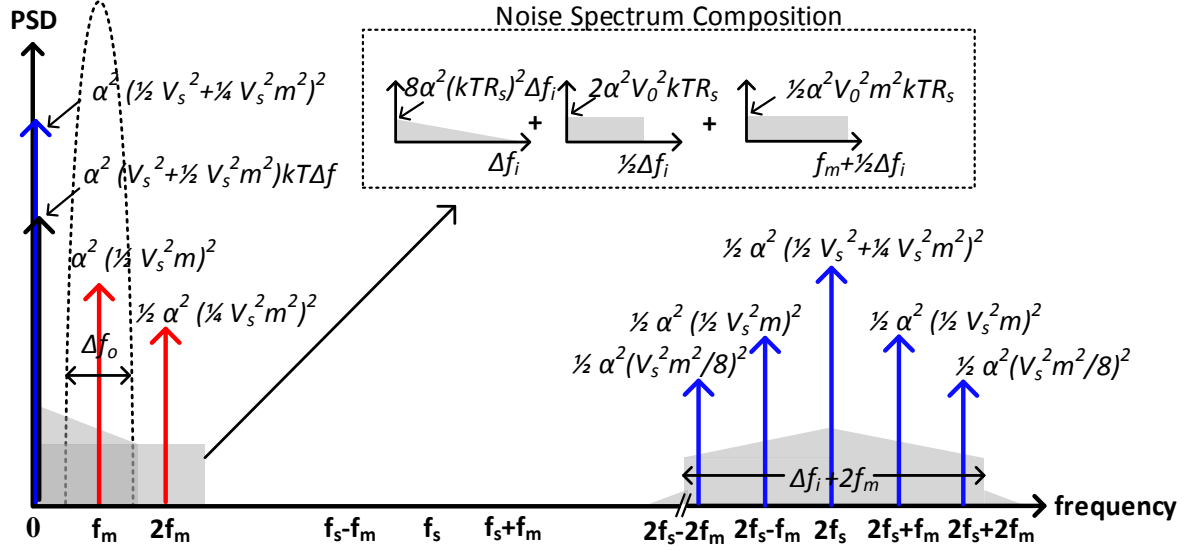
Figure 2.9   PSD of ideal square law detector output with an AM modulated the input signal

$$S_{V_{det\_out}V_{det\_out}}(f) = \alpha^2\left\{(\frac{1}{2}V_0^2 + \frac{1}{4}m^2V_0^2)^2 + (V_0^2 + \frac{1}{2}m^2V_0^2)kTR_s\Delta f\right\}\delta(f)$$

$$+\left\{2\alpha^2V_0^2\delta(f-f_s) + \frac{1}{2}\alpha^2m^2V_0^2(\delta(f-f_s-f_m)+\delta(f-f_s+f_m))\right\}*S_{nn}(f)$$

$$+\alpha^2\left\{\frac{1}{4}m^2V_0^4\delta(f-f_m) + \frac{1}{32}m^4V_0^4\delta(f-2f_m)\right\}$$

$$+\frac{1}{2}\alpha^2\left\{(\frac{1}{2}V_0^2 + \frac{1}{4}V_0^2m^2)^2\delta(f-2f_s) + \frac{1}{2}m^2V_0^4\delta(f-2f_s+f_m) + \frac{1}{2}m^2V_0^4\delta(f-2f_s-f_m)\right\}$$

$$+\frac{1}{2}\alpha^2\left\{\frac{1}{64}m^4V_0^4\delta(f-2f_s+2f_m) + \frac{1}{64}m^4V_0^4\delta(f-2f_s-2f_m)\right\} +\alpha^2(kTR_s\Delta f_i)^2\delta(f)+2\alpha^2S_{nn}(f)*S_{nn}(f)$$

$$(2.24)$$

$$SNR_{output\_AM} = \frac{\sqrt{\frac{1}{2}V_0^4 m^2}}{\sqrt{\frac{1}{2}V_0^2 m^2 kTR_s\Delta f + 2V_0^2 kTR_s\Delta f}}$$

$$= \sqrt{\frac{m^2}{(\frac{1}{2}m^2 + 2)(m^2 + 1)}\frac{\frac{1}{2}V_0^2(1+m^2)}{kTR_s\Delta f}} \qquad (2.25)$$

$$= \sqrt{\frac{2m^2}{(m^2 + 4)(m^2 + 1)}}SNR_{input\_AM}$$

As illustrated in Eqn. (2.25), the noise figure is a function of modulation index m. In Figure 2.10, the modulation index m is swept from 0 to 1, and the noise figures are calculated and plotted. The noise figure reaches the minimum when the modulation index, m is 1, and the minimum noise figure is 6dB. This is the same as that of Eqn. (2.14). An intuitive explanation is that the detector output noise floor of AM modulated input case is higher than the unmodulated case due to the two additional noise sidebands and a lower output signal strength because of an increased number of unwanted sidebands. Once again, the noise impact is simulated in Matlab to verify the results. The signal in Eqn. (2.26) is applied to the input. $V_s = 1$V and $\sigma = 2.03\text{x}10^{-6}$.

$$V(t) = V_0(1 + m\cos(\omega_m t))\sin(\omega_s t) + \sigma \times randn,$$

$$\sigma \times randn \text{ has a pdf of } f(V) = \frac{1}{\sigma\sqrt{2\pi}}e^{\frac{-(V-0)^2}{2\sigma^2}}. \qquad (2.26)$$

The output PSD's are plotted for two different modulation indices and are shown in Figure 2.11. As predicted by Eqn. (2.24), the dominant part of the output noise floor is the input noise "up-converted" to f_s for a small modulation index, m. The difference between the noise floors for a modulation index of m=0.1 and of m=1 is 3.47dB from Eqn.(2.27) and as shown in the Matlab[TM] simulated results in Figure 2.11.

$$20\log\left(\frac{3V_0^2 kTR_s\Delta f\big|_{m=1}}{2.01V_0^2 kTR_s\Delta f\big|_{m=0.1}}\right) = 3.47dB \tag{2.27}$$

The dependence on AM modulation index can be intuitively explained using Eqn. (2.26). The AM modulated input signal $V_s(t)$ can be regarded as the sum of three independent input signals at ω_s, $\omega_m+\omega_s$, and $-\omega_m+\omega_s$.

$$\begin{aligned}
V_s(t) &= V_0(1+m\cos(\omega_m t))\sin(\omega_s t) \\
&= V_0\sin(\omega_s t) + \frac{1}{2}mV_0\sin(\omega_m+\omega_s)t + \frac{1}{2}mV_0\sin(-\omega_m+\omega_s)t.
\end{aligned} \tag{2.28}$$

Each signal tone induces its own "up-converted" noise sidebands around these frequencies, and the net effect is to increase the average power of the total input signal which in return makes the output noise higher. Although Figure 2.11 shows the output noise floor is insensitivity to the modulation index, m. The modulation index plays a major role in determining output signal strength. A weak modulation deteriorates the output SNR and raises the detector noise figure. In summary, when input signal is AM modulated with modulation index m, a minimum SNR degradation of 7.78dB is expected. The minimum SNR degradation is achieved when m=1, indicating the OOK like modulation scheme should be used for best detector noise performance. Except for the benefits of minimizing the negative impact of flicker noise, AM modulation generally degrades the detector noise performance. To square law detector, large input signal does not benefit the detector performance. For moderately high input signal amplitude (10mV to 150mV), input noise "up-converted" terms dominate the total output noise, increasing the detector NEP. For high input signal amplitude (>150mV), the optimum bias point of device is disturbed and detector NEP is further increased. These two effects restrict the usage of detector in small signal region if SNR is a concern.
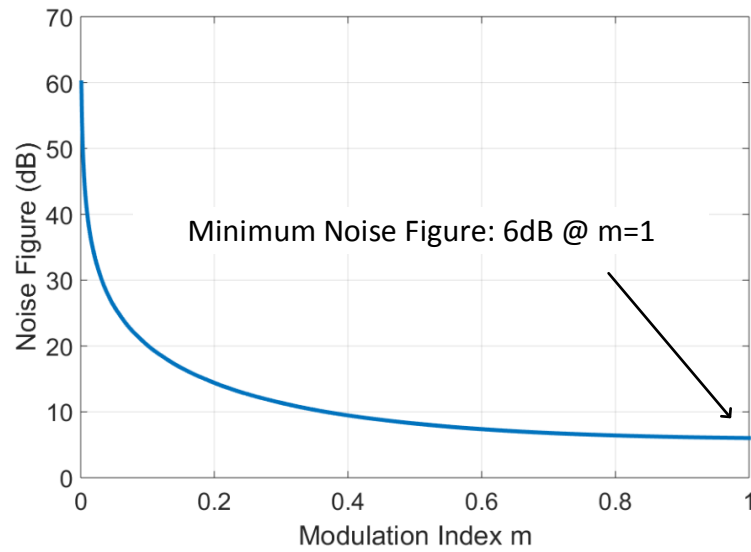
Figure 2.10   Noise Figure versus modulation index, m.
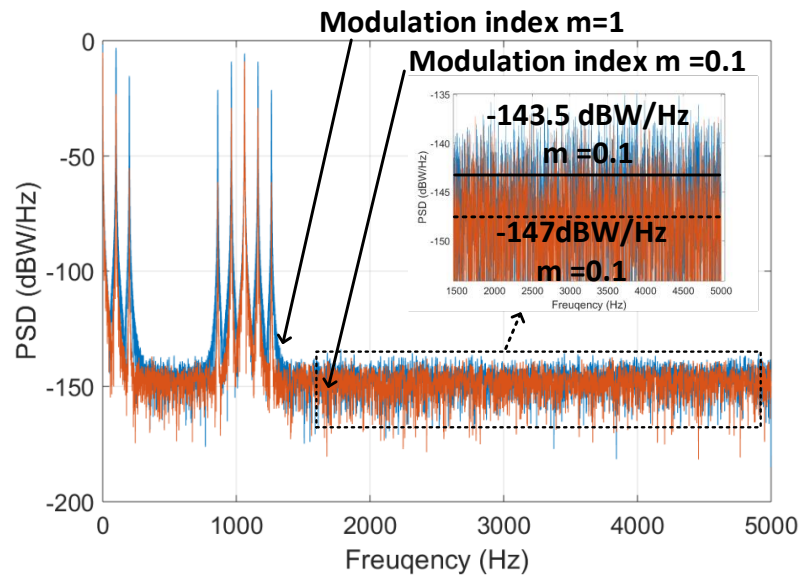
Figure 2.11   Output noise floor with a modulation index of m=0.1 and of m=1. The inset shows magnified noise floors and their mean values.

2.2.3 System Noise Limit

Having identified all the critical noise processes and mechanisms, the noise of a spectrometer can be summarized as shown in Figure 2.12. According to [18], [19], the gas absorption follows the Lambert-Beer law. Defining the available power from a radiating source of P_0, the loss coefficient of the waveguide as α_c (in cm^{-1}), and the loss coefficient associated with the gas molecule as α_g (in cm^{-1}). The power received P_1 is

$$P_1 = P_0 e^{-(\alpha_c + \alpha_g)l}. \tag{2.29}$$

The information about the molecular absorption is encoded into a change of the power when wave traveling through a gas absorption cell.

$$\Delta P = P_0 e^{-\alpha_0 l}(1 - e^{-\alpha_g l}) \approx \alpha_g l P_0 e^{-\alpha_0 l}. \tag{2.30}$$

The approximation in Eqn. (2.30) holds true when the gas absorption is small. Now with the minimum detectable signal set by Townes noise Eqn. (2.17) The detection limit of rotational spectroscopy system is (assume the noise temperature of the receiver is T_d, system bandwidth is B)

$$\frac{S}{N} = \frac{\alpha_g l e^{-\alpha_0 l}\sqrt{P_0}}{2\sqrt{k(T + T_d)B}}. \tag{2.31}$$

This result gives interesting insights about a receiver of a spectrometer. First, the signal to noise ratio increases with a square root of transmitted power, and the gas molecule saturation places the upper limit for the signal to noise ratio. Increasing the tube length l increases the travel length of waves interacting with gas molecules, which increases power absorption and the signal strength.
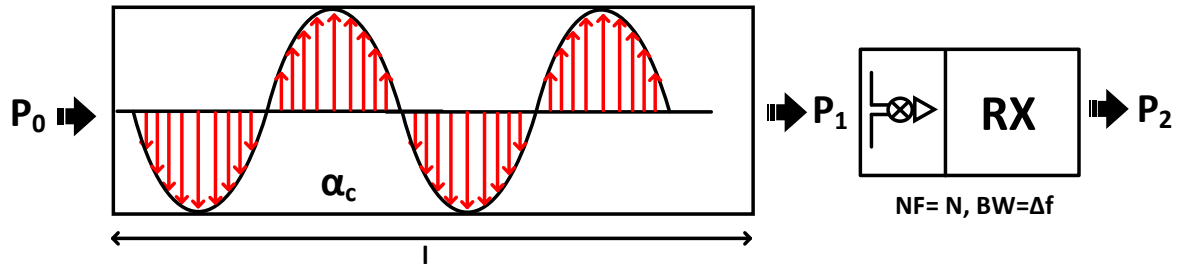
Figure 2.12   Simplified spectrometer system for noise analysis.

However, as the wave travels through the gas cell, it is also attenuated by the loss of the cell itself. Depending on the loss coefficient of the gas tube and absorption coefficient of gas molecule tube, there should be an optimum length for a given gas cell.

2.3 Receiver System Design

With the noise analysis in Section 2.2, it is obviously advantageous to choose coherent detection methods to mitigate the deleterious effects of transmitter phase noise and to increase the signal to noise ratio. The receiver system diagram is shown in Figure 2.13. This architecture is based on a conventional heterodyne system and consists of three main sections: receiver front-end (RX front-end), local oscillator chain (LO chain), and base-band circuit (baseband). The RX front end utilizes a mixer first design with an on-chip antenna picking up the signal and the mixer following the antenna performing down conversion to an intermediate frequency (IF). Following the mixer, a low noise amplifier is added as a gain stage preceding the baseband circuit. To alleviate the design challenge for the wideband high frequency of LO, the front-end mixer is designed using a sub-harmonic mixer. In the LO chain design, an X4 multiplier upconverts the

31
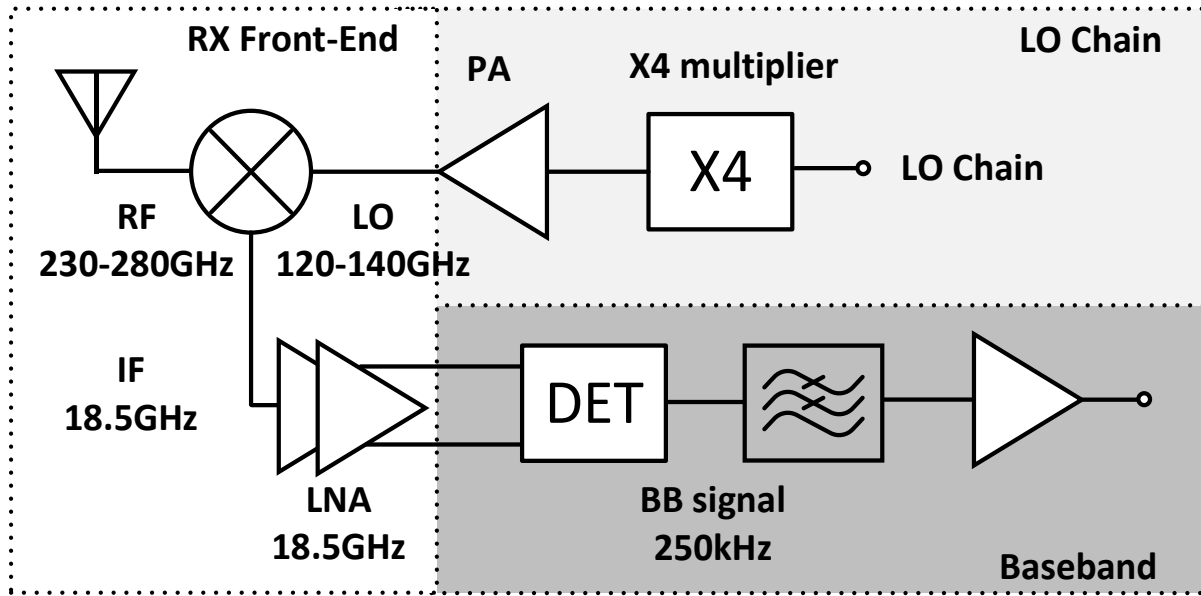
Figure 2.13   Receiver system diagram

input signal to the desired LO frequency. In the baseband section, an RMS detector is used as a demodulator which senses the power absorption by molecules.

To increase the types of gas molecules that can be detected, a receiver should have as a wide bandwidth as possible. The targeted RF range is between 200 and 280 GHz which corresponds to a 33-% bandwidth. The frequency and bandwidth requirements are challenging for both RX front-end and LO chain implementation. Although the use of sub-harmonic mixer cuts the required LO frequency into a half, however, the 33-% fractional bandwidth remains the same. To further alleviate the LO design challenges, a dual sideband down-conversion frequency plan is proposed and is shown in Figure 2.14. When RF is below 240GHz, sub-harmonic lower sideband down conversion is employed. The image frequency, in this case, will be over 400GHz which is rejected by the frequency response of IF low noise amplifier. When RF is above 240 GHz, high-side sub-harmonic down conversion is used. The dual sideband down conversion lowers the

Sub Harmonic Lower Sideband Conversion

2LO
228.5~258.5GHz

IF
18.5GHz
LO
114.25~129.25GHz
RF
210~240GHz

Sub Harmonic Higher Sideband Conversion

2LO
221.5~286.5GHz

IF
18.5GHz
LO
110.75~143.25GHz
RF
240~305GHz
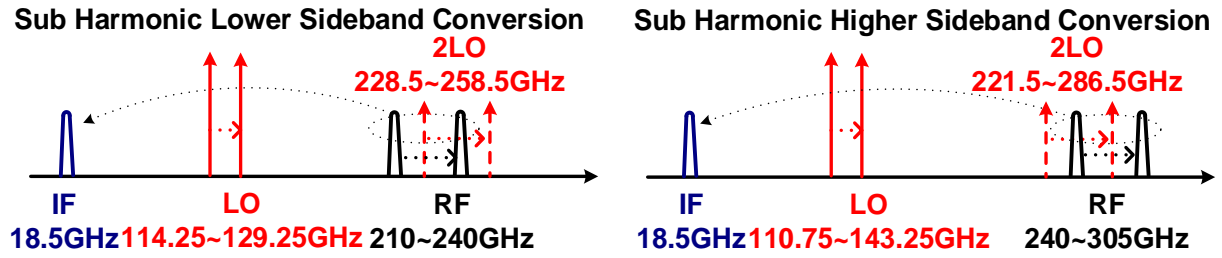
Figure 2.14   Frequency plan of the receiver.

Table 2-1   Requirements for Rotational Spectroscopy Receiver.

Specification	Value	Comments
RF frequency	200-300 GHz	Fractional BW :40%
LO frequency	110-140 GHz	Fractional BW: 24%
LO power	0-dBm	N/A
Noise Figure (NF)	15 dB	N/A
Side-band injection	Both	N/A
IF frequency	20 GHz	Fractional BW:<10%
Architecture	Mixer First High IF Heterodyne	N/A
Input	On-Chip Antenna	with an off-chip reflector

required LO bandwidth by 50%, which combined with the sub-harmonic mixing lowers the LO

absolute bandwidth by 4X. Another important feature of this frequency plan is that on the contrary

to typical wideband RX designs, a narrow band IF can be used for this application. This proves to

be beneficial especially when the first stage of the RX system has a loss because the IF amplifier

can be designed to be noise and gain matched to the down-conversion mixer to optimize gain and

noise performance. The receiver design specification is summarized in Table 2-1.

2.4 Circuit Component Design

2.4.1   Wideband Antenna Design

Silicon on-chip antennas suffer from low gain and efficiency because the high dielectric constant of the substrate (ε_r =11.9) makes electromagnetic waves propagate into the silicon substrate rather than radiated out to air [20] [21] while the loss of substrate attenuates the waves. A solution to mitigate this is to place a metal reflector at the backside of the chip to reflect the wave back to air as shown in Figure 2.15(a). By controlling the silicon die thickness to be odd multiples of $\lambda/4$, the back-reflected wave can be combined in phase with the broadside radiation, improving the peak antenna gain[22] [23]. When the substrate thickness is odd multiples of $\lambda/4$, the total phase shift of reflected wave is integer multiples of 2π.

$$\phi_{reflected\_wave} = 2\beta d + \phi_{reflector} = \frac{4\pi}{\lambda_0}d + \pi. \tag{2.32}$$

Here, β is the phase velocity and d is the silicon die thickness, $\phi_{reflector}$ is the phase shift caused by the metal reflector which is equal to π. From Eqn. (2.32), it is easily seen that when the single route travel distance of reflected wave d is $((2n+1)\ \lambda_0)/4$, where n is an integer, then the total phase shift is

$$\phi_{reflected\_wave} = 2(n+1)\pi, \tag{2.33}$$
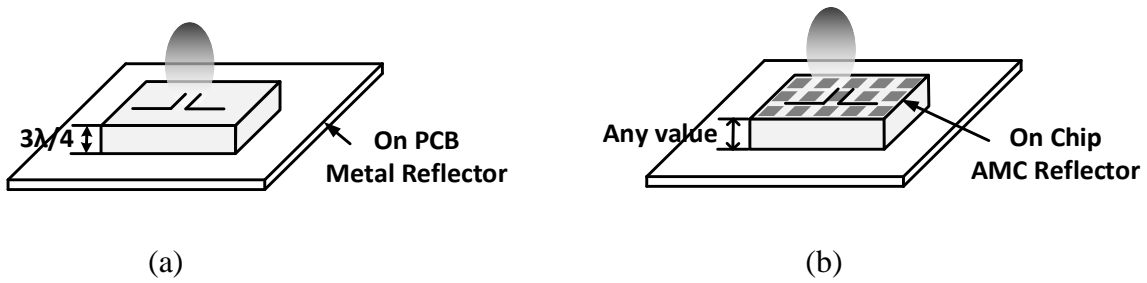
Figure 2.15   On-chip antenna (a) with an off-chip metal reflector (b) with an OC-AMC reflector.

and the reflected wave is in phase with the wave radiated from the antenna out to air if n is odd. Under this condition, the waves will add constructively, however, the requirement on the silicon die thickness restricts the applicable frequency. If the operating frequency of the on-chip antenna is too low or too high, the die thickness of 275µm to ~1mm will either be too thick or too thin. To overcome this limitation, instead of a metal reflector, use of an on-chip artificial magnetic conductor (OC-AMC) as a reflector [24] [25] has been proposed. This configuration is shown in Figure 2.15(b). The major difference is that the reflector is integrated on a chip (in many cases, they are realized using lower level metal layers). This makes the reflector be extremely close to an on-chip antenna. The total phase shift of reflected wave is close to zero because the AMC introduces a phase shift of zero at its resonance frequency and the phase shift associated with the short distance between the top and lower level metal layers is negligible.

The two methods have been proven to be effective in many applications. But for wideband applications, a major drawback of these techniques is that this constructive interference occurs over only a narrow frequency range and results in a "band-pass" response for the
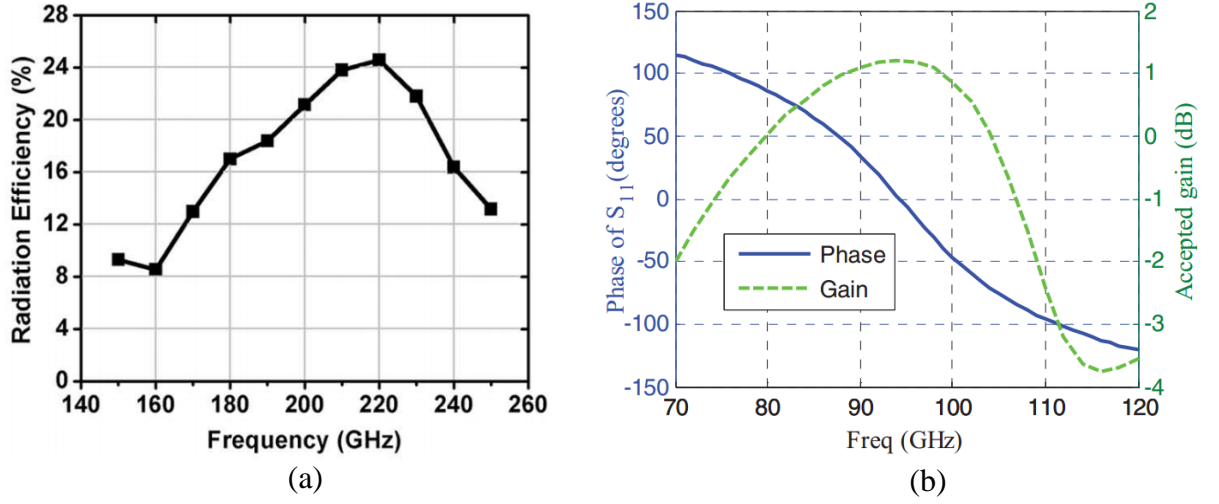
Figure 2.16   (a) Antenna radiation efficiency (with a metal reflector) [23] , (b) AMC phase response [24].

antenna gain. Eqn. (2.32) can be rearranged with operating frequency f as the independent variable. With the metal reflector tuned for center frequency f_0.

$$\phi_{reflected\_wave} = 2\beta d + \phi_{reflector} = (2n+1)\pi \frac{f}{f_0} + \pi \tag{2.34}$$

Constructive interference with a reflected wave is only achieved when $f=f_0$. In an extreme case at $f=2f_0$, the reflective wave will even cancel the broadside radiation. The radiation efficiency versus frequency characteristics of a metal reflector backed on-chip antenna is shown in Figure 2.16(a). The added off-chip metal reflector significantly shrinks the antenna radiation bandwidth.

For the OC-AMC, although it eliminates the frequency dependent phase shift caused by the silicon substrate, the AMC itself introduces frequency dependent phase shifts shown in Figure 2.16(b). Unlike the metal reflector which always presents a 180° phase shift to incoming waves, the AMC has a resonant behavior with a limited bandwidth.

To mitigate these bandwidth limitations, a phase-compensated AMC (PC-AMC) reflector is proposed in this design. The basic configuration is shown in Figure 2.17. This approach uses an off-chip metal reflector but with an AMC structure instead of a metal reflector. In order for constructive interference at the surface of the IC, the die thickness needs to be even multiples of λ/4. Figure 2.17 illustrates the phase shift versus frequency.
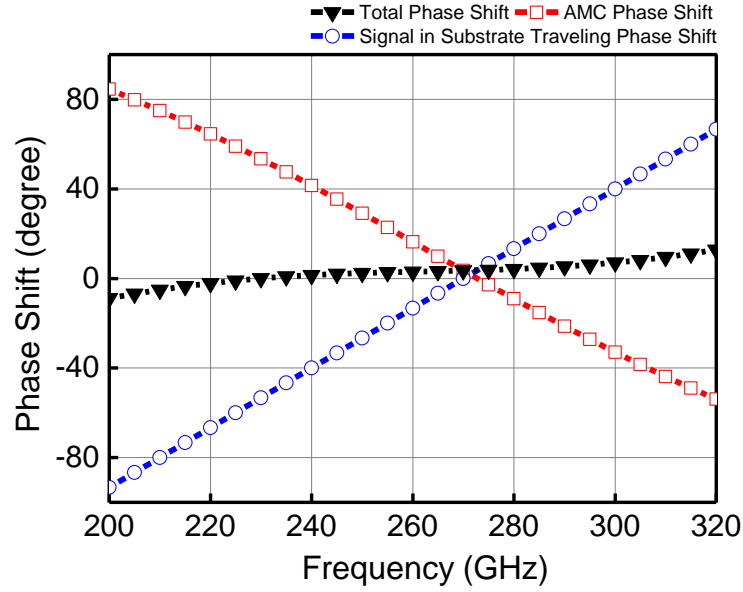
Figure 2.17   PC-AMC reflector configuration and phase compensation mechanism

The frequency dependent phase shift of an AMC reflector on the backside of chips is compensated using the phase shift through the silicon substrate. The frequency response of the phase shift due to the AMC and propagation through the substrate have an opposite frequency dependence.

$$\phi_{reflected\_wave} = 2\beta d + \phi_{reflector} = 2n\pi \frac{f}{f_0} + 2\pi k_{AMC}(1 - \frac{f}{f_0}) \qquad (2.35)$$

37

The Eqn. (2.35) describes the basic phase relationship. Here a linear approximation is applied to the AMC surface phase shift with a slope of k_{AMC}. If the operating frequency f moves away from the tuned frequency f_0, the linear phase change due to wave propagation is countered by the AMC phase change.

This compensation is most effective when k_{AMC}=1. When compensated, the phase shift can be kept less than +/-8 ˚ over the entire operating frequency range and makes the antenna efficiency to be within 0.5dB of the peak efficiency between 200 to 300 GHz as shown in Figure 2.18.
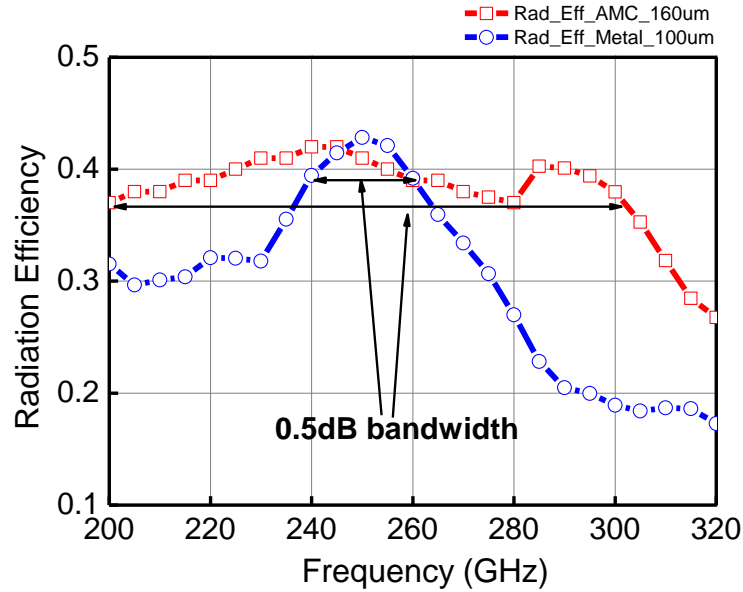
Figure 2.18   Radiation efficiency: PC-AMC (circle) and Metal (square) reflector.
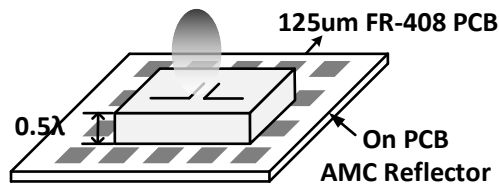
Figure 2.19   PC-AMC reflector configuration.

A PC-AMC reflector is shown in Figure 2.19. The AMC cells are fabricated on a PCB. The die thickness is trimmed to $\lambda/2$ and it is placed on a PCB containing the AMC reflector.

2.4.2 Harmonic Mixing Using an Anti-Parallel Diode Pair

For sub-harmonic mixing, an anti-parallel diode pair (APDP) is commonly used because of its ability to reject even order mixed products [26],[27],[28]. Although CMOS-compatible Schottky barrier diodes [29] are available, an antiparallel diode-connected NMOS transistor pair biased in the sub-threshold region has better performance due to its symmetry. However, as illustrated in Figure 2.20, diode-connected transistor pair with a grounded-body (GB-APDP) experience different body-to source-voltage (V_{BS}) or body effect.
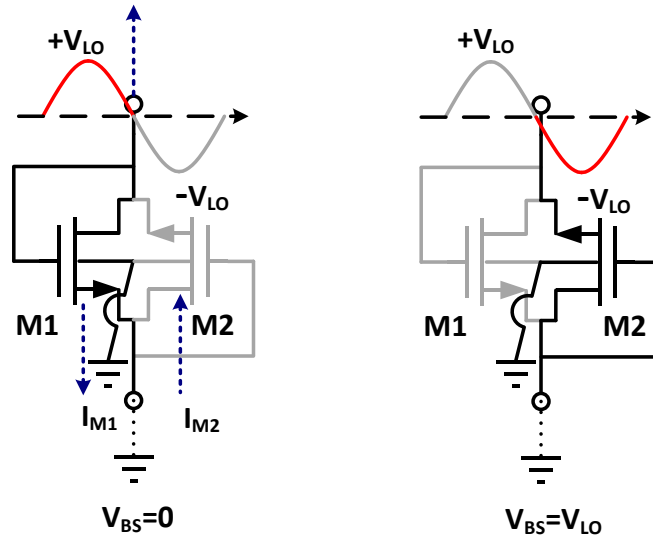
Figure 2.20   Asymmetry in an APDP using diode connected transistors with a grounded body during a cycle of LO swing.

Because of this, even-order harmonics are not perfectly canceled, and an increased conversion loss is observed in simulations. The simulated two branch current during a large LO voltage swing of

GB-APDP is shown in Figure 2.21. These two currents should be identical if the devices are perfectly balanced. But body effect mismatch makes the two currents be not the same and thus, the 2nd harmonic currents of GB-APDP are not perfectly canceled.
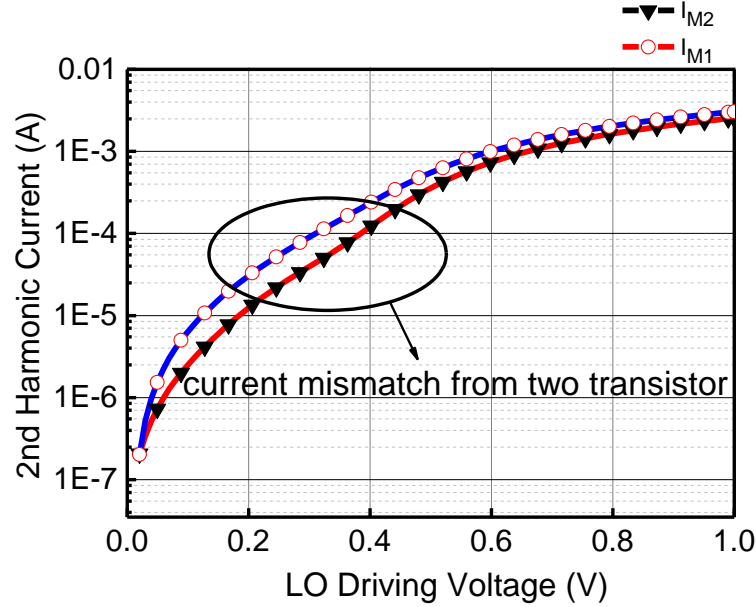
Figure 2.21   Two branch currents in a GB-APDP versus LO driving voltage.

More importantly, because the LO power is used to generate its second-order harmonic, the LO power required for the minimum conversion loss is high. To precisely determine the ability of the device to generate the desired non-linearity and reject unwanted harmonic terms, a test-bench in Figure 2.22 is constructed. An ideal single-tone large signal voltage source is used to drive the device under test, which in this case, is an APDP. The large signal source only generates a signal at the fundamental frequency, and the rest comes exclusively from the device under test (DUT). The voltage source presents an ideal short to ground, All the generated harmonic currents can be extracted equally from the device without impedance matching. In general, this is equivalent to a

large signal harmonic Y_{21} measurement. This setup is simulated using a foundry RF transistor model with gate and drain tied together.
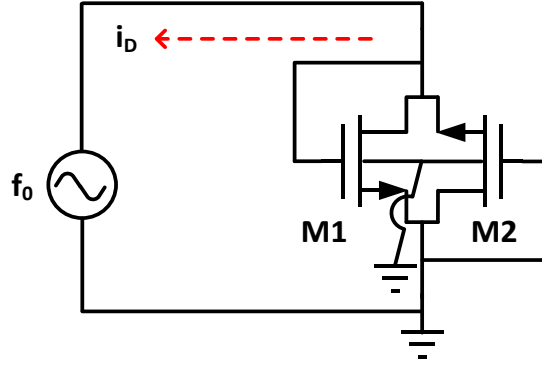
Figure 2.22   Harmonic current gain test setup

The current coming out of the device in this setup can be written using a power series in Eqn. (2.36). The I_0, I_1 ... are the power series coefficients.

$$i_D = I_0 + I_1 \cos(2\pi f_0 t) + I_2 \cos(4\pi f_0 t) + I_3 \cos(6\pi f_0 t) + ... \qquad (2.36)$$

From this, the harmonic current gain can be defined as,

$$G_k = \frac{I_k}{I_1}, \text{ where k is integer.} \qquad (2.37)$$

The harmonic current gain of GB-APDP device are shown in Figure 2.23, and plotted with respect to the LO voltage amplitude. The second harmonic current gain is a good indicator of the device symmetry as in a symmetric APDP pair, the 2nd order harmonic current is internally circulating and the extricate current is zero. However, in the GB-APDP case, the second harmonic current is 3% of the fundamental current which results wasting of a significant amount LO power and unwanted 2nd order harmonic generation.

41
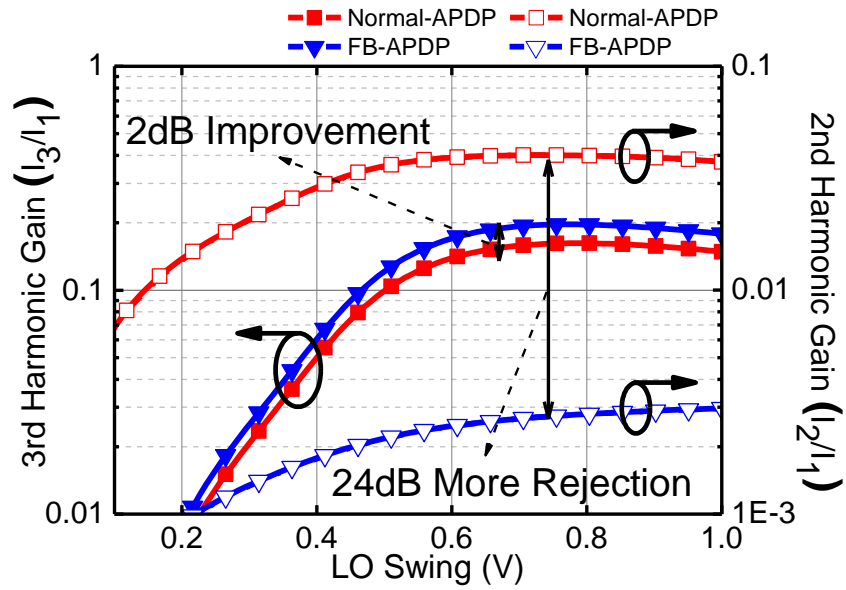
Figure 2.23   Second and third order harmonic current gains of GB-APDP device (Normal-APDP) and Floating body APDP device (FB-APDP).
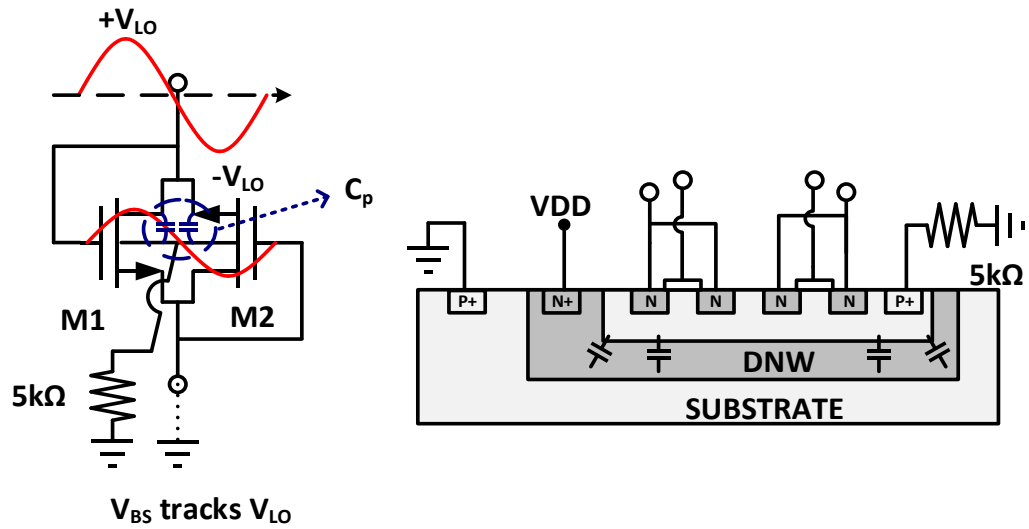
Figure 2.24   Floating body APDP circuit (left) and its realization in a CMOS process (right).

To avoid these, a floating-body NMOS APDP (FB-APDP) is used. As shown in Figure 2.24, two NMOS transistors in an isolated p-well are used to form an APDP structure. Instead of connecting the body terminal directly to the ground, a 5-kΩ resistor is inserted between the ground and body node to AC isolate or float the body node. This makes the body voltage to track the LO drive through the parasitic coupling and to keep the source-to-body voltages of both MOSFETs the same over an entire LO cycle. As shown in Figure 2.25, an applied large signal LO swing creates a replica of itself at the body, and the body voltage closely tracks the changes of drain/source terminal.
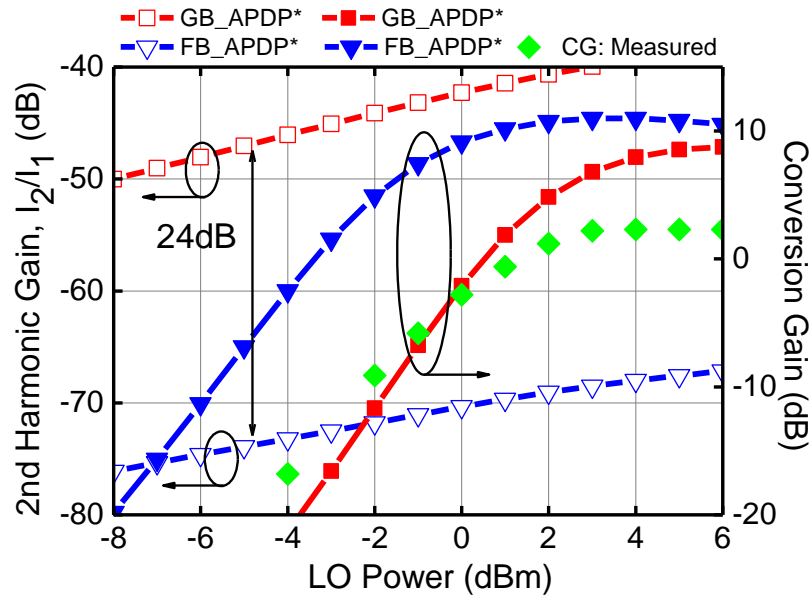
Figure 2.25   Conversion gain comparison between FB-APDP and GB-APDP

The effectiveness of floating body connection can be clearly seen from the simulations results shown in Figure 2.23 and Figure 2.25, which show that the undesired second harmonic currents which can decrease the sub-harmonic conversion efficiency and increase the noise

"folding" effect by creating a strong fundamental mixing term rejected by more than 24dB. This proves that an FB-APDP is more symmetrical than a GB-APDP. Using an FB-APDP can increase the conversion gain by 2dB compared to using a GB-APDP device. The required LO power to reach the mixer saturation is also reduced by 4dB.

2.4.3   Hybrid design

The floating body APDP is incorporated into a broad-band hybrid structure for signal isolation and impedance matching. Conventional hybrid designs rely on $\lambda/4$-transmission lines for both impedance matching and isolation between RF and LO. A typical example is a rat-race coupler [30]. However, the strong frequency dependence of quarter wave line makes it narrowband. The designs usually occupy a lot of spaces. There are certain types of hybrid that are capable to operate over a large bandwidth, such a hybrid is a "magic-T" [31] as shown in Figure 2.26.
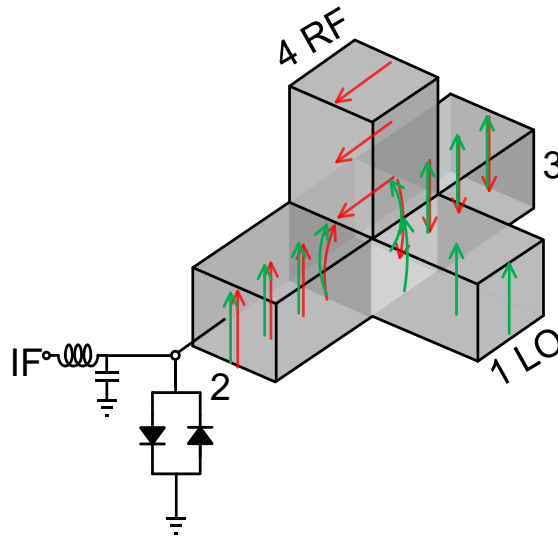
Figure 2.26   Magic-T hybrid and its application in a mixer.

"Port 1 is called "sum" port, and is also sometimes called the H-plane port. A signal incident on port 1 equally splits between ports 2 and 3, and the resulting signals are in phase. Ports 2 and 3 are sometimes called the co-linear ports, because they are the only two that are in line with each other. Port 4 is the Δ (difference or delta) port, and is also sometimes called the E-plane port. A signal incident on the difference port splits equally between ports 2 and 3, but the resulting signals are 180° out of phase."[32] Port 1 is isolated from port 4 because two different modes are excited in these two ports and they are not compatible with each other. This isolation is effective so long as the wave-guide is operating in its dominant mode. The bandwidth of magic -T hybrid is thus the same as waveguide bandwidth which easily exceeds hundreds of GHz. The wideband of magic-T inspired the idea to use "mode isolation" to implement a hybrid.

Three different types of transmission lines, differential transmission line (Diff Line), three-line transmission line (Tri-TL) and grounded coplanar waveguide (G-CPW), are shown in Figure 2.27.

Diff Line (Odd Mode)   **Tri-TL (Even/Odd Mode)**   **G-CPW (Even Mode)**
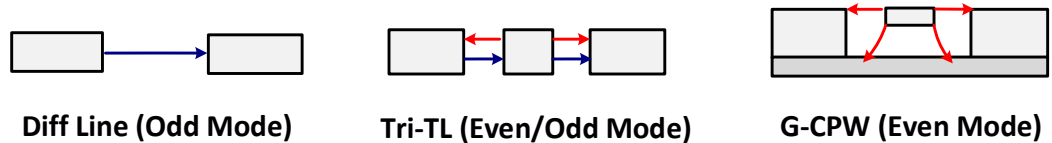
Figure 2.27   Three different types of transmission lines and their supported modes.

For a Diff Line, only a differential mode or so-called an odd mode is permitted when differentially excited. For a G-CPW, the signal line is enclosed by metal ground around three surfaces permitting quasi-TEM mode transmission. The cross-section of G-CPW shows even distribution of electrical field from the signal conductor to the surrounding ground conductor, thus this mode is an even mode. G-CPWs and Diff Lines are widely used in microwave integrated

circuit design. An interesting variant of these two transmission lines is the three-line transmission line which is basically a CPW with floating ground. Depending on the excitation methods, a Tri-TL can simultaneously support even and odd modes.

The hybrid design is based on these three transmission lines as shown in Figure 2.28. The first section is a Diff Line which transmits an odd mode signal, the second section is a Tri-TL in which both even and odd mode signals are supported and the third section is G-CPW where only even mode signal is permitted. The modes are not compatible with each other in the first and third section, providing wideband isolation between these two ports. On the other hand, in the middle section, both modes are supported and both signals from the 1st and 3rd sections can flow in the middle region. This structure resembles the magic-T structure. The difference is that the structure is planar. In Figure 2.28, port 1 and port 4 are isolated while port 1 and port 4 can both propagate to port 3.
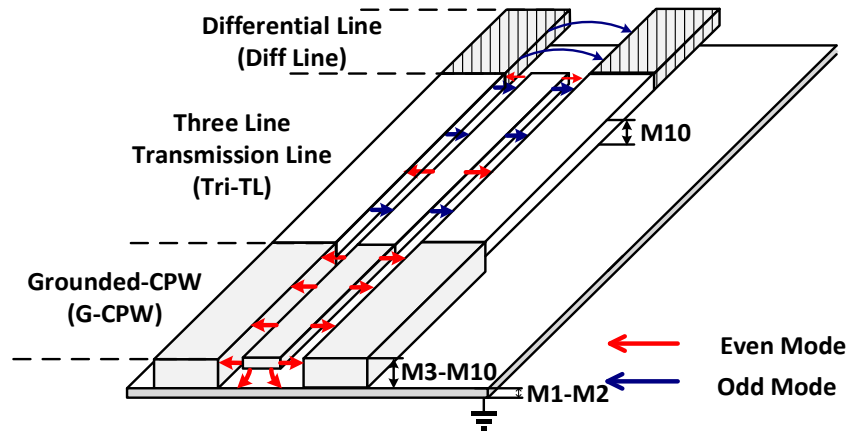
Figure 2.28   Conceptual diagram of hybrid design using mode isolation

With this hybrid, the mixer design is straightforward. As shown in Figure 2.29, the Diff Line section should be connected to an on-chip dipole antenna which naturally provides a
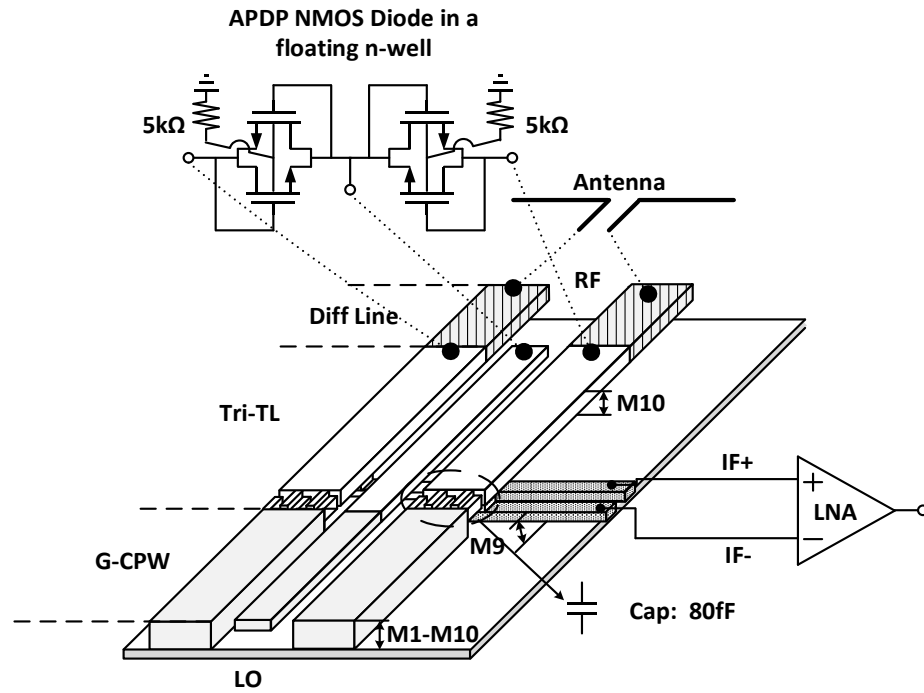
Figure 2.29   Complete mixer design with the hybrid.
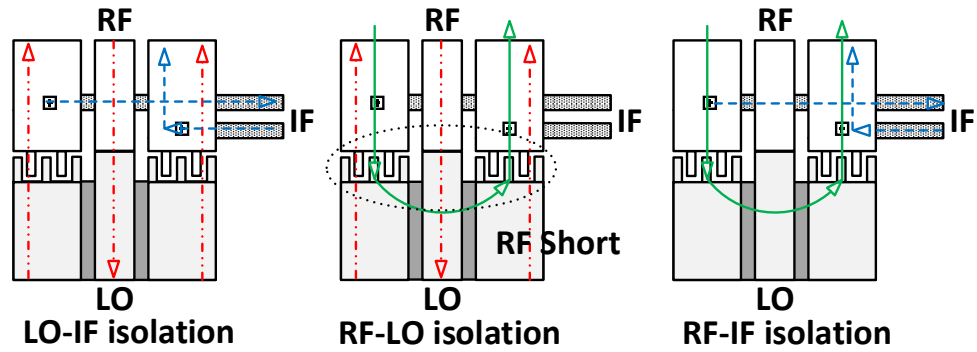
Figure 2.30   Port to port isolation diagram.

differential signal. LO is fed in using a G-CPW. With this configuration, wideband isolation between RF and LO signals can be achieved because their feed structures cannot support the mode of the other. Lastly, to isolate the IF path from the hard short provided by the ground of G-CPW,

two 80-fF metal-oxide-metal capacitors are inserted into the ground path of LO G-CPW. This capacitance is essentially a short at RF and LO frequencies and absorbed into the IF matching network. Another benefit of this configuration is that the IF signal is extracted from the node at which LO and RF signals are AC grounded. This allows implementation of a high-Q IF matching network without affecting the LO and RF matching. In simulations, the hybrid provides over a 100-GHz bandwidth with less than 1-dB transmission loss. RF-to-LO, LO-to-IF and RF-to-IF isolation all exceed 50dB. The port to port isolation diagram is shown in Figure 2.30.

2.4.4   LO Chain Design

The LO chain consists of a frequency quadrupler and a two-stage LO driver. The quadrupler takes input signals at 27.5-32.5 GHz (30.4-34.8 GHz in measurements) and generates output signals at 110-130 GHz (121.6-139.2 GHz in measurements). The LO driver utilizes two stages of capacitively neutralized differential common source stages to drive the LO port of receiver front-end that requires 0-2dBm power.
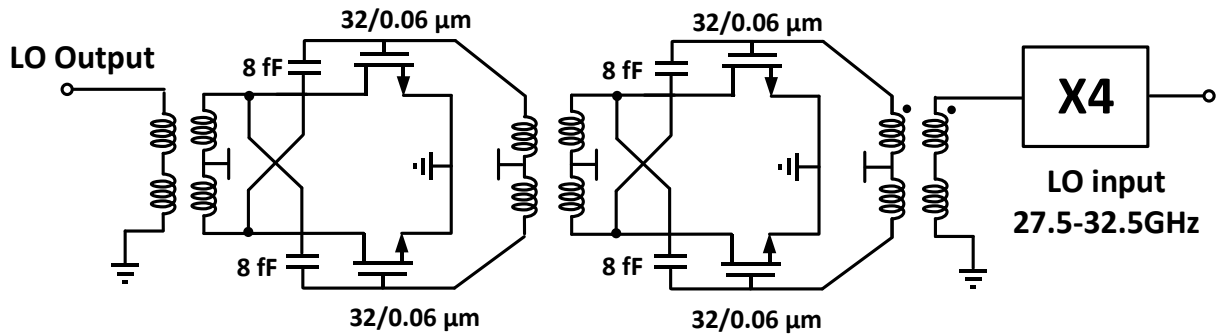
Figure 2.31   LO chain circuit diagram.

48

2.4.5   IF LNA and Baseband Circuit Design

An IF low noise amplifier is designed to operate around 20 GHz and consists of two stages. Its input and output are transformer coupled with a high turn ratio of 4:2 and 3:2, respectively. This allows exact noise and gain match. Slight degenerations are added to each stage using 50-pH
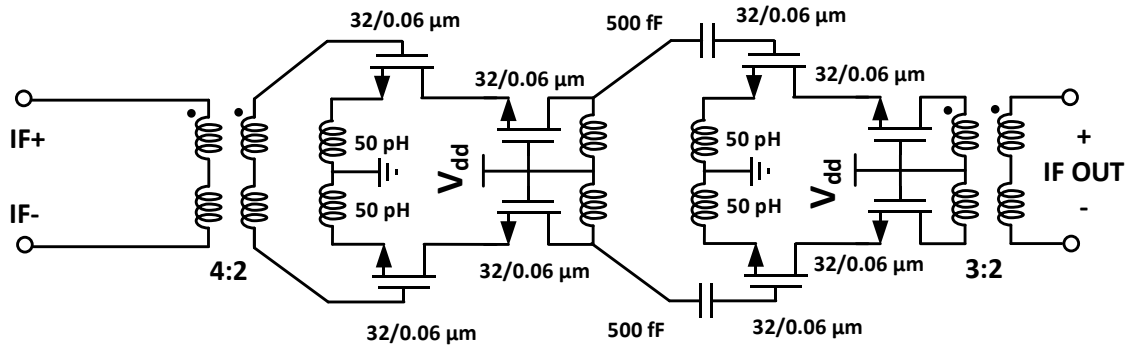
Figure 2.32   IF LNA circuit diagram.
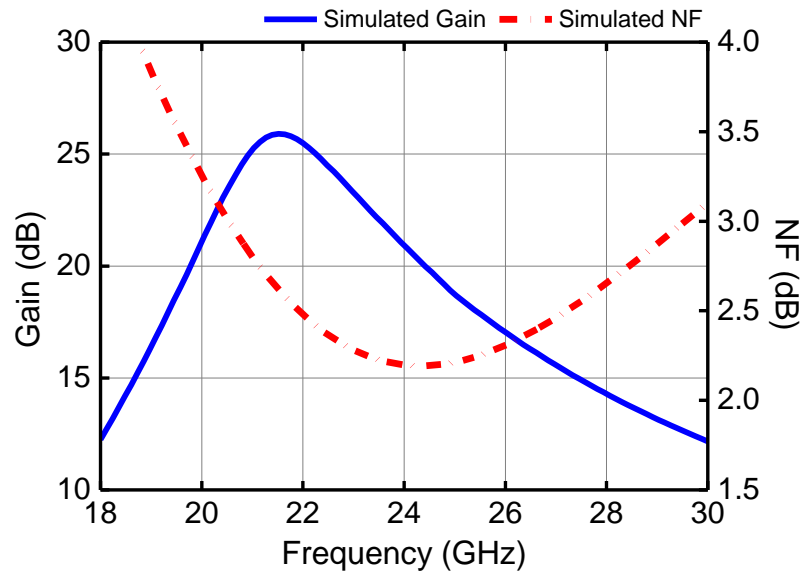
Figure 2.33   Simulate power gain (dash line) and noise figure (solid line) of IF-LNA.

differential inductors to make impedance matching. The gain stages are composed of a cascode structure for its excellent power gain and reverse isolation. The simulated power gain and noise figure are shown in Figure 2.33. At 20 GHz, the IF-LNA has about 20-dB power gain with 3-dB noise figure.

A doubler based amplitude detector [33] is used as a demodulator. The overall circuit diagram is shown in Figure 2-26. The output of IF amplifier in the RF front-end is coupled to the detector using a transformer. The transformer provides higher-Q impedance matching from the RF front-end which not only increases the responsivity of detector but also rejects the out of band noise and mixing spurs from the RF front-end. The 20-GHz power detector consists of two pairs of sub-threshold biased frequency doublers ($M_{1\sim4}$) with a resistive load. One pair is excited by the differential IF signal and produces a demodulated signal (DO+) while the second pair acts as a reference (DO-). By subtracting these two outputs, an output voltage proportional to a square of the input IF voltage is generated. The load resistors and output bypass capacitors C_1 and C_2 are
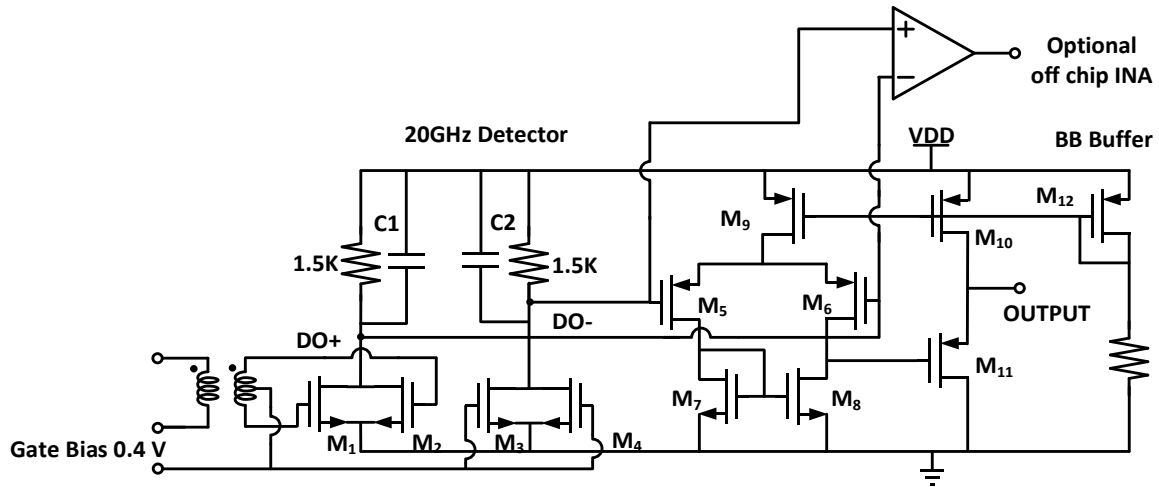
Figure 2.34   Baseband detector and buffer circuit diagram.

chosen to be 1.5kΩ and 1pF, respectively to make the low pass bandwidth (100MHz) greater than

the modulation frequency range of the RF input signal (100kHz~10MHz).

Table 2-2　　Size of transistors in the baseband detector and buffer.

Name	Size (W/L in μm)	Name	Size (W/L in μm)
$M_{1\sim4}$	160/0.16	$M_{7\sim8}$, M_{10}	50/1
$M_{5\sim6}$	30/1	$M_{11\sim12}$, M_9	150/1

Simulated responsivity (R_v) of 8kV/W and noise equivalent power (NEP) of 2pW/√Hz for the 20-

GHz detector is shown in Figure 2.35. The width and length of the transistors are 150 and 0.16

μm. The flicker noise corner frequency of the detector is 100 kHz. The relatively high output

impedance
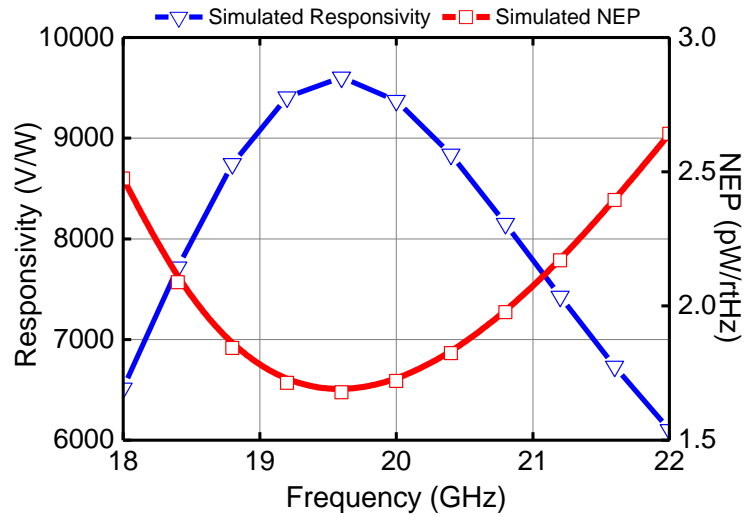
Figure 2.35　　Simulated NEP and responsivity of the detector.

(~1.5kΩ) of detector limits its driving capability at high modulation frequencies. A buffer amplifier

is added to provide a low impedance output and to improve the load driving capability. The 3-dB

51

bandwidth of the amplifier is 10 MHz with a 25-pF load capacitor. It is important that this buffer amplifier to also be low noise and low gain in order not to deteriorate the dynamic range and noise performance. In this design, the first OTA stage serves as the main gain stage and it also converts the differential signals to single-ended signals. The input transistor is sized with a W/L ratio of 300μm/1μm to reduce the flick noise corner. This stage is followed by a common drain stage that provides low impedance output. The buffer amplifier has simulated voltage gain of 20dB, input referred noise of 4nV/√Hz and flicker noise corner frequency of 100 kHz.

2.5 Receiver Measurement

2.5.1   Receiver Front-end Characterization

The measurements are performed on the wafer. Pictures of the measurement setup are shown in Figure 2.36, and a detailed diagram is shown in Figure 2.37. The TX signal is generated by a WR.03 X18 multiplier and radiated using a standard gain horn antenna. To verify the effectiveness of PC-AMC reflector, two different silicon dies with a thickness of 0.25λ and 0.5λ are prepared. The reflector is placed underneath the silicon die. The AMC is fabricated using a
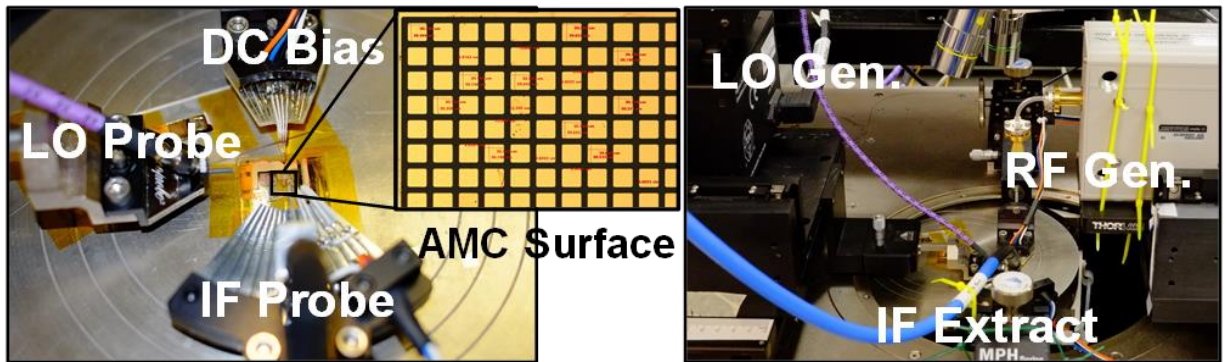
Figure 2.36   Receiver front-end measurement setup
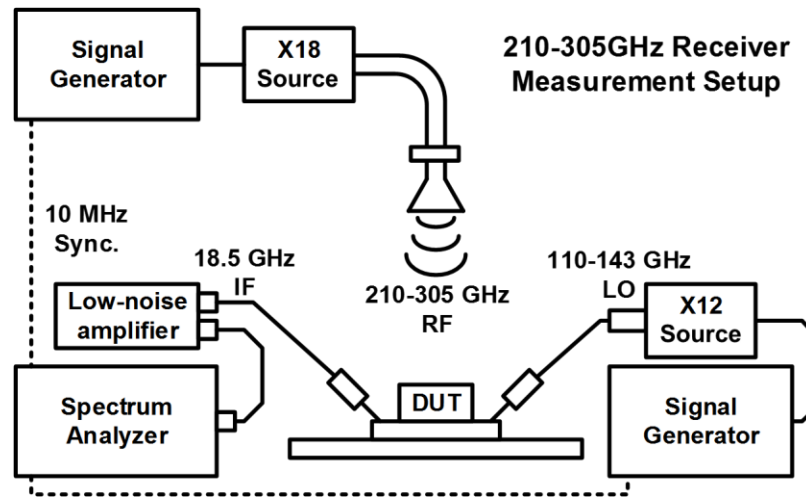
Figure 2.37   Receiver measurement diagram.
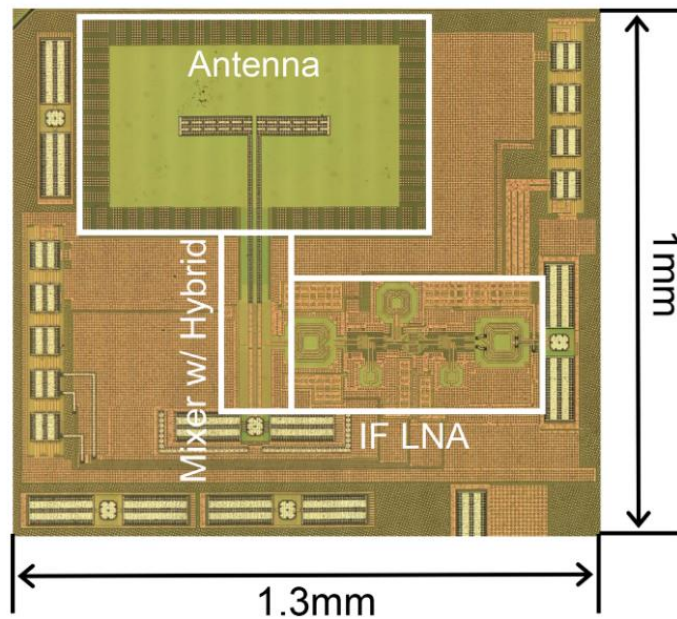
Figure 2.38   Receiver front-end chip die photo.

separate PCB in clean room. The TX antenna was positioned above chip in such a way to satisfy

the far-field radiation condition. The LO signal is generated using an X12 multiplier and IF is

extracted from the chip using a low noise amplifier connected to a spectrum analyzer. Figure 2.38 shows a die photo. The front-end test chip size is 1mm x 1.3mm.

Table 2-3 summarizes the measurement parameters. For frequency sweep, the TX antenna position was slightly adjusted at each frequency step in an effort to accommodate the shift of radiation pattern. The distance R of 11cm is calculated to be in the far-field and experimentally verified by observing the R^{-2} dependence.

Table 2-3   Measurement Variables Summary

Name	Value	Description
P_{IF}	As measured	Measured IF power in dBm
P_{TX}	-20dBm	Transmitter output power
G_{TX_ant}	20dB	TX antenna gain
R	1cm	Distance of antenna to chip
P_n	As measured	IF output noise in dBm/Hz

The RF input power is calculated using the *Friis's* transmission equation without including the extra attenuation of the atmosphere. The path loss L_{path} is calculated from the free space sphere envelop transmission in Eqn. (2.38). Conversion gain (*CG*) is defined in Eqn. (2.39). The noise figure (*NF*) is calculated from the measured noise at the IF amplifier output and conversion gain.

$$L_{path} = 20\log(\frac{\lambda}{4\pi R}) \qquad (2.38)$$

$$CG = \frac{p_{IF}}{p_{TX} - G_{TX\_ant} + L_{path}} \qquad (2.39)$$

$$NF = \frac{p_n}{p_n + 174(\text{dBm/Hz}) - CG(\text{dB})}$$ (2.40)

Figure 2.25 also shows the measured conversion gain versus LO power at 240 GHz. The measurements are performed on wafer. The measured conversion gain at LO power of 2dBm is ~5dB lower than the simulated. However, the LO power required for the conversion loss saturation is within 1dB of simulation suggesting that use of FB-APDP's reduced the LO drive requirement. Figure 2.39 shows the measured conversion gain and single-sideband noise figure of RX. Both RX with the PC-AMC reflector (RX_AMC) and the one with a metal reflector (RX_Metal) exhibit good conversion gain (2-7dB) and acceptable noise figure (13.9-19dB) at 240 to 260 GHz. The
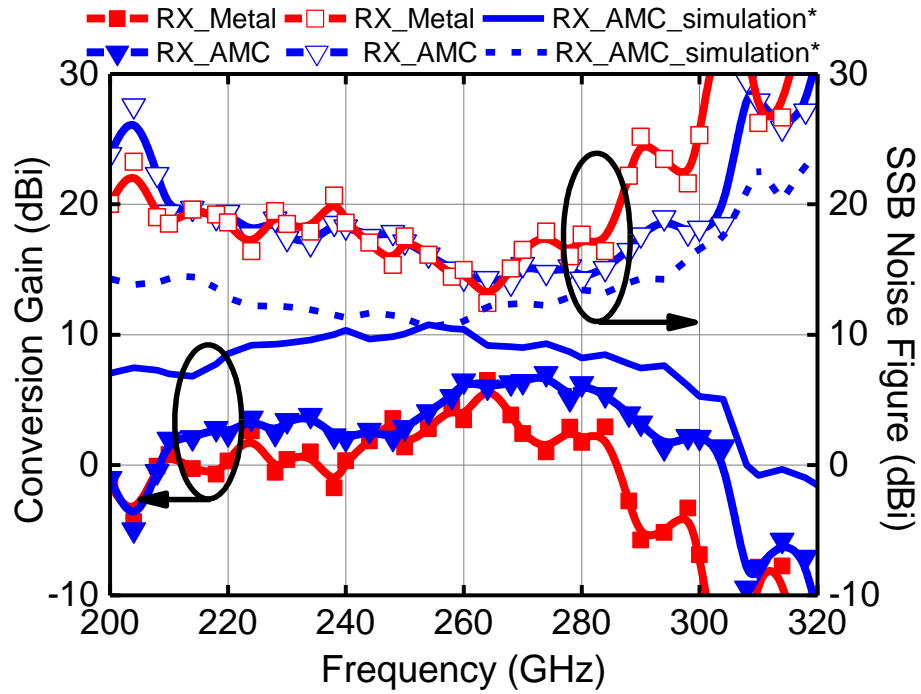
Figure 2.39   Measurement results of receiver front-end (*Simulation results consist of HFSS simulated antenna gain and ADS simulated mixer and IF LNA Gain)

available LO power is 2-4 dBm. However, above 260 GHz and below 240 GHz, the RX_AMC shows significantly improved performance. As a result, the RX_AMC achieves conversion gains between 2 and 7dB and noise figure between 13.9 and 19 dB from 210 to 305GHz. The noise figure should be sufficient for uses in a rotational spectrometer. Figure 2.39 also shows the simulated conversion gain and noise figure of RX_AMC. The measured and simulated gain and noise figure are within around 5dB over the entire frequency range. The comparison in Table 2-4 indicates that this work demonstrates the best in class noise figure in terms of minimum value, bandwidth and in-band variation.

Table 2-4   Comparison of the state-of-art receiver front ends

Ref.	[34]	[35]	[36]	**This Work**
Technology	65nm CMOS	65nm CMOS	SiGe HBT	**65nm CMOS**
RF (GHz)	240	239-281	202-230	**210-305**
Bandwidth (GHz)	7.6	42	28	**95**
LO Freq. (GHz)	80x3	242-285	110	**115-142.5**
LO Power (dBm)	-3	0	0	**2**
Mixer Topology	Fund	Fund	2nd HM	**2nd HM**
SSB Noise Figure (dB)	15	40	16	**13.9-19**
Conversion Gain (dB)	25	-2	18	**2-7**
RF Interface	OCA	OCA	Probe	**OCA**

2.5.2 Receiver Characterization

A printed circuit board (PCB) for receiver testing is shown in Figure 2.40. The PCB is made of FR-5, a high-frequency material with a thickness of 600 µm. An RX chip which is thinned to 100 µm to improve antenna efficiency is mounted on a gold-plated ground plane which acts as a metal reflector. A Texas Instrument INA155 instrumental amplifier is used as an optional off-chip buffer for the detector. The LO signal is provided using an SMK cable and interfaced to the PCB using an end-launch K connector. A 17-mm long CPW on the PCB and bonding wires are co-designed to create wideband impedance matching between the LO source connected using an SMK cable and the on-chip LO input port. Figure 2.41 shows a die photograph of the receiver. The chip area including bond pads is 2.8 mm^2.
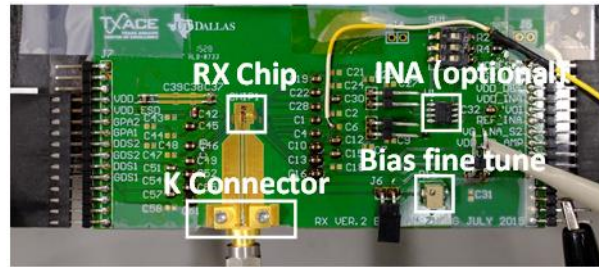
Figure 2.40   PCB of receiver.
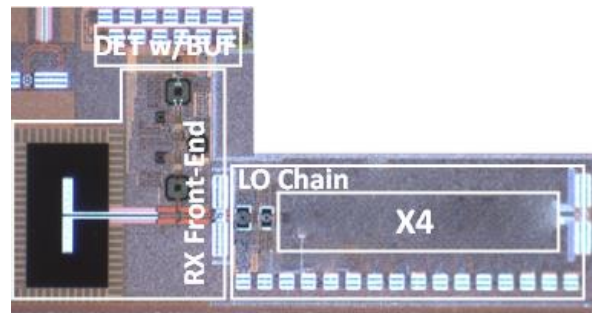
Figure 2.41   Receiver die photo.

The measurement setup for the receiver is shown in Figure 2.42. 225-280 GHz RF signals are generated using an Agilent SM-03 multiplier chain and radiated to the receiver using a WR-03 standard horn antenna with a 21-dB gain. To reduce the impact of flicker noise to the receiver operation, the RF signals are amplitude modulated at 200 kHz. The Agilent transmitter is placed 12cm away from the RX under test to ensure far-field operation. The LO signal for the RX is generated using an Agilent E8257D signal generator and an active frequency doubler from SpaceK Labs. The demodulated 200-kHz signal is measured using a vector signal analyzer (VSA).
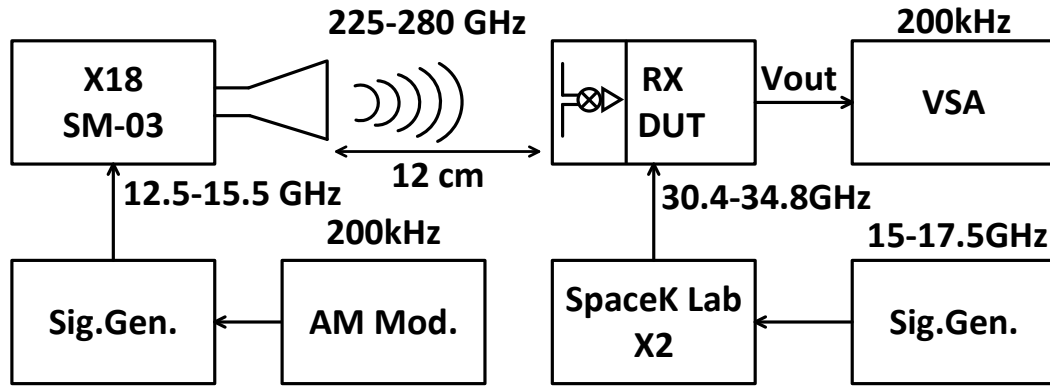
Figure 2.42   Receiver measurement setup.

The measured responsivity, R_v (volts/watt) is defined in Eqn. (2.41). "V_{out} "is the output of the receiver. The measured noise equivalent power, NEP (watt/$\sqrt{Hz}$) is defined in Eqn. (2.42). "V_{n_out} "is the output voltage noise in volt/$\sqrt{Hz}$.

$$R_v = \frac{V_{out}}{p_{TX} - G_{TX\_ant} + L_{path}} \tag{2.41}$$

$$NEP = \frac{V_{n\_out}}{R_v} \tag{2.42}$$

The R_v varies between 400 and 1200 kV/W, while the NEP varies between 0.4 and 1.2 pW/√Hz at 225 to 280 GHz as shown in Figure 2.43. During the LO chain testing it was found that its operating frequency range shifted from 110-130 GHz to 122-140 GHz as shown in Figure 2.44, and the tuned
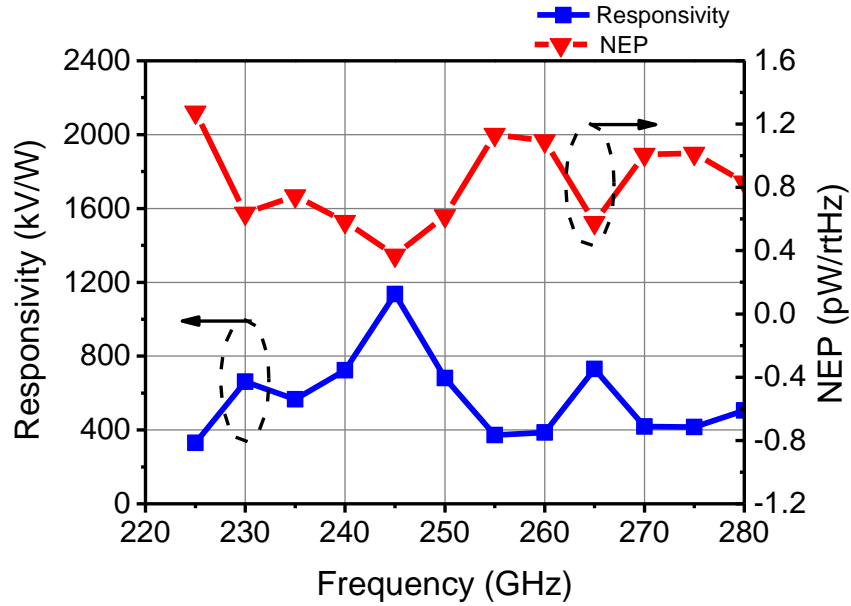
Figure 2.43   Measured responsivity and NEP of receiver.
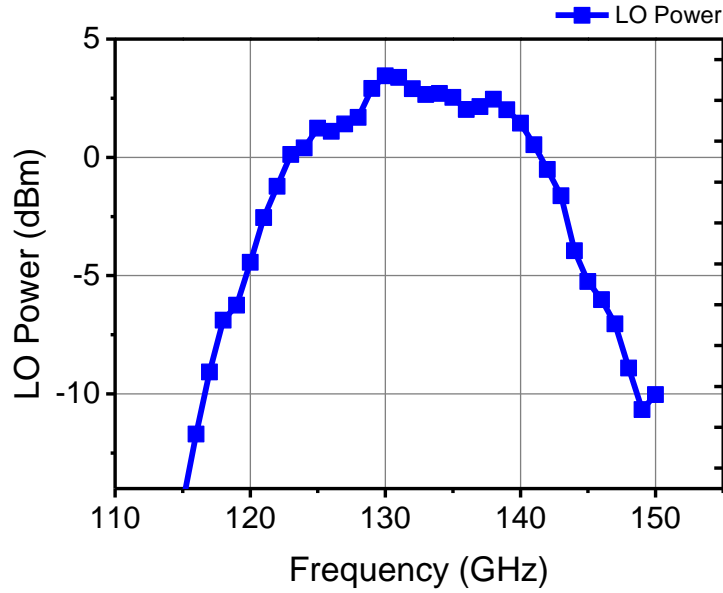
Figure 2.44   Measured LO power versus frequency.

59

frequency of IF amplifier shifted from 20 GHz to 18.5 GHz. To work around this, for the RF range between 225 and 260 GHz, low side down-conversion is employed while high side down conversion is employed for the RF range between 260 and 280GHz. Because of the LO operation frequency range shift, the operating frequency range of receiver was reduced from 210-280 GHz (Metal reflector [17]) to 225-280 GHz. The measured performance of the receiver is summarized in Table 2-5. The difference between the measurements and simulations are mainly due to the shifts of LO and intermediate frequencies.

Table 2-5   Receiver Performance Summary

Item		Measurement	Simulation
Technology		**65nm CMOS**	
System Bandwidth		225-280 GHz	200-280 GHz
IF frequency		18.5 GHz	20 GHz
Off-chip LO frequency		30.4-34.8 GHz	27.5-32.5 GHz
On-chip LO frequency		122-139 GHz	110-130 GHz
On-chip LO Power		0-3.6 dBm	0-2 dBm
Responsivity		400-1200 kV/W	2100 kV/W
NEP		0.4-1.2 pW/√Hz	0.2pW/√Hz
Power Consumption	RX Front-End	42mW	38mW
	Detector	0.78mW	0.88mW
	BB amplifier	0.96mW	0.96mW

2.6 Measurement of Gas Spectrum Using the CMOS Receiver

The rotational spectroscopy measurement setup is shown in Figure 2.45. Transmitted signals at 210-260 GHz are generated using a frequency multiplier chain from Virginia Diodes Inc. (VDI) and radiated. The radiated signals are collected and converted to a plane wave using a lens. This wave is then propagated through a 1-meter-long 10-cm diameter metal
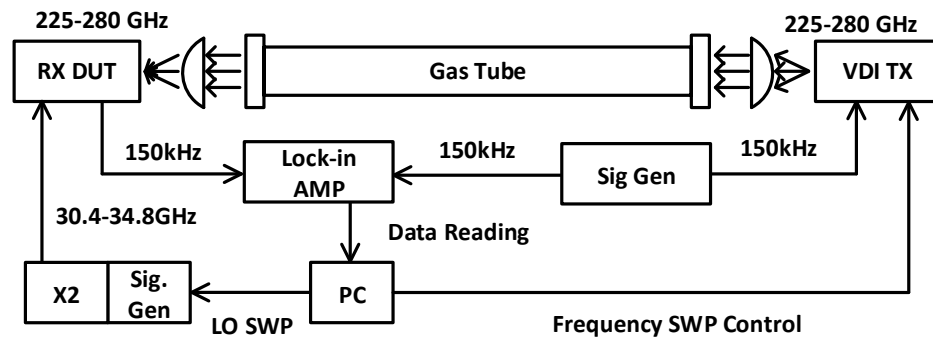
Figure 2.45   Block diagram of spectrometer measurement setup.
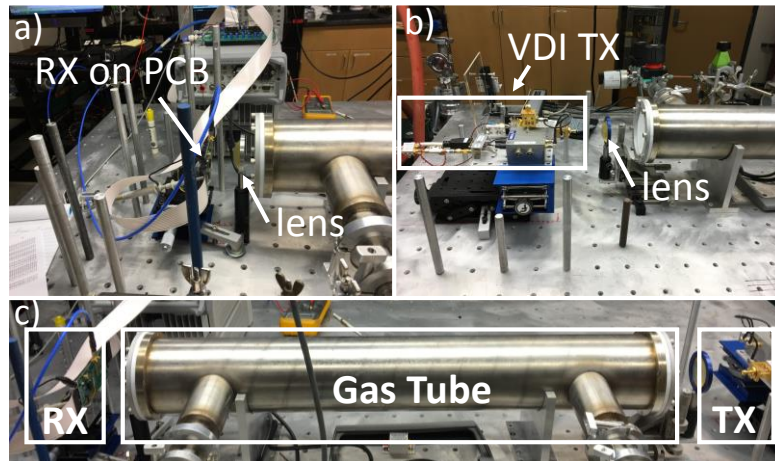
Figure 2.46   Measurement setup for rotational spectroscopy. (a) RX under test, (b) VDI TX, (c) complete setup.

absorption cell containing a gas sample. At the far end of the cell, the wave is focused on the receiver using the second lens. The use of lenses also reduces the propagation loss. The VDI TX is frequency-modulated (FM) at 150 kHz. When the signal interacts with gas molecules, FM to AM conversion occurs [5]. Because of this, the RX picks up an amplitude modulated signal. This conversion effectively differentiates the spectrum with respect to frequency, which helps to remove the baseline variation due to the in-band variation of the RX and TX characteristics and the standing wave effect.

The measured spectrum of Acetone is shown in Figure 2.47. The cell was scanned from 235 to 250 GHz. As shown in the graph, the spectrum was taken using the CMOS RX and VDI TX match well with the OSU Acetone reference library (bottom). The spectral lines around 240
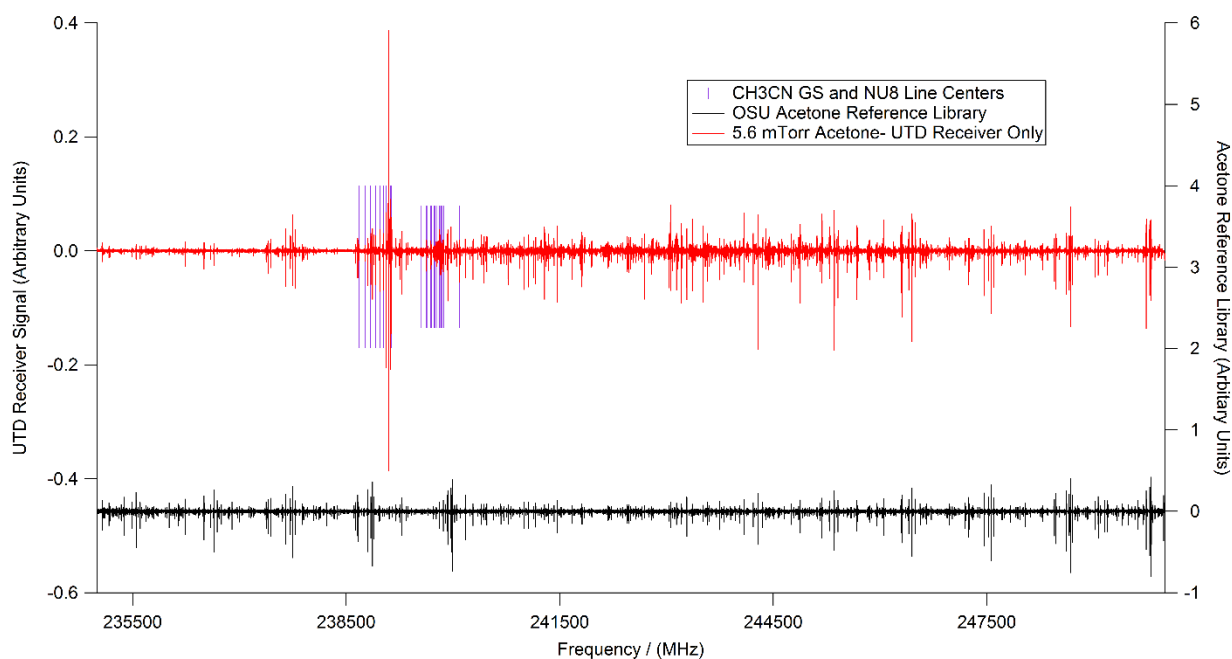
Figure 2.47   Spectrum of 5.6 mTorr Acetone with CH$_3$CN contamination.

GHz overlayed with lighter shaded lines, which in the cell are the known spectral lines of residual CH_3CN.

Figure 2.48 shows the measured snippets of Ethanol spectrum overlayered with the JPL reference library and OSU library. The frequency measurement accuracy is limited by the spectral line widths to about 50 kHz and the amplitude accuracy by the noise floor is visible in the plot. The receiver not only detected Ethanol lines at 5.2-mTorr, it also detected acetone and EtCN contaminants which are all at much lower concentration levels than that of Ethanol.
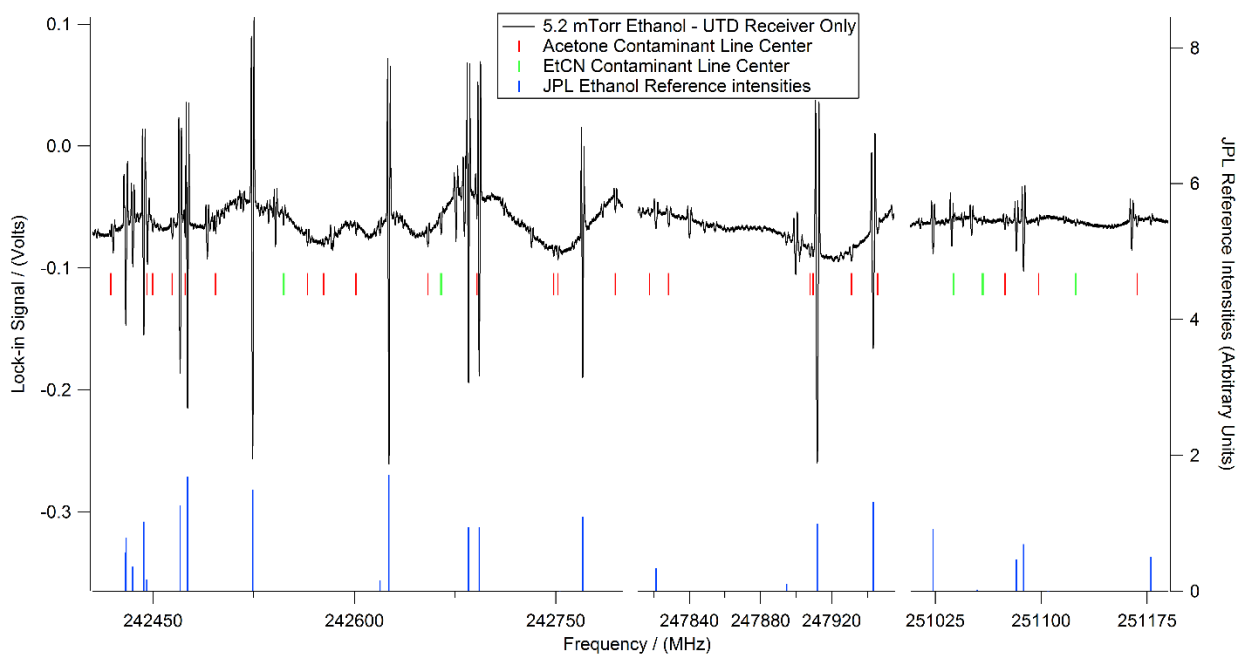
Figure 2.48   Spectrum of 5.2mTorr ethanol with EtCN and acetone contaminants.

2.7 Summary and Conclusion

A 225-280 GHz receiver for rotational spectroscopy fabricated in 65-nm CMOS is demonstrated. The receiver was used in a rotational spectrometer to detect gas molecules in a mixture, demonstrating for the first time that a CMOS receiver can be used for rotational

spectroscopy. Furthermore, this work also demonstrated that a CMOS circuit operating at 225 to 280 GHz can support an existing application. This is an important step toward realizing an affordable rotational spectrometer.

CHAPTER 3

TRANSMITTER DESIGN FOR DIELECTRIC WAVEGUIDE COMMUNICATION

3.1 Introduction

High speed, low cost, and low overhead interconnects in current electronic systems fall into three general categories: electrical, optical and wireless. The electrical interconnects are the most widely used which are found in almost every electronic device. The state-of-art electrical interconnects achieve a data rate up to 60Gbps (Gigabits per seconds)[37] [38] [39] over a 0.7-meter long Twinax cable. At this high data rate, the transmission line becomes lossy (up to 20 dB [37]). Dispersion and impedance mismatch also become serious problems. To circumvent these issues, the communication distance is limited to less than 1meter, an expensive cable like Twinax is used, and on the design level, sophisticated equalization techniques must be adopted. All these added together to make an electrical link expensive and fragile. On the other hand, optical fibers do not suffer from the bandwidth limitation and signal cross-talk. However, the additional optical device makes integration difficult. Recent advances of process technology have made wireless connection an interesting and promising option. The maturing of millimeter wave and sub-millimeter wave technologies enable operation of circuits at hundreds of gigahertz where a large bandwidth is readily available. Additionally, with the development of low-cost plastic waveguide, the channel can be significantly improved over that of electrical links and both the communication distance and fidelity can be improved.

Exploiting these, communication over a dielectric waveguide with a loss of less than 10dB/m has been proposed to meet the ever-increasing bandwidth demand [40], [41].

3.2 System Definition

In support of the high data rate communication over the dielectric waveguide, a transmitter supporting 30 Gbps single channel communication through a dielectric waveguide is demonstrated. The conceptual diagram of this link is shown in Figure 3.1. The transmitter accepts an unmodulated digital signal and then modulates the digital codes onto a 315GHz carrier. The carrier transmits over a dielectric waveguide and picked up by a receiver on the other side of the waveguide. The link should be low-power while maintaining a competitive high data rate at a given bit error rate.
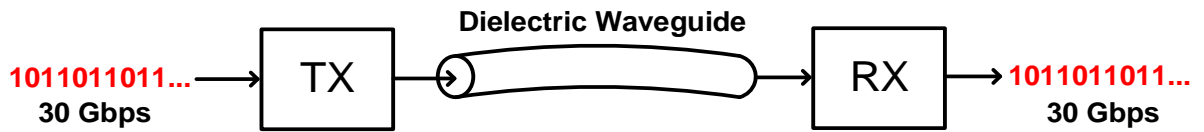
Figure 3.1   Conceptual diagram of dielectric communication system

3.3 MSK Modulation

In sections 3.1 and 3.2, it was mentioned that the core limiting factor for the electrical link is the bandwidth/data rate and power consumption, while for an optical link is the difficulty of system integration. Thus, the data rate and power consumption are the ultimate targets for transmitter design. At millimeter-wave frequencies, binary on-off keying (OOK) modulation is a popular option because of its simplicity [42] [43] [44] [7]. However, OOK is not bandwidth efficient as shown in Table 3-1 and it requires a higher signal-to-noise ratio to maintain a given symbol error rate than phase modulation. In fact, M-phase modulation (M-PSK) is inherently superior to M amplitude modulation (M-ASK).

QPSK modulation [8],[45],[46] is another popular option. Compared to OOK modulation, it almost doubles the maximum achievable data rate and at the same data rate, it also does not post a stringent noise requirement for the receiver as the OOK modulation. However, QPSK has the main drawback of high side lobe emission. To understand its negative effects, different bandwidth definitions are revisited. The first is called null-to-null bandwidth efficiency, which is defined to be the width of the main spectral lobe. Another useful definition is percentage bandwidth efficiency which is defined as how much percentage of total signal energy is contained within the certain bandwidth. This percentage is usually chosen to be 90% or 99%. As seen in Table 3-1, the null-to-null bandwidth of QPSK modulation is R_b or the data rate while the 99% bandwidth of QPSK modulation is $10R_b$. This means that there's a lot of energy in its side lobe spectrum. If not properly filtered, this energy will be leaked to adjacent channels and corrupt the signal in the other

Table 3-1   Comparison between different modulation scheme

Modulation	BW (null to null)	BW (90%)	BW (99%)	Efficiency (bits/s/Hz)	Eb/No* (dB)
OOK	$2R_b$**	-	-	1	15
BPSK	$2R_b$	$3.4R_b$	$20R_b$	1	12
BFSK	$3R_b$	$2.46R_b$	$4.24R_b$	0.67	15
QPSK	R_b	$1.7R_b$	$10R_b$	2	12
MSK	$1.5R_b$	$1.52R_b$	$2.4R_b$	1.3	12
16-QAM	$0.5R_b$	-	-	4	15.5
*assuming the same symbol error rate of 10^{-7} for different modulation scheme and coherent detection if possible. ** R_b is the bit rate.					

channels. This brings a lot of design challenges for a system using multiple channels. Another issue of QPSK modulation is that its envelope is not constant which usually means the power amplifier design for a transmitter is harder since the power back-off efficiency is low. To support a non-constant envelope modulation while maintaining high power efficiency, a complicated power amplifier architecture like Doherty or digital pre-distortion (DPD) is a must. However, these techniques are very difficult to use at high frequencies and for high data rate applications. After balancing these three key design targets: 1. bandwidth efficiency, 2. multi-channel capability, 3. power efficiency, minimum phase shift keying (MSK) is found to be the best suited.

Like QPSK, MSK is just a special case of quadrature phase shift keying with some weighting factors. Consider a simple QPSK signal:

$$s_{QPSK}(t) = A_I(t)\cos(2\pi f_c t) + A_Q(t)\sin(2f_c t) \tag{3.1}$$

where A is the amplitude of carrier signal and $I(t)$, $Q(t)$ are the baseband I-Q digital codes. Based on this, we can also define offset QPSK (OQPSK) by shifting one of the baseband signals by a bit period:

$$s_{OQPSK}(t) = A_I(t)\cos(2\pi f_c t) + A_Q(t-T)\sin(2f_c t) \tag{3.2}$$

MSK takes one step beyond OQPSK modulation by shaping the baseband signal by a sinusoidal signal with a specific frequency of 1/4T which is a quarter of the bit rate:

$$s_{MSK}(t) = A_I(t)\cos(\frac{\pi}{2T}t)\cos(2\pi f_c t) + A_Q(t-T)\sin(\frac{\pi}{2T}(t-T))\sin(2f_c t) \tag{3.3}$$

To better understand the special properties of the MSK signal, Eqn.(3.3) can be rewritten in a different form [47]. It is obvious that in the kth bit period of T seconds, $I(t)$ and $Q(t)$ is either 1 or -1, we denote them as I_k and Q_k, thus

$$s_{MSK}(t) = A\cos(2\pi(f_c + d_k \frac{1}{4T})t + \varphi_k), \quad kT \leq t \leq (k+1)T \tag{3.4}$$

where $d_k=1$ when I_k and Q_k have opposite signs and $d_k=-1$ when I_k and Q_k have same signs. Or equivalently

$$d_k = -I_k Q_k \tag{3.5}$$

$\varphi_k =0$ or π corresponding to $I_k =1$ or -1. Or equivalently

$$\varphi_k = \frac{\pi}{2}(1 - I_k) \tag{3.6}$$

Both d_k and φ_k are constant in a bit period of T seconds since I_k and Q_k are constant in T. Eqn. 3.4 indicates that MSK modulation can be treated as a special case of FSK modulation with two frequencies $f_+ = f_c + 1/4T$ or $f_- = f_c - 1/4T$. The frequency separation is $\Delta f = 1/2T$. The correlation of signals at those two frequencies is:

$$\int_{kT}^{(k+1)T} \cos(2\pi(f_c + \frac{1}{4T})t + \varphi)\cos(2\pi(f_c - \frac{1}{4T})t + \varphi) = 0 \tag{3.7}$$

These two signals are orthogonal. In fact, $\Delta f = 1/2T$ is the minimum separation for two FSK signals to be orthogonal, hence the name minimum shift keying.

From Eqn. (3.4), the envelope of MSK signal is constant no matter the bits. Second, the phase is continuous as bit transitions. There are no abrupt phase changes at bit transitions like in QPSK or OQPSK signals. Third, the signal is an FSK signal with two different frequencies and with a symbol duration of T. The above equations are graphed as signal waveforms in Figure 3.2(a). From the waveform, the constellation as shown in Figure 3.2 can be constructed. As we can see, the phase rotation changes its direction only at 0 degree, 90 degree, 180 degree, 270 degree points and within each bit period, the phase linearly increases or decreases. Thus, the overall constellation

including transitions forms a circle. The constant envelope property of MSK modulation makes it favorable for PA design because PA does not need to be backed-off while supporting a decent bandwidth efficiency and IQ demodulation capability.
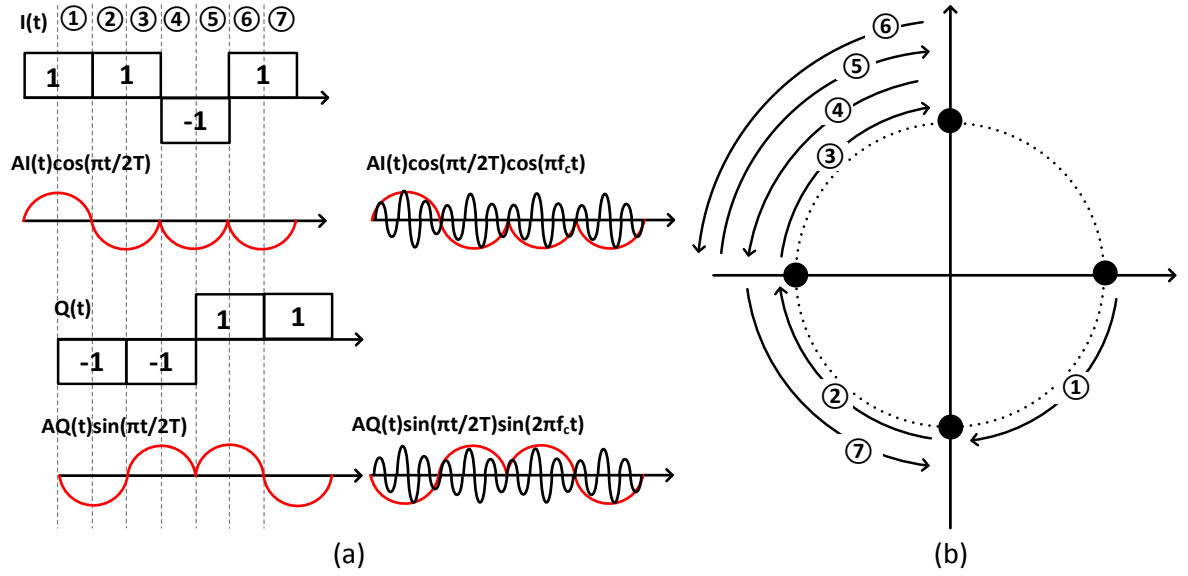
Figure 3.2   (a) MSK I-Q signal waveform (b) MSK constellation

3.4 Transmitter Architecture

Transmitter architecture for the proposed dielectric waveguide communication system is shown in Figure 3.3. The frequency band between 157.5 and 382.5 GHz is channelized into five 45-GHz bands that support horizontal and vertical polarization communication modes for a total of 10 channels. With a data rate of 30-Gbps per channel, the aggregate data rate is 300-Gbps. The
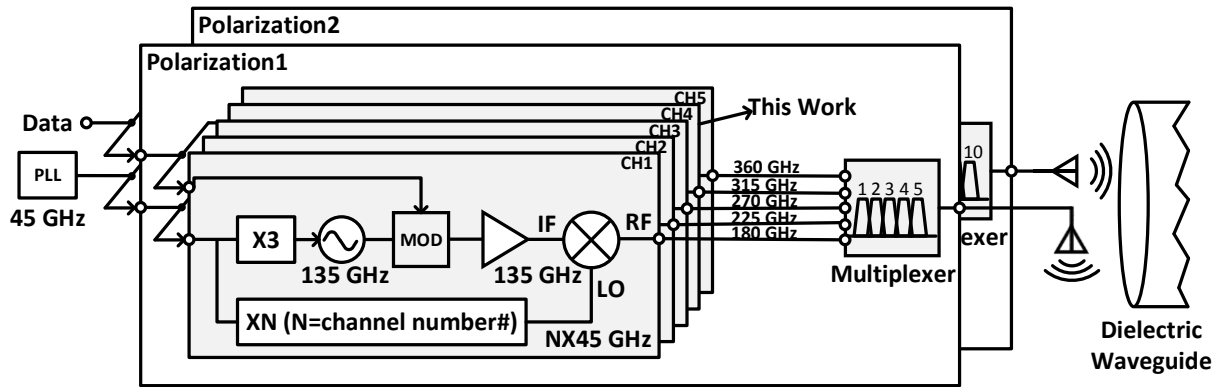
Figure 3.3   Transmitter architecture (CH4 is implemented in this work)
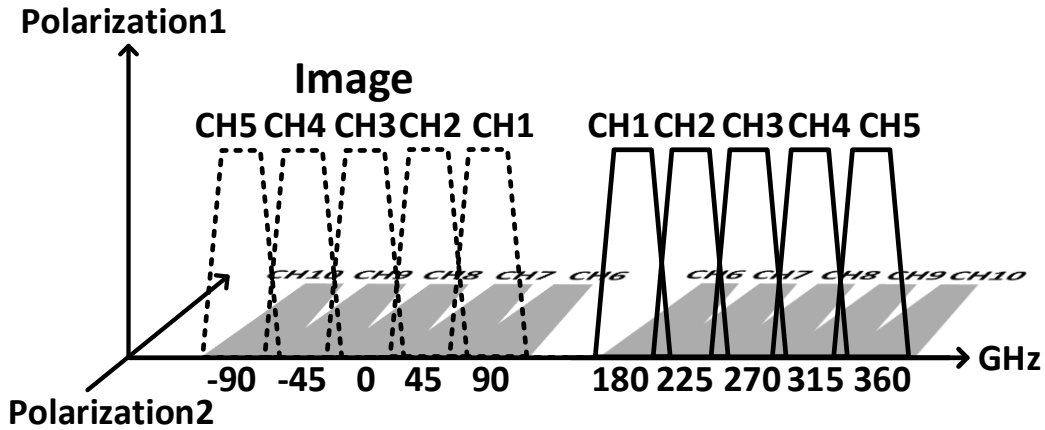
Figure 3.4   Frequency plan of transmitter.

transmitter chains are identical except for a different frequency multiplication factor to generate

the local oscillator signal for an up-conversion mixer that generates the RF output signal as well

as RF matching. A quadrature modulator superimposes the digital input onto 135-GHz outputs of

a quadrature voltage controlled oscillator (QVCO) stabilized by injection locking. The modulated

signal at 135 GHz is then amplified by a wideband (40 GHz bandwidth) power amplifier and up-

converted to generate the RF output. The outputs of transmitters are combined using a multiplexer

71
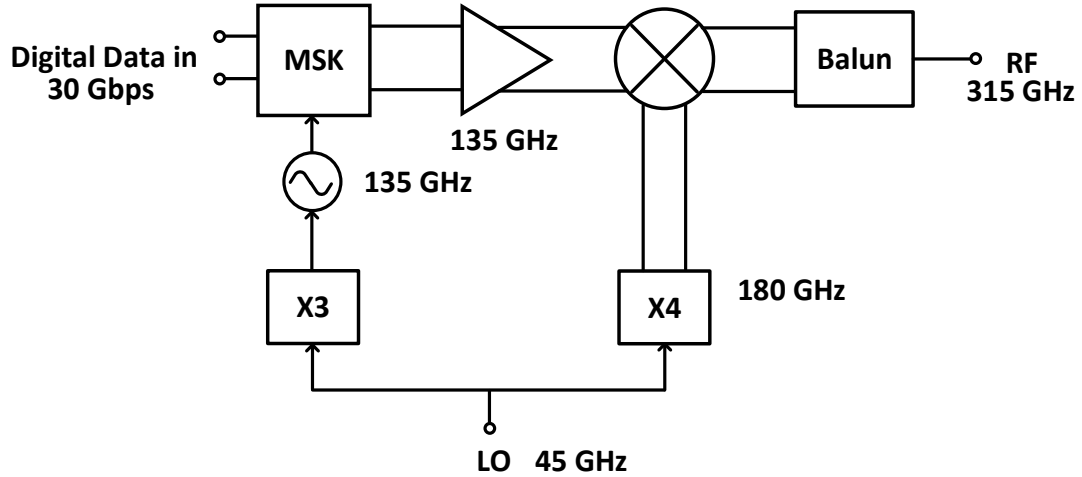
Figure 3.5   MSK transmitter architecture

and fed to a transition for the waveguide. Two sets of five transmitters are used to support both vertical and horizontal polarization modes. The carrier frequencies are separated by 45 GHz and only one narrow-band integer-mode phase locked loop (PLL) is needed. The frequency plan including images is shown in Figure 3.4. Compared to [48], [49], the use of a higher frequency modulator and the frequency plan in Figure 3.4 eliminates the need for a single side-band (SSB) mixer or an image rejection architecture for a more compact and energy efficient realization.

The detailed single channel transmission architecture is shown in Figure 3.5. It is based on a traditional heterodyne up-conversion structure. MSK modulator takes 30-Gbps digital data and modulates them onto the 135-GHz signal. A wideband buffer amplifier the 135-GHz modulated data. The up-conversion mixer is driven by a 180-GHz LO signal and final RF output is at 315 GHz. In this architecture, the input LO frequency is chosen to be 45 GHz. The 135-GHz and 180-GHz LO signal for the up-conversion mixer both are integer multiples of input LO frequency

Table 3-2   Targeted Specification of MSK Transmitter

Specification	Value
Modulation Type	MSK
Bit Rate	30 Gbps
Data bandwidth	50 GHz
Final Carrier frequency	315 GHz
Modulator Frequency	135 GHz
LO frequency	180 GHz
Output Power	-5 dBm
Output Interface	Probe
Total Power Consumption	180 mW

.

For modulation at 135 GHz, an on-chip quadrature voltage controlled oscillator (QVCO) is implemented as a power efficient option to provide the I-Q signal. This QVCO is injection locked to an off-chip 45-GHz LO signal through an on-chip tripler. The tripler output power can be low enough to just lock the on-chip QVCO so that the whole 135-GHz I-Q generation is power efficient. For the 180-GHz LO signal up-conversion, the off-chip 45 GHz LO signal is frequencily multiplied by 4 using an on-chip multiplier chain. The front-end consists of a 315-GHz up-converting mixer and an on-chip Marchand Balun for the differential to single-ended conversion.

MSK modulator and its buffer design are the key challenges because of the high data rate. As summarized in Table 3-1, for 30-Gbps MSK modulation, the null to null bandwidth should be

at least $1.5R_b$ or 45 GHz. For 90% energy bandwidth, it should be 45.6 GHz. To leave some design margin, we set the design target for the bandwidth of this buffer is 50 GHz. At the center frequency of 135 GHz, this means the amplification frequency spans from 110 to 160 GHz. The detailed specifications of the MSK transmitter are summarized in Table 3-2.

3.5 Circuit Components

3.5.1 MSK Modulator Design

The MSK modulator design can be very straightforward and intuitive. Eqn. (3.3) indicates that the modulation can be accomplished by upconverting the sine-shaped digital data. The conceptual diagram of the MSK modulator is shown in Figure 3.6. On the bottom of each channel, there is a pair of switches driven by digital I and Q codes. When an incoming digital code is 1, the
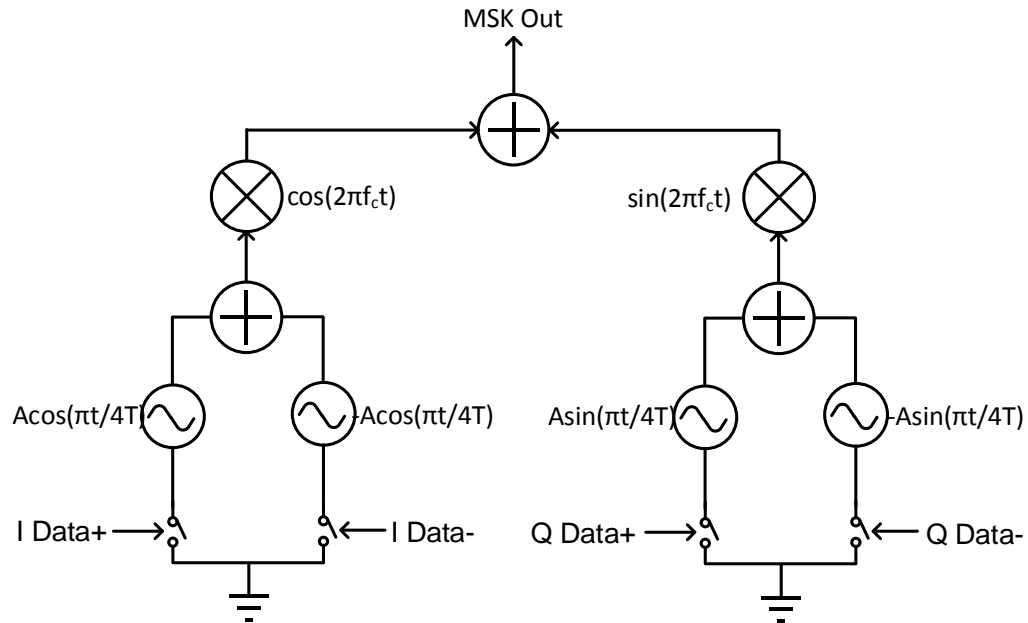
Figure 3.6   Conceptual diagram of MSK modulator

left branch will be connected and shaping signal Acos(πt/4T) will mix with the carrier signal, cos(2πf$_c$t). When an incoming digital code is 0, the right branch will be connected and shaping signal -Acos(πt/4T) will mix with the carrier signal cos(2πf$_c$t). The Q-channel operates in the same way as the I- channel. The outputs are finally added to produce the complete MSK modulation output.

Based on the above description, the digital codes control can be regarded as a "polarity switcher" that toggles the shaping signal from 0 degree to 180 degree. Therefore, the MSK modulator consists of 3 key building blocks: polarity switcher, adder, and up-converting mixer.
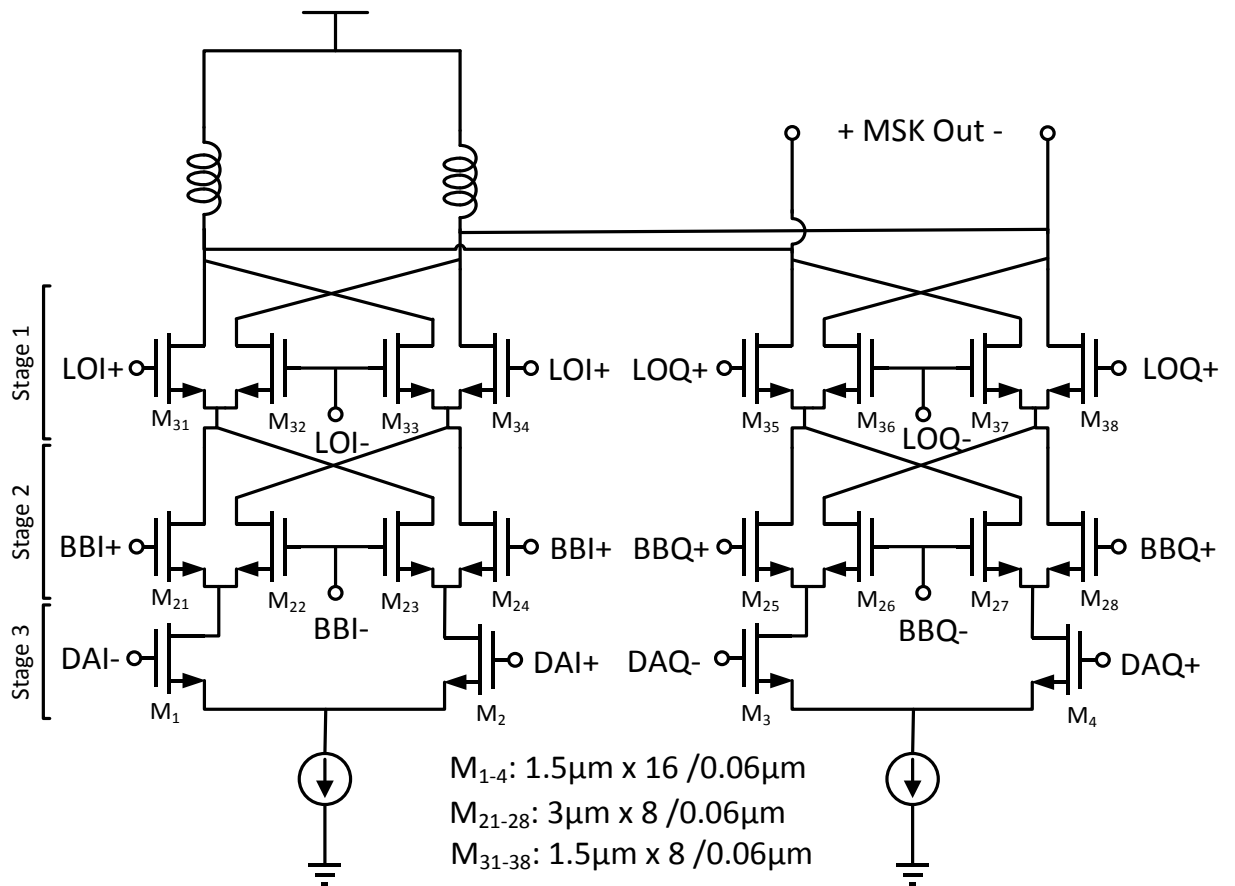
Figure 3.7   MSK modulator circuit diagram

To achieve high data rate operation, the speed of "polarity switcher" should be high and current mode logic (CML) [50] is a good choice since it gets rid of the "slow" PMOS device and its differential operation minimize the deleterious effect of power-ground bounces. The adding functions can be all done in current domain resulting in a simple shunt connection and a high operating bandwidth. The up-converting mixer unit needs to have sufficient LO/IF leakage suppression since both IF and RF will have a frequency rich spectrum, a double-balance Gilbert cell can fulfill these requirements. The complete MSK modulator circuit diagram is shown in Figure 3.7. Two current mode logic (CML) double balanced switches toggle the current between the two differential trans-conductors in a waveform shaping stage controlled by the CLK signals. When CLKI+/Q+=DC, CLKI-/Q-=0, the shaping stage together with the data switch stage forms cascode current switchers and the circuit works as a QPSK modulator. If one of the branches (e.g. I or Q branch) is shut off, the circuit works as a BPSK modulator. If sinusoidal waves are provided at shaping stage, it works as MSK modulator. The stage-1 is a double balanced-Gilbert cell mixer whose LO (labeled as LOI+ and LOI-) are driven by the 135 GHz I-Q signal generation. This stage serves as a mixer to mix the carrier signal with the baseband modulation signals. The stage-2 is another double-balanced Gilbert cell whose gates are connected to sinusoidal shaping signal (labeled as BB+ and BB-), instead of mixing, this stage is, in fact, a voltage to current conversion stage (V-I converter) which converts shaping signal voltage to current. The stage-3 is the "polarity switcher". If the switches (M_1, M_2 or M_3, M_4) are open at the same time, stage-2 will have no AC output. The shaping signal acts as the LO to the stage-2, and the double balanced structure suppresses LO, thus, no shaping signal is produced at the output of stage 2. However, this situation never occurs in real operation since the fully differential nature of polarity switcher controlled
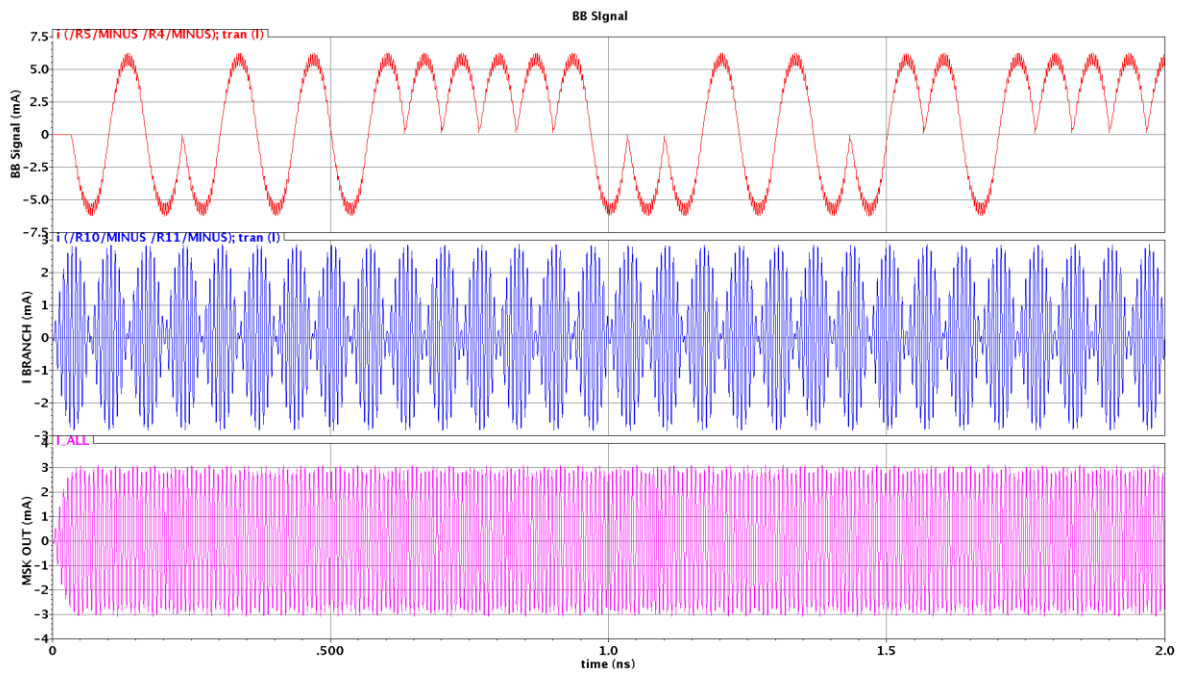
Figure 3.8   Simulated waveform of key nodes of MSK modulator circuits
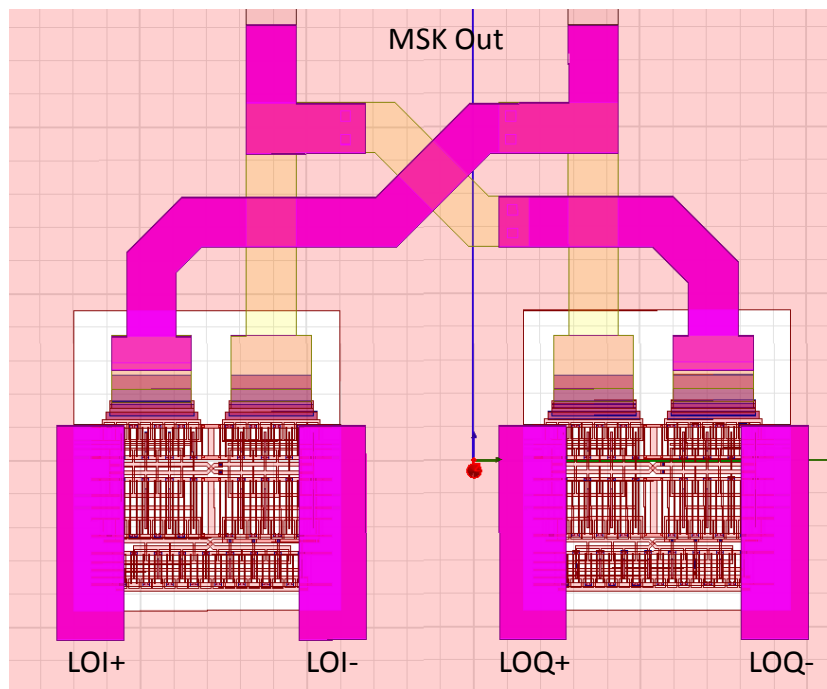
Figure 3.9   MSK modulator HFSS parasitic extraction

by DAI+ DAI- makes sure the switcher waveforms are non-overlapping. Thus, only one switch will be turned on at a time, toggling the shaping signal of stage 2 from in phase to out of phase. Simulated signals of key nodes are shown in Figure 3.8, where I branch is the single I branch current waveform taken from stage 1, BB signal is the output current waveform taken from stage 2 and MSK Out is the combined waveform of I-Q branch currents.

The layout of the MSK modulator needs to be carefully planned due to the high data rate. As shown in Figure 3.9, I-Q branches are drawn symmetrically using the identical layout cells to minimize mismatches. The stage 1, stage 2 and stage 3 shown previously in Figure 3.7 are merged along to minimize the lengths of inter-stage connection lines which also makes the floorplan compact to help reduce the parasitic effects brought by a larger area. The whole layout structure is simulated and verified using HFSS and included in the simulation. The MSK modulator after parasitic extraction shows good performance up to 30-Gbps in the simulation.

3.5.2 Wideband Data Buffer Design

The data buffer designs is another challenge. As discussed in the previous section, the MSK modulator is essentially two Gilbert cell mixers stacked. It is well known that a Gilbert cell is a representative of passive switching mixers and has a theoretical loss of about 6-dB. Recalling that the MSK modulator carrier is at 135 GHz, and the overall output power of the modulator is nowhere sufficient to drive the 2nd stage mixer. In fact, the simulated output power of the MSK modulator is around -15-dBm~-20-dBm, with the last stage up-conversion loss to 315 GHz of more than 10dB. The final output power without dedicated pre-amplification will be less than -20-dBm, which is far below the specification in Table 3-2. Thus, to achieve the goal of -5-dBm output

power, a wideband buffer providing at least 20-dB power gain over entire the data bandwidth is needed. Because of the wide bandwidth of data, the gain has to be flat over the bandwidth to avoid inter-symbol-interference (ISI).

Another key requirement for this power amplifier is the group delay. The group delay is the transit time for a signal through a communication channel [51]. Ideally, the transit time should be constant so that all frequency components of the transmitted signal experience the same time lag. If the transit time is not constant, the modulation components of the signal extending to the band edge experience an increased or decreased delay relative to others. If this delay variation is not negligible, adjacent symbols run into each other and energy may exist at the sample instant of one symbol that is associated with an adjacent symbol. Requirements for the wideband data buffer are specified in Table 3-3.

Table 3-3   Wideband Data Buffer Specification

Specification	Value
Bandwidth	50 GHz (110-160 GHz)
In-band Gain Flatness	<2-dB ripple
In-band Group Delay Variation	< 5%
Power Gain	> 20-dB
Saturated Output Power	~10-dBm
Output Gain Compression Point	>10-dBm

Based on these requirements, number of gain stages needed must be determined. It is well known that CMOS transistors suffer from a significant power gain degradation when operating frequency approaches f_{max}. To increase power gain at operating frequency above 100 GHz,
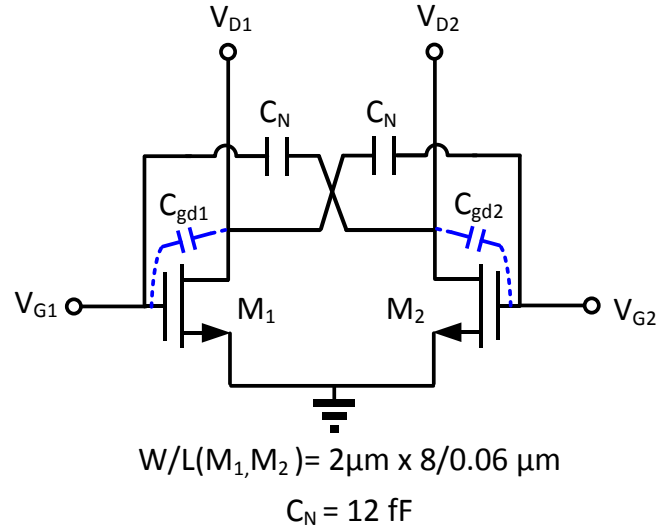
Figure 3.10   Differential pair using a neutralization technique.

capacitive neutralization widely utilized [52],[53],[54],[55]. In Figure 3.10, neutralization is accomplished by basically capacitively cross-coupling two transistors M_1 and M_2 with neutralization capacitance C_N. If the value of C_N is chosen correctly, it will create a negative capacitance looking into node V_{G1} or V_{G2}, canceling the intrinsic parasitic gate to drain capacitance $C_{gd1,2}$, resulting in a capacitive neutralized differential pair. Effectively, the neutralization techniques eliminate the feedback through parasitic capacitances $C_{gd1,2}$. This has at least two significant advantages. Firstly, the deteriorative "Miller Effect" that multiplies the first-order input time constant with the small signal transistor gain will be reduced [56]. This boosts the high-frequency gain of the differential pair. In fact, in this case, the gain of transistor approaches the maximum stable gain (MSG), the maximum achievable gain under stability constraints in most cases [57] (the gain of transistors is close to unilateral power gain in practical design for stability concern). Secondly, because of the elimination of feedback capacitances $C_{gd1,2}$, the transistor becomes more "unilateral", which makes it much easier to stabilize when input and output
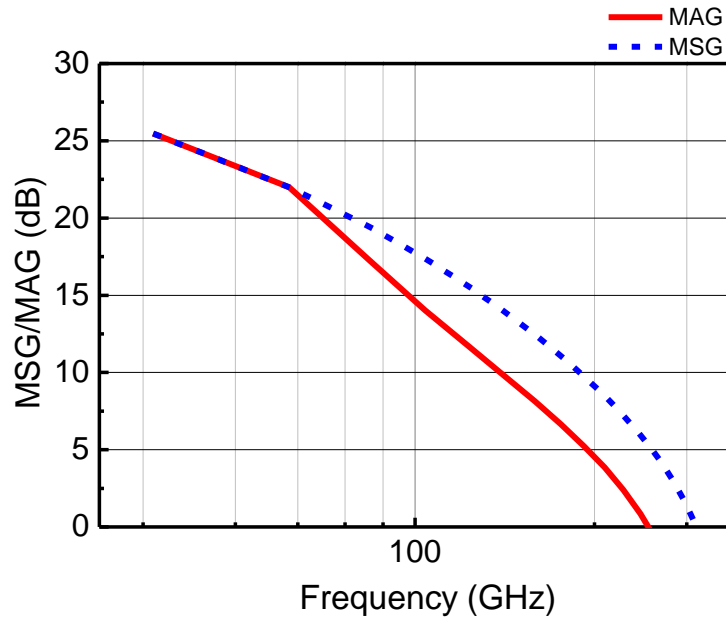
Figure 3.11   MSG and MAG of neutralized differential transistor pair with C_N=9fF
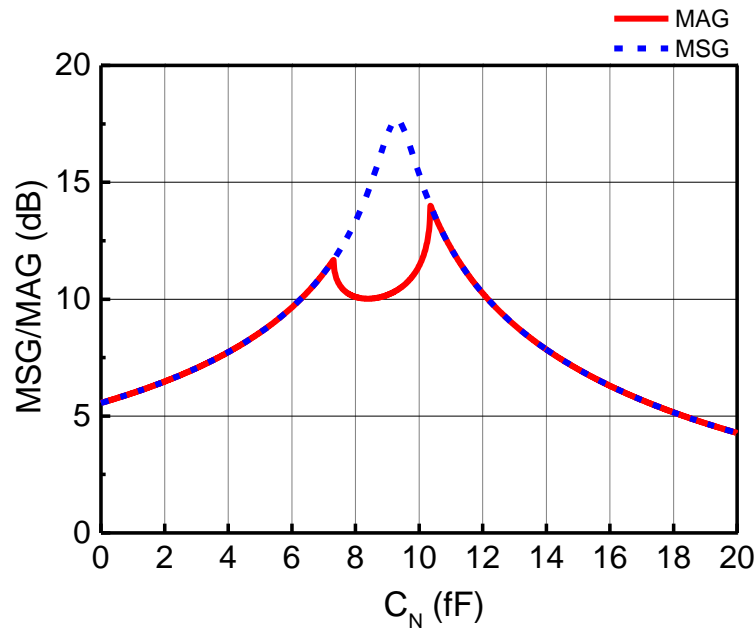
Figure 3.12   MSG and MAG versus neutralization capacitance at 135 GHz

matching networks are connected. As shown in Figure 3.11, the maximum available power gain

(MAG) and maximum stable power gain (MSG) curve overlap with each other until around 70 GHz, above 70 GHz, MAG curve is lower than MSG curve. Recalling that

$$MAG = \begin{cases} MSG, \text{ when k<1} \\ \left| \dfrac{S_{21}}{S_{12}} \right| (k \pm \sqrt{k^2 - 1}), \text{ when k} \geq 1 \end{cases} \qquad (3.8)$$

It can be seen that Kurokawa's stability factor k [58] is greater than 1 for frequencies greater than 70 GHz, indicating that the differential transistor pair becomes unconditionally stable beyond 70 GHz. The effectiveness of neutralization technique is shown in Figure 3.11. The MAG of differential transistor pair peaks when C_N is chosen to be around 10-fF. Compared with no neutralization (C_N=0-fF), MAG is 5 dB higher. It is important that C_N is between 6.5-fF to 10-fF. Based on Eqn. (3.8), the MAG curve overlaps with the MSG curve when k <1. As shown in Figure 3-10, for C_N < 6.5-fF or C_N >10-fF, the MAG curve becomes the same as MSG indicating k<1 and the differential pair is conditionally stable.

Although neutralization greatly mitigates the gain and stability challenges of wideband data buffer design, it does not address its strong frequency dependence on MAG. As seen in Figure 3.11, in the design frequency range of 110-160 GHz, MAG drops monotonically with frequency from 12-dB to 8-dB. In this situation, the gain curve of the amplifier is not flat due to the intrinsic gain drop slope at this frequency range. The matching needs to be done in a way to counter this effect. To solve this problem, use of a coupled resonator [59],[60],[61],[62]as inter-stage matching elements is proposed. The basic configuration of the coupled resonator is shown in Figure 3.13, C_1 and L_1 form the resonator 1 and C_2 and L_2 form the resonator 2. They both resonate at their own resonating frequency. With either an inductor (L_2) or capacitor (C_2) bridging these two resonators
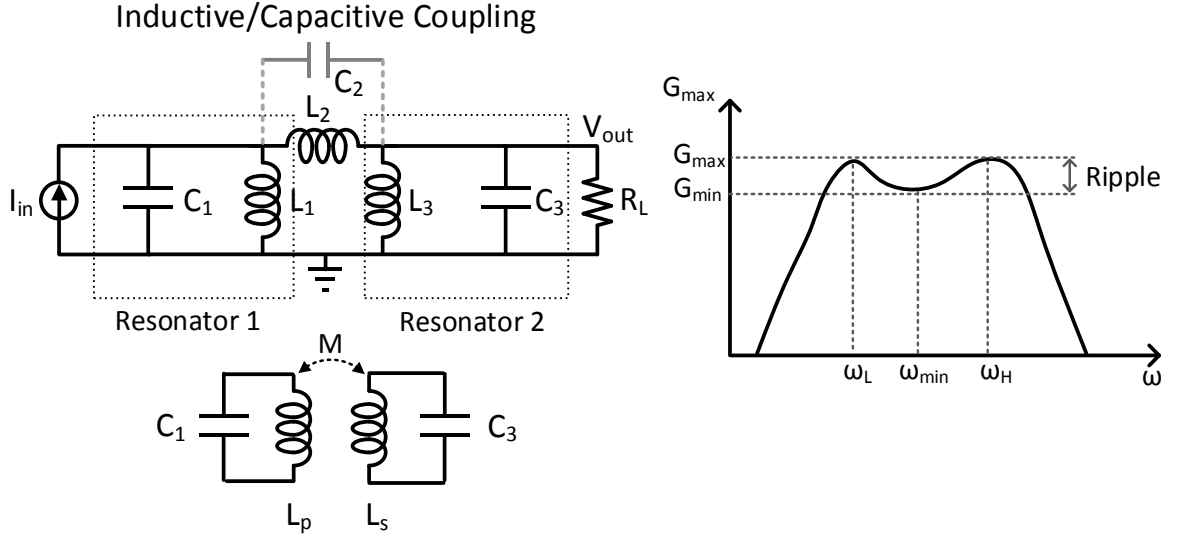
Figure 3.13   Coupled resonator: inductive/capacitive and its gain plot

together, a coupled resonator is formed. Based on the type of coupling components, it can be an inductively coupled resonator (ICR) or a capacitively coupled resonator (CCR). An ICR is of particular interests as the three inductor L_1, L_2 and L_3 shown together in Figure 3.13 is a "π" model of a transformer. Therefore, the ICR can be potentially realized using two capacitors and a single transformer. The frequency response of ICR is very similar to Chebyshev band-pass filter with two poles located at ω_L and ω_H. The gain of the network peaks at pole location creating an in-band ripple. According to [62], the gain of this network, V_{out}/I_{in} is

$$\frac{V_{out}}{I_{in}}(s) = \frac{kQ\dfrac{s}{\omega_0}\sqrt{R_s R_L}}{(\dfrac{Q}{\omega_0}s^2 + \dfrac{1}{\omega_0}s + (1-k)Q)(\dfrac{Q}{\omega_0}s^2 + \dfrac{1}{\omega_0}s + (1+k)Q)} \tag{3.9}$$

From Eqn.(3.9), the transfer function contains two pairs of conjugate poles at

$$\omega_{L,H} = \frac{1}{\sqrt{L_pC_1(1-k^2)}}\sqrt{1-\frac{1}{2Q^2}\pm\sqrt{(1-\frac{1}{2Q^2})^2-(1-k^2)}} \qquad (3.10)$$

in the above equation, Q of each resonator is normally high, Eqn. (3.10) can be reduced to

$$\omega_{L,H} = \frac{1}{\sqrt{L_pC_1(1-k^2)}}\sqrt{(1\pm k)},\ k=\frac{M}{\sqrt{L_pL_s}}\ \text{and}\ L_pC_1=L_sC_2\ \text{(critical coulping)} \qquad (3.11)$$

In the critical coupling condition described in Eqn. (3.10) and Eqn. (3.11). ω_L and ω_H are strongly related to transformer the coupling coefficient k. The low frequency and high-frequency pole locations with respect to the transformer coupling ratio k is shown in
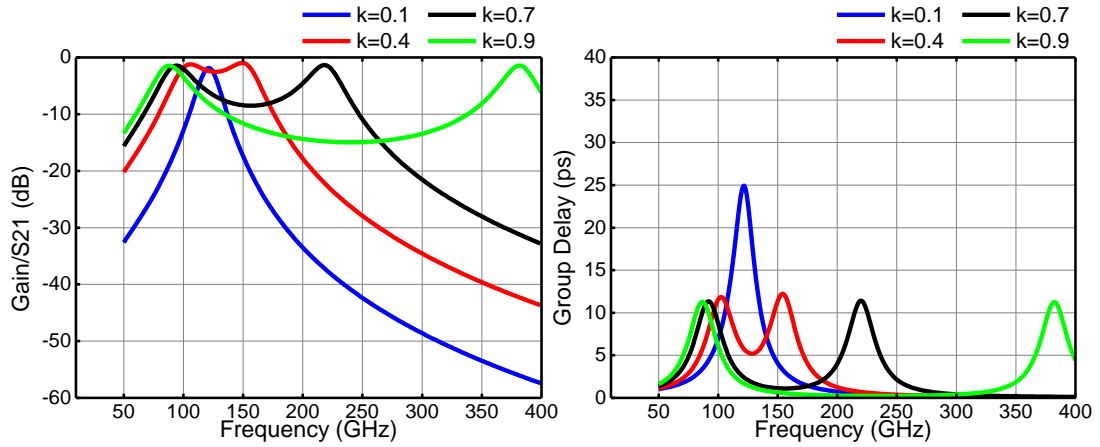
Figure 3.14   Transformer with varying coupling coefficients

Figure 3.14. From this plot, it is clear that the typical transformer matching with a moderate to high coupling coefficient k is a special case of a wideband coupled resonator. With relatively large k (e.g. k=0.6), ω_L and ω_H will have relatively large frequency difference, we can calculate their ratio using Eqn. (3.11)

$$\frac{\omega_H}{\omega_L} = \sqrt{\frac{1+k}{1-k}}\Bigg|_{k=0.6} = 2 \tag{3.12}$$

Eqn. (3.12) means that if matching is done at one of the pole frequency (e.g. 100 GHz), then the other one is at twice or half of that frequency (e.g. 200GHz or 50 GHz). In many systems, only one pole is used. The other one is pushed way out of the band, therefore, the transformer matching is normally considered as a one-pole band-pass system. On the other hand, if we choose k to be a small number, the ratio in Eqn. (3.12) will be much smaller, and the two poles will come in-band creating a double-peak-like frequency response shown in Figure 3.14(red curve, k=0.4). Eventually, if k is sufficiently reduced (blue curve, k=0.1 in Figure 3.14), the two poles will be very close to each other creating a narrow band-pass response which looks like a single-pole but the out of band cut-off slope is twice (e.g. 40dB/decade stopband rejection) as sharp as those using high coupling coefficients. A coupled resonator provides a good way to expand the bandwidth of inter-stage matching of the amplifier at the expense of a larger in-band ripple. The design procedure of coupled resonator for inter-stage matching [60] is shown in Figure 3.15. Starting with
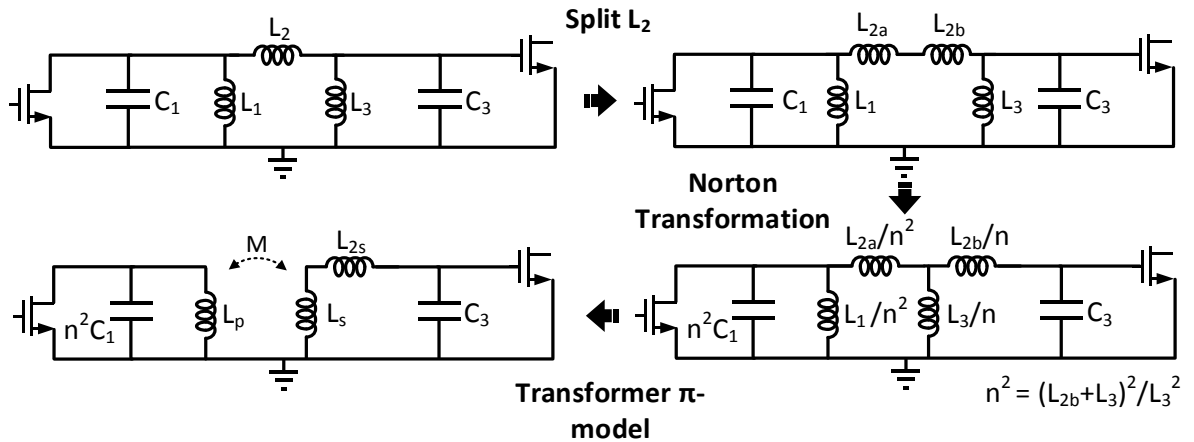
Figure 3.15   Coupled resonator matching design procedure
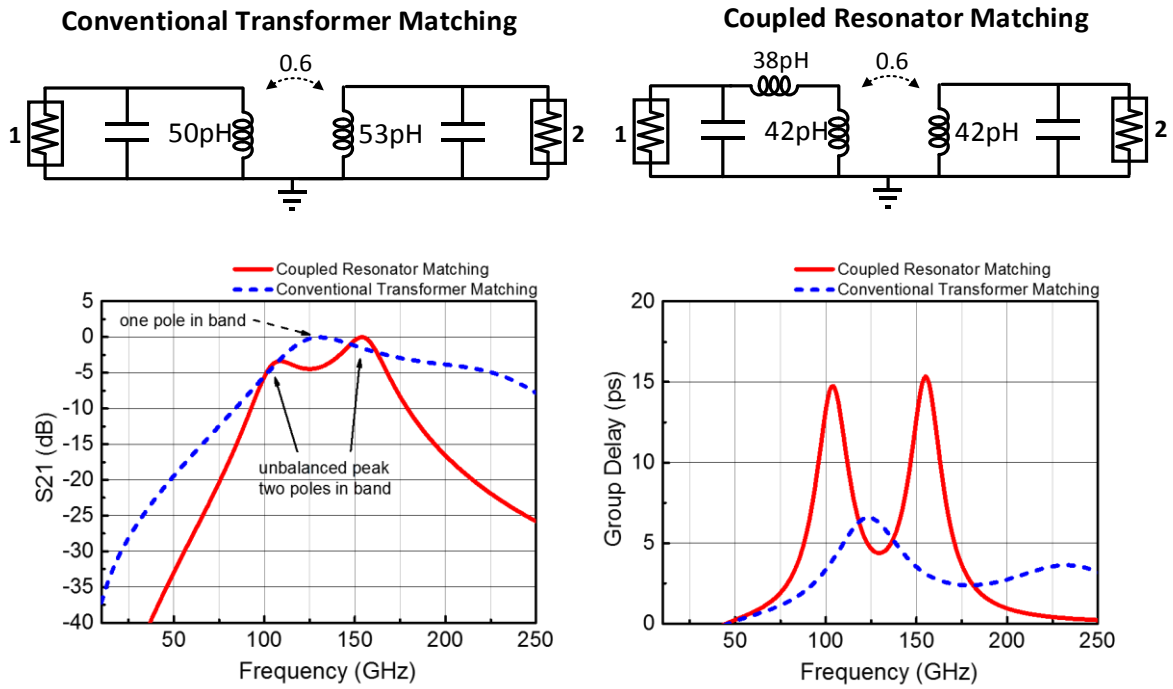
Figure 3.16   Frequency response of two different matching methods

a coupled resonator. Parasitic capacitances of the output transistor and input transistor can be absorbed into lumped capacitors C_1 and C_3. Then the inductor L_2 is split into two inductors L_{2a} and L_{2b}. Next, the Norton impedance transformation is applied and inductor L_{2b} is moved to the right side of L_3. After this transformation, the coupled resonator can be represented as a transformer with a series inductor, in order to make a balanced frequency response of the coupled-resonator structure. For the design in Figure 3.11, the MAG of the transistor has a strong frequency dependence. This approach can be used to deliberately unbalance the two in-band peaks of coupled-resonator to counter the frequency dependence of the transistor. In Figure 3.16, for the same source and load, two different matching methods are used. The one using conventional transformer matching shows signal $|S_{21}|$ transmission peak at the center frequency of 135 GHz while the one using a coupled resonator matching shows dual peaks located at 110 GHz and 160

GHz. The 110-GHz peak is intentionally set to be lower than the 160-GHz peak by 3-dB. This balances the gain drop of the transistor at high frequency. The group delay of these two matching schemes is also very interesting. As is shown in Figure 3.16, whenever there is a pole or transmission peak, the group delay also peaks. From Eqn.(3.9), the phase of the gain transfer function and group delay are

$$\phi(\omega) = 90 - \arctan(Q\frac{\omega}{\omega_0} - (1-k)Q\frac{\omega_0}{\omega}) - \arctan(Q\frac{\omega}{\omega_0} - (1+k)Q\frac{\omega_0}{\omega}) \tag{3.13}$$

$$\tau_{group\_delay} = \frac{d\phi(\omega)}{d\omega} = \frac{\frac{Q}{\omega_0} + (1-k)Q\frac{\omega_0}{\omega^2}}{1 + (Q\frac{\omega}{\omega_0} - (1-k)Q\frac{\omega_0}{\omega})^2} + \frac{\frac{Q}{\omega_0} + (k+1)Q\frac{\omega_0}{\omega^2}}{1 + (Q\frac{\omega}{\omega_0} - (1+k)Q\frac{\omega_0}{\omega})^2}. \tag{3.14}$$

In Eqn. (3.14), that group delay of the network contains two pairs of conjugate poles. A closer examination reveals that the two pairs are located at the frequencies of $\omega \approx \omega_0\sqrt{1-k}$ and $\omega_0\sqrt{1+k}$. These frequencies are the same as the multi amplitude peak points of the coupled resonator. This result can also be understood intuitively. At the pole frequency, the matching achieves local resonance and the phase of transmission coefficient at this frequency is zero. Below or above this frequency, the transmission impedance changes from inductive to capacitive or vice versa. Therefore, the phase change is the largest and sharpest around the pole frequency which leads to the group delay peak because group delay is calculated as the derivative of phase against frequency or in other words, the speed of phase change.

The circuit diagram of the wideband data buffer is shown in Figure 3.17. In this design, there's a total of five stages of matching. Two of them use conventional transformer matching with the center frequency of 135 GHz and the other 3 use a coupled resonator where ω_H and ω_L of coupled-resonator are chosen to be 110 GHz and 160 GHz. The 3 stages of coupled resonator

matching peak at lower and higher end with a significant dip in the middle band, creating large ripples for both gain and group delay. However, the conventional transformer matching has gain and group delay peaks at the center frequency. Therefore, compensating the dip in the middle band. The combination of these two types of matching results in a flat response for both power gain and group delay as shown in Figure 3.18. the gain ripple is less than 2-dB and group delay ripple is less than 4ps for operating frequency range of 110-160 GHz.
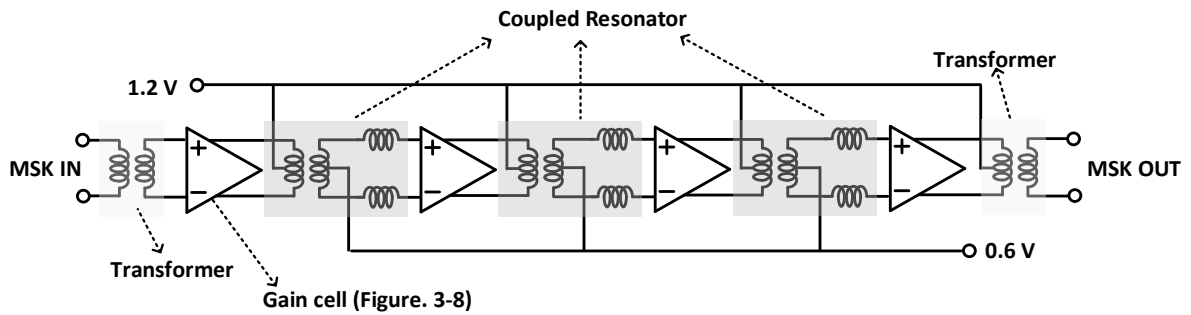
Figure 3.17   Wideband data buffer circuit diagram
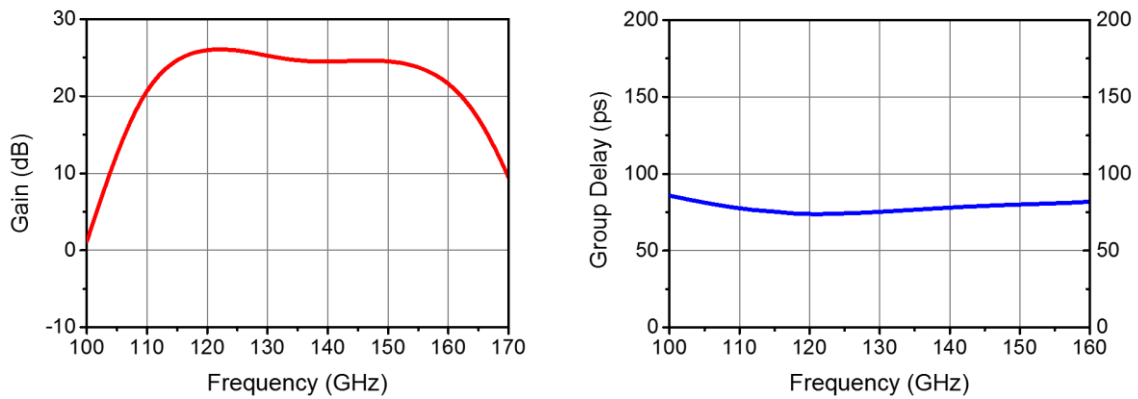
Figure 3.18   Simulated gain and group delay

3.5.3   315 GHz Transmitter Front-end Design

The 315 GHz radio frequency front-end consists of an up-converting mixer and output balun. Its circuit diagram is shown in Figure 3.19. The mixer uses a double-balanced Gilbert cell. A modulated MSK signal centered around 135 GHz is fed a Gilbert cell as IF input. The LO of the mixer is at 180 GHz and the final RF output is centered at 315 GHz. The output of double balanced Gilbert cell is differential which needs to be converted to single-ended for probe measurements. A Marchand balun [63] [64] is used in this design to perform differential to single-ended conversion at the output. To realize the desired coupling ratio, the Marchand balun utilizes broadside coupling using metal 10 (ME10) and aluminum (AL) layers. In this configuration, the coupling factor k can be as high as 0.7 for an excellent phase balance and low insertion loss. The differential port of the balun is connected to the output of Gilbert cell mixer. It is required that the differential conductors of Marchand balun must be "shorted" at the other end. Therefore, DC wise, the Gilbert cell is zero biased at the drain nodes and the mixer becomes a "passive" mixer. Different from a biased active mixer, the passive mixer has no DC current flow in the transistors. The transistors operate in the deep triode region which means there is no reverse isolation from the input to the output of the mixer. This establishes a direct leakage path from IF (135 GHz) to RF (315 GHz). However, even in the case when the transistor is in saturation, reverse isolation is poor since the operating frequency is high. The parasitic drain-to-source capacitances again establish a leakage path from IF to RF. The poor isolation of high-frequency double balance up-conversion mixers further necessitates the output Marchand balun be properly designed to maximize the rejection of this leakage path. The benefits of the full passivity of the up-conversion mixer are low flicker noise

and a high input power compression point. The latter is particularly important as the transmitter output power in this architecture is limited by mixer compression point and mixer conversion gain.

In the simulation, it is found that biasing the drain do help transistor switching slightly. For example, with a 1.0-Volt bias voltage at the drain, the required LO power drops about 2 dB, but there's no difference in conversion performance when mixer enters saturation region. To bias the mixer, instead of grounding at the end of differential conductors, one must use large capacitances to create "AC" short/ground. However, the capacitance not only lowers the overall quality factor
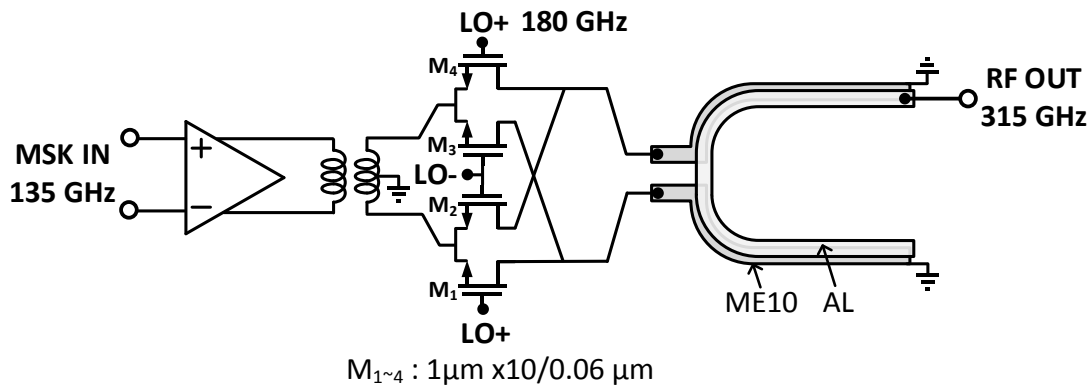
Figure 3.19   Transmitter front-end circuit diagram.
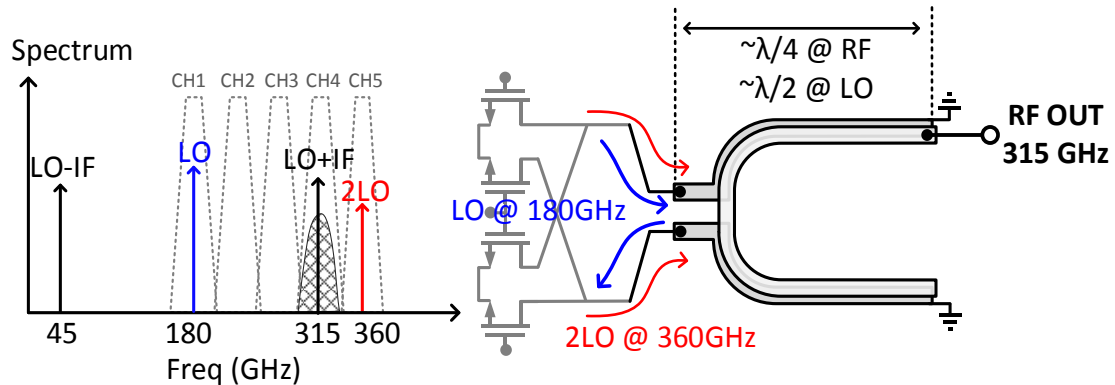
Figure 3.20   Frequency spurs and leaked spectrum rejection.

of Marchand balun matching network but also it creates uncertainties once its operating frequencies to pushed close to its self-resonance. To support multi-channel operation, the transmitter front-end must make sure its output spectrum is confined within allotted bandwidth and it should not produce frequency spurs or harmonics of up-converted spectrums at other frequency bands. As shown in Figure 3.20, in this design, feedthrough of LO at 180 GHz and the 2nd harmonics of LO (2LO) at 360 GHz is identified as a major problem. Because for the former frequency, it falls in CH1 and the latter falls CH5. These signals must be rejected. Fortunately, the combination of double balanced Gilbert cell mixer and Marchand balun exactly serves this purpose. Firstly, the Marchand balun is designed to be $\lambda/4$ at around 315 GHz and at the LO fundamental frequency of 180GHz, it becomes close to $\lambda/8$. Therefore, the overall impedance at the differential input of Marchand balun is extremely small, resulting LO fundamental frequency cancellation. Secondly, the second harmonic of LO frequency together with its own up-converted spectrum is
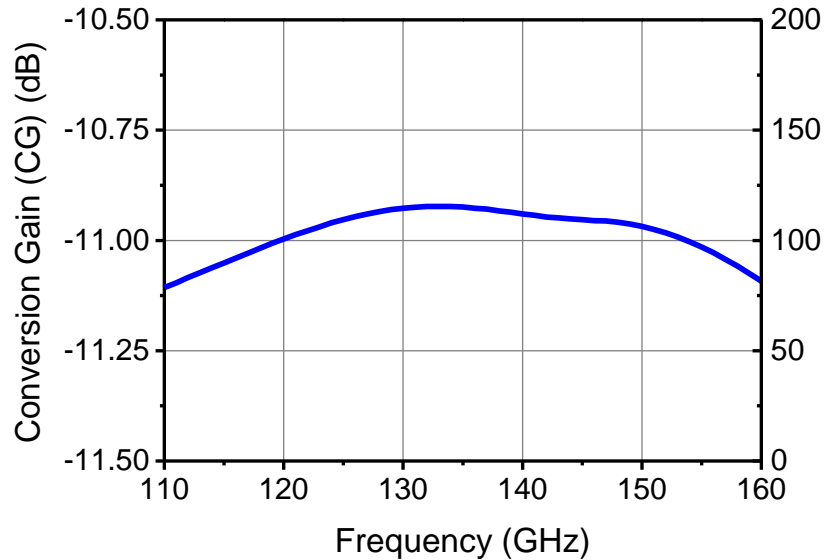
Figure 3.21   Conversion gain of 315-GHz mixer with a Marchand balun

in common mode, Marchand balun cannot support common mode at the differential port, therefore, no output shows up at the single-ended output of the Marchand balun. The simulated conversion loss of 315 GHz mixer with the Marchand balun is shown in Figure 3.21. The mixer is driven to saturation by 0-dBm LO power.

3.5.4 Quadrature Oscillator

An on-chip quadrature oscillator (QVCO) (designed and implemented by Zhiyu Chen) provides quadrature of the first carrier signals to this vector modulator. The quality of the quadrature signal generated by QVCO greatly affects the transmitter performance especially the error-vector-magnitude(EVM) which is defined as the average amplitude of the error vector normalized to the ideal signal peak amplitude,

$$EVM(dB) = 10\log_{10}(\frac{V_{error}}{V_{signal}}) \tag{3.15}$$
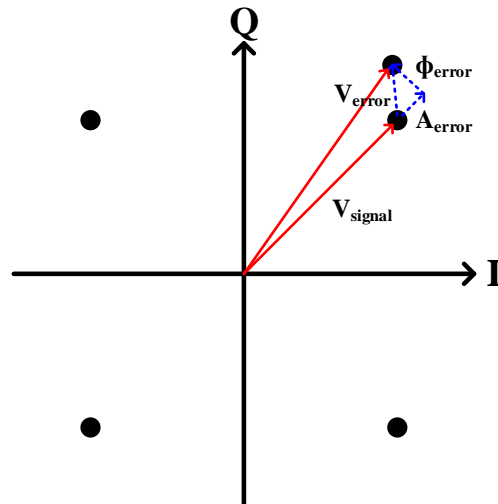
Figure 3.22   EVM constellation conceptual diagram

The error vector can be further decomposed into amplitude error (A_{error}) and phase error (φ_{error}) as shown in Figure 3.22. The quadrature oscillator is the major contributor to the phase error. As the quadrature mismatch of QVCO becomes larger, the averaged constellation points will continuously drift away from the ideal point. The shift reduces the distances between adjacent constellation points and increases the overall bit error rate during data transmission. Although QPSK constellation points are not as tightly spaced as high-level complex modulation such as 128 quadrature amplitude modulation (128-QAM), the quadrature phase mismatch still introduces significant errors since at high frequencies, the low output power of transmitter (small V_{signal} value) and the high noise figure of receiver reduce the signal-to-noise ratio margin of the link. The quadrature mismatch of QVCO must be carefully examined and calibrated. A circuit diagram of QVCO is shown in Figure 3.23. Transistors M_{1-2} and M_{3-4} form two cross-coupled pairs for I and Q tanks. Instead of regular quadrature coupling at the tank, in this design, the quadrature coupling is implemented at the sources of the oscillation transistors by M_{5-8}. The source coupling of the quadrature oscillator brings at least two benefits. First, it minimizes the parasitic loads to the tank [65] because no extra injection coupling transistors are added to the tank side. Moreover, this minimizes the periodical tank loading effect when one of the transistors in the main tank is pushed into the triode region because the source coupling transistors M_{5-8} provide a relatively high impedance path to ground when one of the main tank transistors enters triode region. At the same nodes, injection locking quadrature signals are applied through transistors M_{9-12}. The quadrature injection signals are generated using an on-chip quadrature branch-line coupler and a tripler (quadrature branch-line coupler and tripler are designed and implemented by Wooyeol Choi). The branch-line coupler is made from four sections of quarter-lambda differential transmission lines

which converts two phases differential input signal (0 and 180 degree) from the tripler to four phases of quadrature signal at the output (0, 90, 180, 270 degree).

The quadrature phase relationship of the QVCO is therefore ensured by both quadrature coupling and injection locking. QVCO output frequency is set to be 135 GHz and therefore the
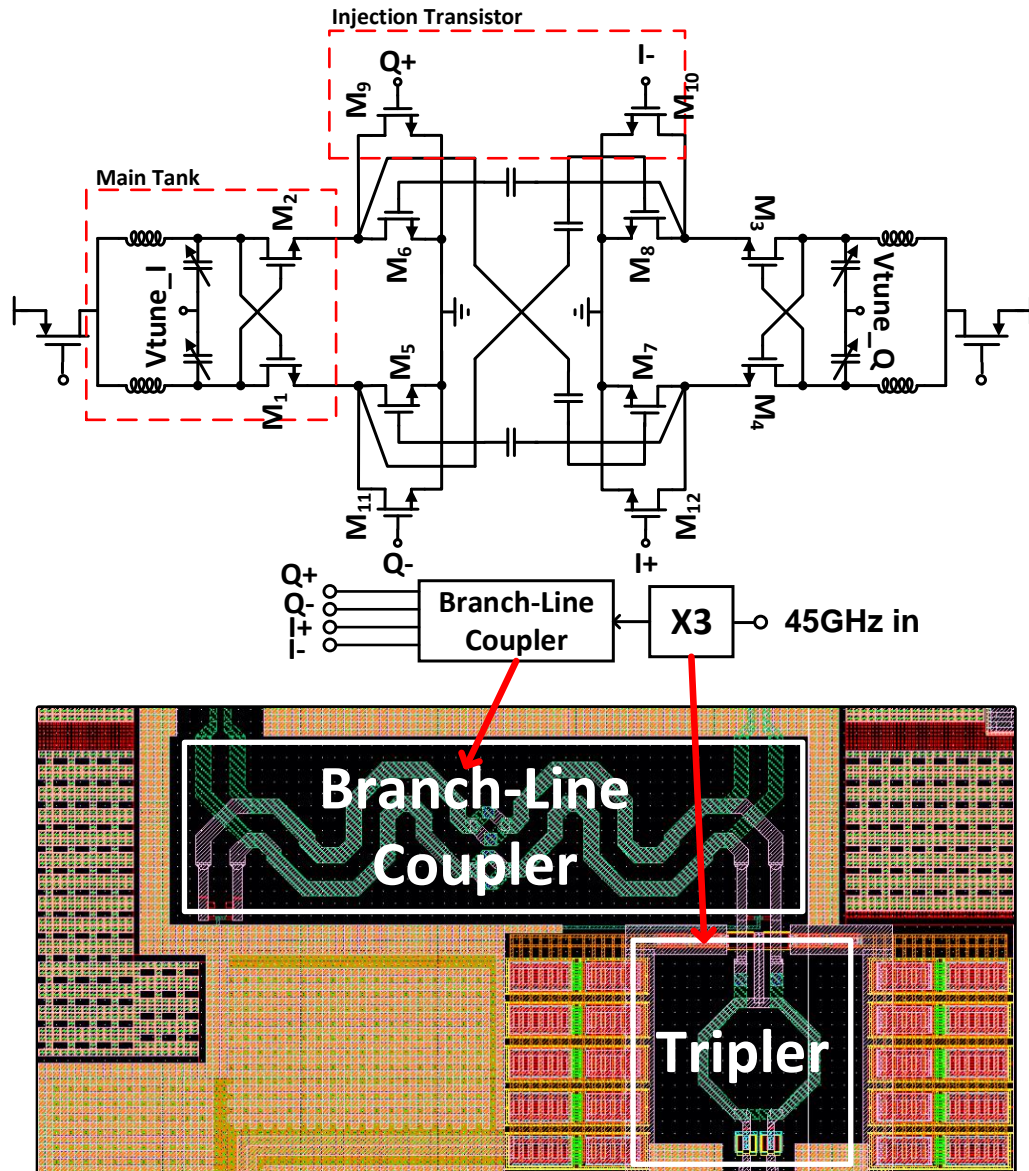
Figure 3.23   QVCO circuit diagram and layout of its branch line coupler and tripler.

injection locking signal can be easily derived from a 45 GHz PLL. The tuning nodes of I and Q

tank varactors are routed out and the tuning voltage of two tanks can be independently set. In

normal operation, the tuning voltage of two tanks should be set to be the same to make sure the

two tanks are resonating at the same frequency. However, this gives a relative phase tuning

capability between the two tanks. The implementation and application of this relative phase tuning

function will be described in detail in the next chapter. The tuning range requirement of QVCO is

low as the first carrier operates only at 135 GHz, which greatly relaxes the design. The output

power of QVCO is set to be 0 dBm when paired with a multi-stage on-chip buffer.

3.6 Transmitter System Simulation

In Figure 3.24, a complete MSK transmitter circuit diagram is shown to reduce simulation

time, the transmitter is simulated using Envelop simulation in Keysight Advanced Design System

Figure 3.24   Complete circuit diagram of MSK transmitter.
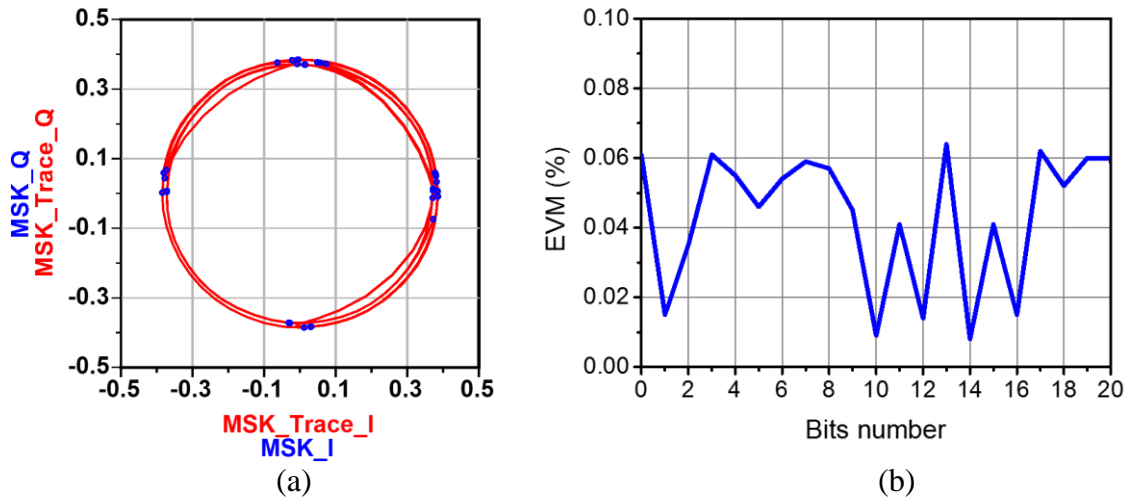
Figure 3.25   (a) MSK constellation (b) EVM over bit sequence.

(ADS). The MSK LO part is excluded from the simulation and the corresponding QVCO is modeled as ideal quadrature signal generators with a 5 degree manually added quadrature phase mismatch. All other parts use transistors models and interconnect parasitics simulated by Ansoft HFSS. The constellation is constructed by comparing the transmitter output to a reference transmitter which is built using all ideal components. Simulated constellations are shown in Figure 3.25(a). The blue dots are I-Q location of bits and their circular traces are shown in red. The error vector magnitude (EVM) performance is shown in Figure 3.25(b). The EVM is less than 10% over the entire bits stream. The simulation is resource demanding. To reduce simulation time and simulation memory requirement, transistor level noise simulation is not performed and therefore, the simulated EVM is mainly a measure of deterministic jitters. 256 random bits with PRBS-7 is simulated while the first 20 bits are shown in the above figure.

The generated signal waveforms of critical signal nodes are shown in Figure 3.26. At the modulator, a sine-shaped baseband signal is first generated, the sinewave overall shape is well

maintained while the maximum and minimum values of some bits are distorted which is mainly due to the frequency response of modulator and the mismatch inside the modulator and at the modulator-data buffer interface. The constellation diagram at RF needs manually sampled with a fixed sampling clock set by the bit period. Finally, an ideal receiver or demodulator is connected to the RF port to examine the demodulated waveform. The ideal received waveform is constructed in ADS using waveform equations. To verify MSK modulation, in this work, the receiver is implemented as a phase/frequency discriminator governed by the equation below

$$\text{DATA}_{\text{demodulated}} = \frac{d\varphi(\text{down-converted sine shaped baseband signal})}{dt} \tag{3.16}$$
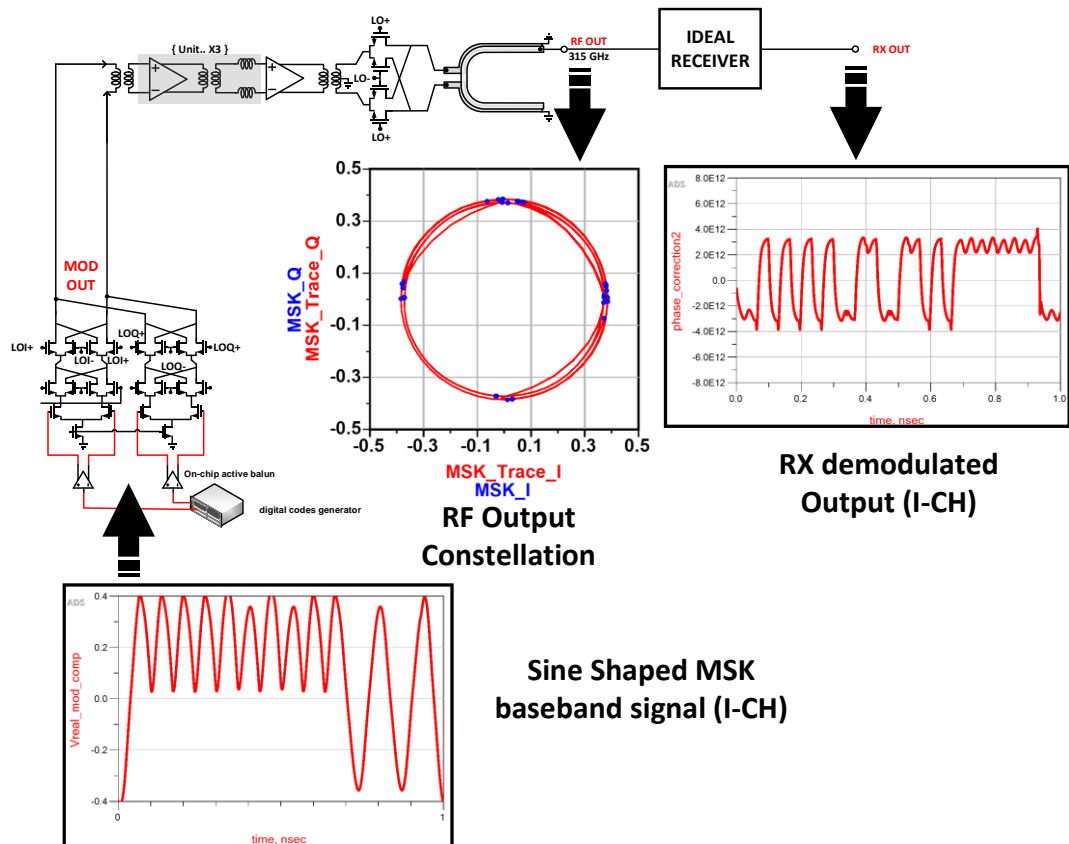
Figure 3.26   Simulated signal waveform of critical nodes along the transmitter chain

3.7 Transmitter Measurement

3.7.1 Quadrature Phase Calibration of QVCO

As mentioned in section 3.5, the quadrature phases of QVCO are critical for the EVM performance of the transmitter. Although it is ensured by both the quadrature coupling of two VCOs themselves and the quadrature injection locking from the branch-line coupler, there're unavoidably some mismatches from either the imbalances of the QVCO or the phase mismatch of the branch-line coupler. The phase mismatches become much worse if the QVCO is not working at the designed frequency (e.g. 10 GHz away from 135 GHz) because the branch-line coupler does not have the similar frequency shift mechanism as the oscillator. The phase shifts of branch line coupler mainly depend on the transmission line electrical length while that of the latter is mainly determined by the tank inductor/varactor and injection locking transistor size/current. When the oscillator is not operating at the designed frequencies, the quadrature branch-line coupler increases the overall quadrature phase mismatch. Fortunately, by working along-side with the on-chip MSK modulator, the quadrature phase mismatch in this design can be calibrated out. The calibration procedure and associated diagram are shown in Figure 3.27. The procedure starts with phase tuning implemented by applying slight DC offset to the frequency tuning element (e.g. I-tank and Q-tank varactors) of quadrature tanks of the QVCO. The applied DC offset voltage introduces an additional phase shift between the two tanks with the assumption that the applied DC offset is small enough that the two tanks are still tightly coupled and resonate at the same frequency. Next, instead of sending baseband digital codes to modulator, a DC level is applied at the data input. Now the bottom two stages of the modulator only control the polarity of upper-most Gilbert-cell
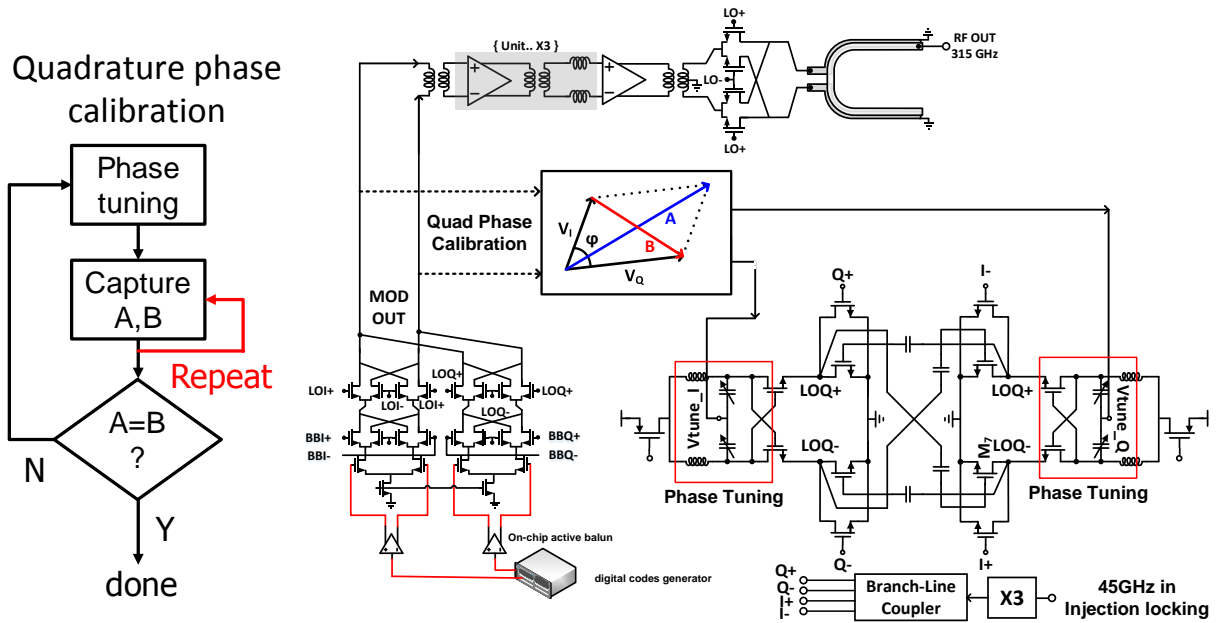
Figure 3.27   QVCO quadrature phase calibration

transistors. In this mode, the entire MSK transmitter degenerates into a two-step heterodyne

continuous wave single frequency up-converter. The output power of this up-converter can be

monitored using an external instrument. At different combinations of bottom switch settings of the

modulator, the amplitude of vector summation (A) and vector subtraction (B) can be obtained.

From Figure 3.7, it is shown that A=B only when the QVCO is in quadrature. Therefore, A=B is

used as an indicator for the quadrature status of QVCO. In the next step, these steps are repeated

multiple times at all the switch combinations of the modulator to avoid additional phase mismatch

introduced by modulator itself. Finally, the average value of A and B in all kinds of modulator

switches combinations are calculated and compared. If A=B, the QVCO is in true quadrature, and

the calibration is done. Phase calibration plane is right at the I and Q path LO port) of MSK modulator.

3.7.2 External Receiver with Image Rejection

The receiver for analyzing the transmitter output is built with external components. To simplify the measurement and to get most of the bandwidth of our baseband amplifier and sampling oscilloscope, a zero-IF architecture is chosen for the external receiver. Generally, a direct-conversion receiver suffers from an image problem if the modulated spectrum is not symmetric and the image is the signal itself. For phase modulation like QPSK and MSK, there is no guarantee that the signal spectrum is fully symmetric. Therefore, image rejection is necessary. With image signal in the pass band, image rejection relying on RF filtering does not work. The receiver must be built to have image rejection at the baseband. A typical direct-conversion receiver with image rejection is shown in the upper part of Figure 3.28. This architecture poses several challenges for implemented using lab equipment. First, the required quadrature LO generation at 300 GHz is very difficult. Second, the IF is wideband with a rate of 15-Gbps. A simple poly phase filter (PPF) does not support this wide bandwidth. A way to avoid this is to implement the other half of image rejection circuits in digital domain which needs dual channel high-speed analog to digital converters (ADCs) and high-speed digital signal processor (DSP) both of which are expensive. Fortunately, there is another way to solve the image rejection problem. As shown in the bottom part of Figure 3.28, instead of quadrature mixing, a single channel mixer is used. Two vector signal generators (PSG) are used here. One provides an LO for the external mixer and another one provides LO for TX. The two PSGs are phase locked. Phase locking two PSGs enables the manual I-Q channel selection because the relative phase can be always manually tuned to be

exactly 90 degrees or 0 degree to select the I or Q channel. Mathematically, the channel selection

process is shown in Eqn. (3.17). Using this method for channel selection does not need any extra

instruments or modifications to the existing measurement equipment. The PSG phase locking

through the 10-MHz sync port is a built-in function for every Keysight vector signal generators.

$$(A_I(t)\cos(\omega_{LO}t) + A_Q(t)\sin(\omega_{LO}t))\cos(\omega_{LO}t + \Phi_1) = \begin{cases} A_I(t) & \Phi_1 = 0 \\ A_Q(t) & \Phi_1 = 90 \end{cases} \tag{3.17}$$

Although its simplicity and low cost, this method has a significant drawback that the phases

of the signal generators of OSC INJ, LO and down-conversion mixer LO need to be stably locked
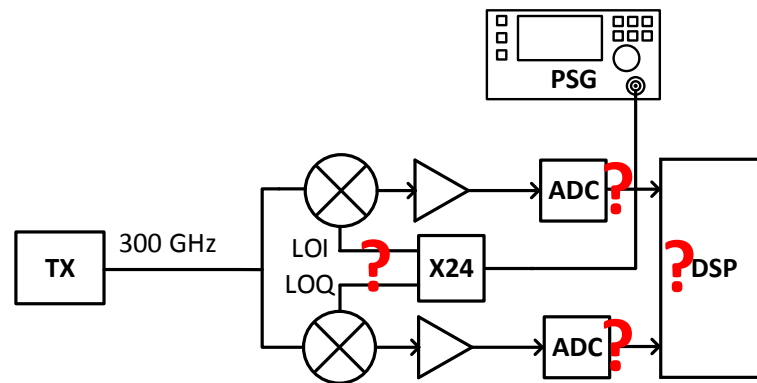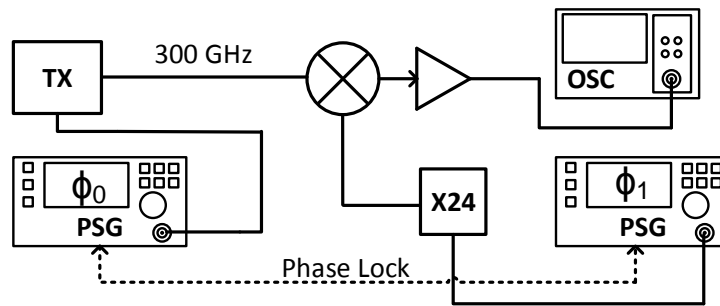
Figure 3.28   Two different architecture for direct conversion receiver

101

without any drift over time during the measurement. Keysight provides high accuracy oven-backed extremely low phase noise 10-MHz reference to be used for phase locking. However, frequency multiplication ratio is still too high in this system compared to normal communication systems. On the transmitter side, the signal needs to be multiplied all the way from 10-MHz reference frequency to 300GHz and the same thing also needs to happen on the receiver side.

This ultra-high multiplication factor contributes to the high accumulated phase noise of the TRX chain. Although the RF signal is demodulated coherently at the receiver side, the relative phase slowly drifts from one value to another over time. In real measurements, the phase locking slowly drifts away at a slow speed and significant variations close to DC can be observed both on a spectrum analyzer and a sampling oscilloscope. This significantly limits the time window to conduct the transmitter measurement. This is one of the major contributors to the high amplitude noise in the eye diagram.

3.7.3   Transmitter Measurement Setup

The measurement setup using probes is shown in Figure 3.29. The setup is based on the direct conversion receiver with image rejection shown in Figure 3.28(bottom). The RF output of the transmitter is down-converted to baseband using an external 2nd order harmonic mixer. The double side-band (DSB) conversion loss of the 2nd order harmonic mixer is 6.5dB and DSB noise figure of 2nd order harmonic mixer is also 6.5 dB. The mixer supports an IF bandwidth from DC to 38 GHz which is sufficient for measurements up to the 15 Gbps data rate. A cascade of an amplifier and a multiplier (AMC Chain) is used to provide the signal at ~150 GHz for LO for the 2nd order harmonic mixer. The AMC power must be attenuated down to 2-3 dBm range in order to protect the harmonic mixer LO port. The down-converted baseband signal is amplified by a
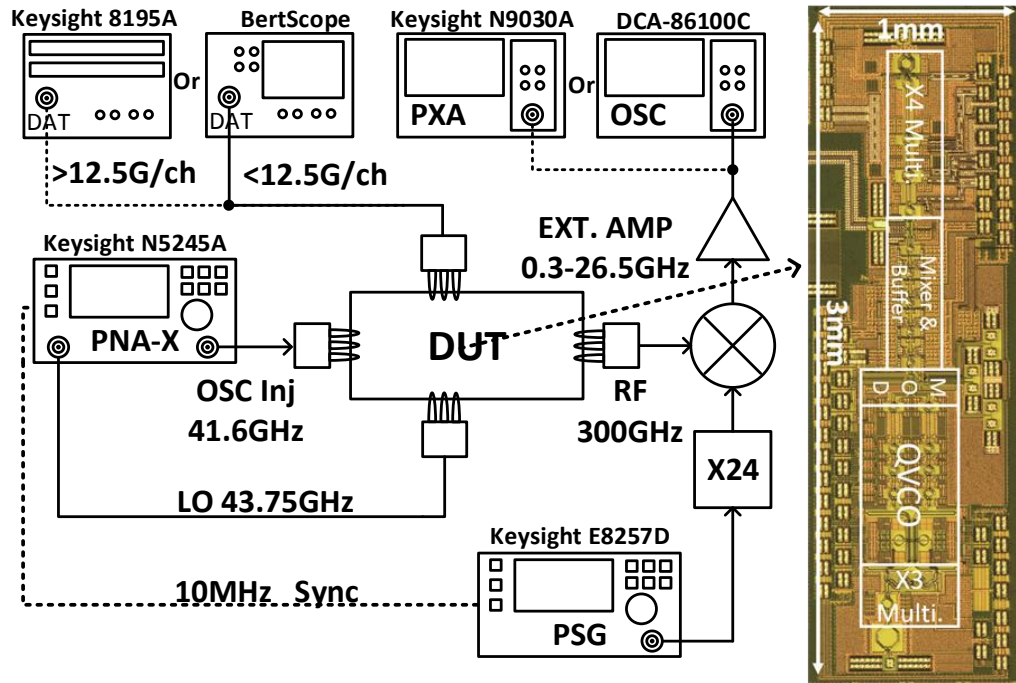
Figure 3.29   Transmitter measurement diagram and die photo.

broadband 0.1 GHz to 22 GHz preamp with a gain of 23 dB and fed to a spectrum analyzer or to a sampling oscilloscope. No equalization is applied to correct the gain ripple of amplifier and conversion gain variation over the frequency of 2nd order harmonic mixer. A die photograph of the transmitter is also shown in Figure 3.29. The chip measures 1mm by 3mm including all the DC and RF bond pads. It is difficult for the instrument to demodulate the MSK signal at such high data rate because MSK signal generation requires quadrature clocks which are sine waves at a frequency equal to a half of the single channel bit rate. The quadrature clocks also need to be time aligned with the incoming bits which require a high-speed CDR and a delay locked loop (DLL). Due to the limitation, the transmitter measurement is performed using QPSK modulation. In this
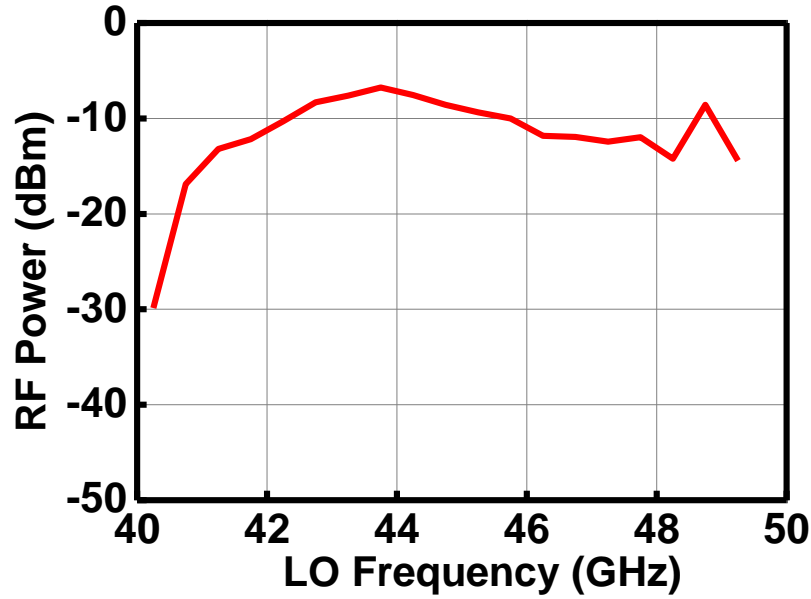
Figure 3.30   Measured RF output power versus LO frequency at QVCO frequency of 125 GHz

case, a DC level is applied to the modulator shaping stage and the shaping stages work as a pair of always-on-switches.

The measured QVCO frequency is downshifted from 135 GHz to 125 GHz. The reason for this downshift is mainly due to the improper estimation of the capacitance of varactors and missing of interconnect parasitic in post-simulation. To adapt to the new oscillator frequency, 41.6-GHz instead of 45 GHz is chosen as the QVCO injection lock signal (OSC Inj in Figure 3.29) frequency. The LO input (LO in Figure 3.29) to the on-chip 2-stage doubler is provided by another PSG and its frequency is swept from 40-50 GHz to determine the maximum transmitter output power and the results are shown in Figure 3.30. At 43.75 GHz or RF of 300 GHz, the peak RF output power

of -6dBm required by the system is achieved. In order to maximize the transmitter system performance, the RF frequency is thus chosen to be 300 GHz instead of 315 GHz.

Sample QPSK spectra of 25-Gbps PRBS-31 input and 30-Gbps PRBS-7 are shown in Figure 3.31. The overall shape of the spectra is well matched to that of a QPSK spectrum. A spur at ~12 GHz is due to the signal used to generate the LO for the external down conversion mixer in the measurement setup. In Figure 3.32, eye diagrams of I channel at the input data rate of 10Gb/s, 16Gb/s, 25 Gb/s and 30 Gb/s are shown. Limited by the instrumentation, only one channel (I or Q) is captured at a time. The eye diagrams for both I and Q channels are the same. The eyes remain open wide without any significant distortion, suggesting that the circuit can support an even higher data rate. As shown in Table 3-4, the transmitter provides the highest data rate among all the CMOS transmitter with an on-chip modulator. It is also the QPSK transmitter with the highest data rate among all fabricated in silicon including MOS transistors and SiGe HBT's. The energy efficiency
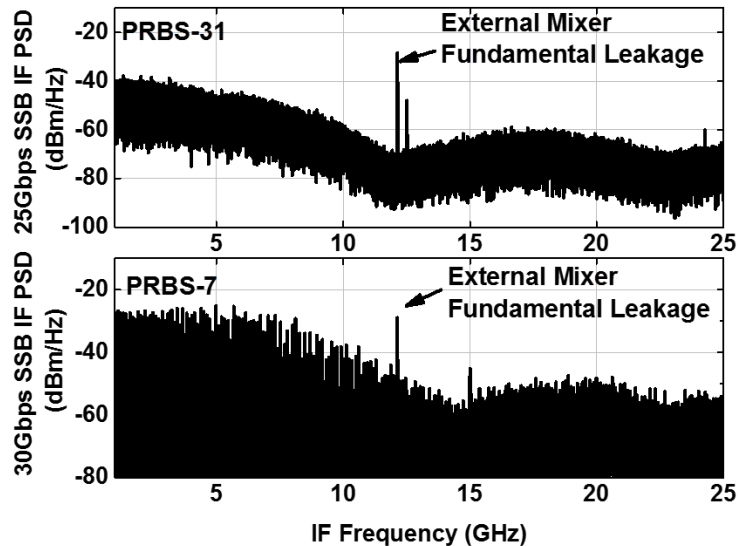
Figure 3.31   Single side band (SSB) spectra for 25-Gbps (PRBS-31, BSA125C) and 30-Gbps

of 6pJ/bit for the transmitter is ~2X better than that of the 16-Gbps CMOS QPSK transmitter [45]

and that of the 32-QAM CMOS transmitter not including a modulator [49].
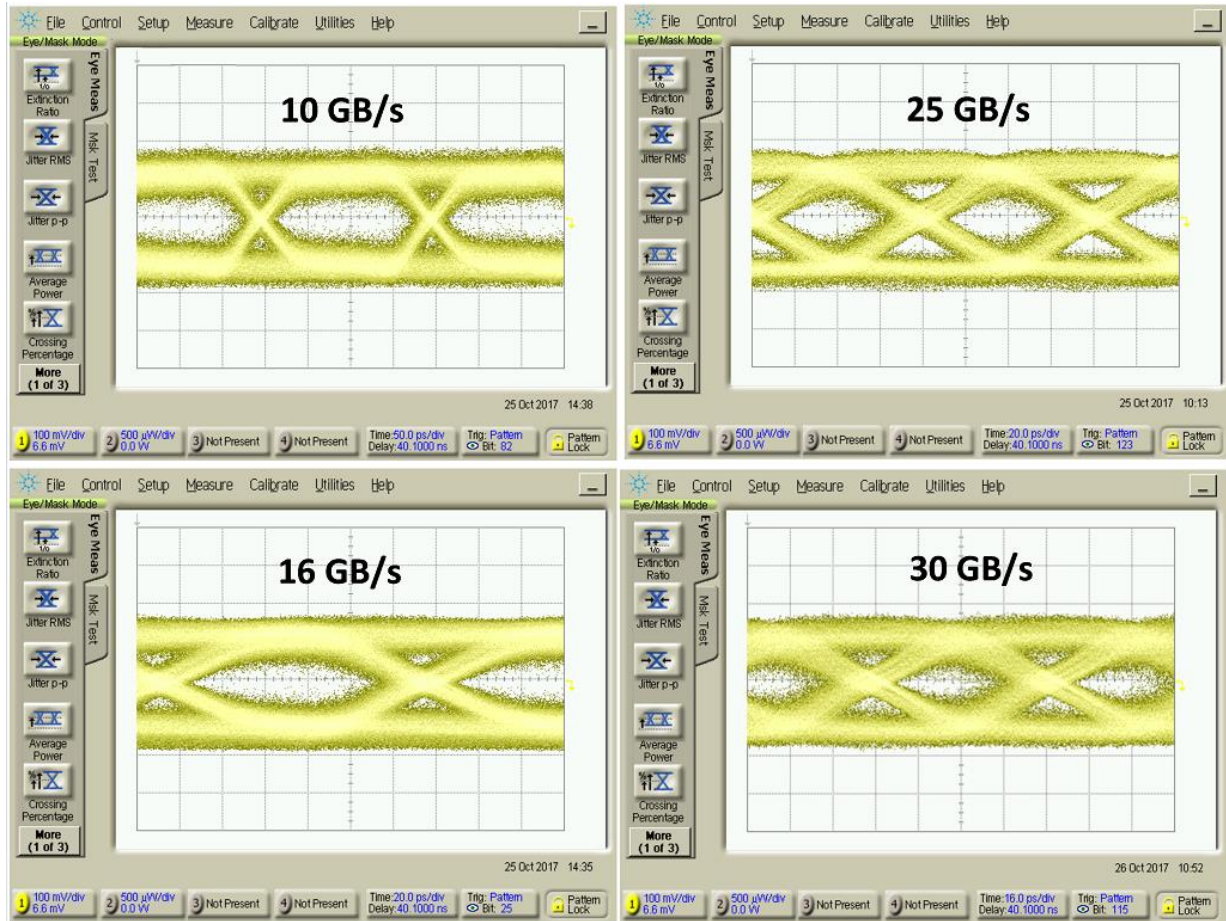
Figure 3.32   Eye diagram at data rate of 10GB/s, 25GB/s, 16GB/s and 25 GB/s

Table 3-4   Comparison of transmitter performance

	[66]	[67]	[45]	[68]	[8]	[49]	[48]	**This Work**
f_c (GHz)	190	240	240	110-170	300	300	300	**300**
P_{out} (dBm)	-6	-4.4	0	9	-	-5.5	-14.5	**-6**
BW_{RF} (GHz)	40	17	14	50	30	-	-	**40**
Integration Level	FE[2]	MOD[3] FE[2]	Full	MOD[3] FE[2]	MOD[3]	FE[2]	FE[2]	**FE[2] MOD[3]**
Modulation	BPSK	QPSK	QPSK	QPSK	QPSK	32 QAM	16 QAM	**QPSK**
Data Rate (Gbps)	50	23.2[7]	16	48	50	107[5]	28[5]	**30[4]**
Technology	130nm SiGe	130nm SiGe	65nm CMOS	250nm InP	250nm InP	40nm CMOS	40nm CMOS	**65nm CMOS**
P_{DC} (mW)	32	1033	180	165	-	1400	1400	**180**
Energy/Bit (pJ/bit)	-	-	11.3	3.4	-	13.1[6]	-	**6**
Note	[1]on chip antenna, [2]RF front-end, [3] modulator and associated baseband circuits, [4] limited by instrument, [5]with equalization, [6]modulator not included. [7]estimated							

CHAPTER 4

SUMMARY AND FUTURE WORK

4.1 Summary

A 225-280 GHz receiver for rotational spectroscopy fabricated in 65-nm CMOS is demonstrated. The receiver was used in a rotational spectrometer to detect gas molecules in a mixture, demonstrating for the first time that a CMOS receiver can be used for rotational spectroscopy. Furthermore, this work also demonstrated that a CMOS circuit operating at 225 to 280 GHz can support an existing application. This is an important step toward realizing an affordable rotational spectrometer.

A 300-GHz 30-Gbps QPSK transmitter intended for FDM and PDM 300-Gbps dielectric waveguide communication with an output power of -6 dBm is demonstrated in 65-nm CMOS. The transmitter shows the highest data bandwidth among the state-of-arts high-frequency transmitters including an on-chip modulator. The 315-GHz transmitter front-end utilizes a combination of Marchand balun and double balanced mixer to achieve the high rejection of unwanted out of band harmonic tones and the up-converted input signal. The wide bandwidth data buffer uses innovative coupled resonator inter-stage matching together with conventional transformer matching to achieve nearly constant group delay and in-band gain.

4.2 Future Work

4.2.1   Future Work for Receiver of Rotational Spectrometer

One of the factors limiting the performance of rotational spectroscopy is the performance of amplitude detector. The noise of the detector has been analyzed in detail in Chapter 2. In spectroscopy applications, the amplitude of received signal in typical operations could be very large compared to the one in AM communication systems. However, the absolute signal amplitude is not the one of interest for AM receivers. The change of the signal amplitude is of interest for spectroscopy. The large signal amplitude actually degrades the peak sensitivity because of resulting deviation of the bias from the optimum and generation of additional noise. These two factors put a cap on the maximum signal amplitude at the input of the detector and this limits the optimization space for further SNR improvement. In Figure 4.1, the output noise, NEP, and responsivity versus input amplitude of detector used in rotational spectroscopy receiver is shown. The responsivity drops with an increase of input signal amplitude. This result is discouraging as it turns out that the improvement to the overall system sensitivity by improving transmitter output power or conversion gain of the receiver is limited. Sometimes increasing the transmitted power or conversion gain of the receiver may even make the system performance worse.

The origin of all these issues is at the amplitude detector. If amplitude detection can be done linearly without using non-linear building blocks, the system performance can be further improved using the high dynamic range techniques available for linear systems.
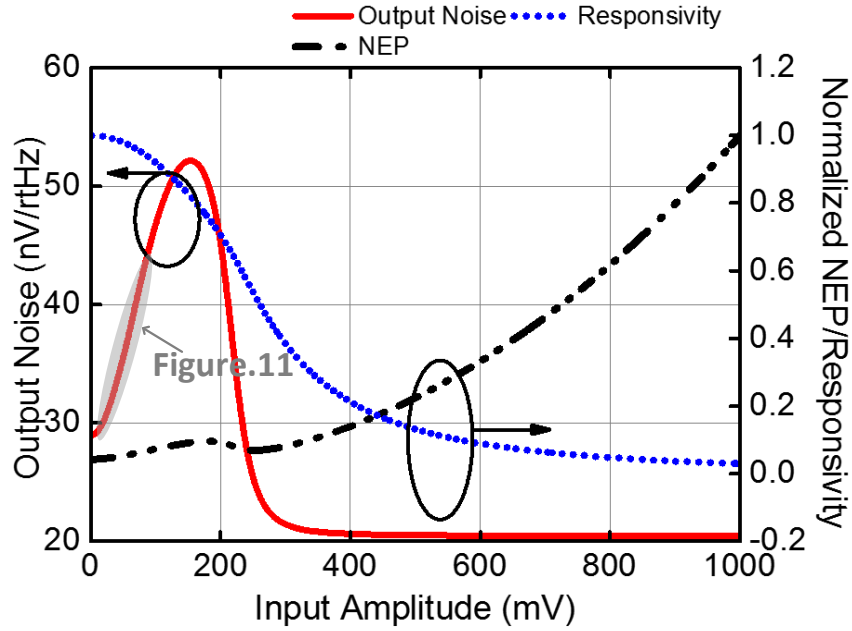
Figure 4.1   Output noise, normalized NEP, Responsivity versus input amplitude.

4.2.2   Future Work for Transmitter of Dielectric Waveguide Communication Systems

A transmitter for a single channel of dielectric communication system has been successfully demonstrated. The 30-Gbps data transmission using a 300-GHz carrier has been proven to be feasible. The next step is incorporation of the 300-Gbps transmitter into the system. The first challenge is the interface. The transmitter needs to be interfaced with a dielectric waveguide instead of a probe. An on-chip antenna is a good element for interfacing the chip to a dielectric waveguide as no physical connections from the chip to a dielectric waveguide is needed. This greatly simplifies the interface. Various antenna structures need to be investigated and the tradeoffs between the radiation efficiency and bandwidth should be understood. The large bandwidth requirement will make designing a high-efficiency antenna difficult at these frequencies. The concept of polarization division multiplexing using a pair of antennas aligned in orthogonal

directions also needs further investigation as the level of isolation between the on-chip antennas may not be sufficiently high for adequate suppression of channel crosstalk. Lastly, the dielectric waveguide will be physically close to antennas and this will modify the antenna performances. The radiation efficiency and bandwidth of the antenna need to be carefully modeled and simulated in the presence of this large dielectric slab.

On the circuit level, multiple improvements need to be made. First, the QVCO frequency needs to be tuned back to 135 GHz. The QVCO frequency downshift is mainly due to improper modeling of varactor cells and addition of antenna diodes to the main tank. An on-chip PRBS and a quadrature data clock generation circuit should be included in the next chip. Providing a high-speed data input from off-chip has proven to be difficult as the cables need to phase matched. Probes, connectors, and long cables increase the uncertainty during high-speed baseband data transmission. An on-chip PRBS generator minimizes the interconnection distance, the baseband data stream need to travel to reach the modulator for improved fidelity. Another benefit of the on-chip PRBS generator is that the bandwidth limitation is greatly relaxed for the on-chip implementation compared to using off-chip components. It is easy to generate a high data rate bit stream on-chip while costly instruments are needed for the off-chip approach. It is also easier to derive data clocks from the on-chip PRBS generator as the generation process itself is based on clocked multiplexing.

REFERENCES

[1]   M. M. Rodgers, V. M. Pai, and R. S. Conroy, "Recent Advances in Wearable Sensors for Health Monitoring," *IEEE Sens. J.*, vol. 15, no. 6, pp. 3119–3126, Jun. 2015.

[2]   K.-H. Kim, S. A. Jahan, and E. Kabir, "A review of breath analysis for diagnosis of human health," *TrAC Trends Anal. Chem.*, vol. 33, pp. 1–8, Mar. 2012.

[3]   I. R. Medvedev, C. F. Neese, G. M. Plummer, and F. C. D. Lucia, "Submillimeter spectroscopy for chemical analysis with absolute specificity," *Opt. Lett.*, vol. 35, no. 10, pp. 1533–1535, May 2010.

[4]   K.-H. Kim, S. A. Jahan, and E. Kabir, "A review of breath analysis for diagnosis of human health," *TrAC Trends Anal. Chem.*, vol. 33, pp. 1–8, Mar. 2012.

[5]   "260h / Vibrational and Rotational Spectroscopy." [Online]. Available: https://260h.pbworks.com/w/page/58803638/Vibrational%20and%20Rotational%20Spectroscopy. [Accessed: 22-Feb-2017].

[6]   J. Manyika, M. Chui, J. Bughin, R. Dobbs, P. Bisson, and A. Marrs, "Disruptive technologies: Advances that will transform life, business, and the global economy | McKinsey & Company." [Online]. Available: http://www.mckinsey.com/business-functions/digital-mckinsey/our-insights/disruptive-technologies. [Accessed: 21-Feb-2017].

[7]   C. W. Byeon, C. H. Yoon, and C. S. Park, "A 67-mW 10.7-Gb/s 60-GHz OOK CMOS Transceiver for Short-Range Wireless Communications," *IEEE Trans. Microw. Theory Tech.*, vol. 61, no. 9, pp. 3391–3401, Sep. 2013.

[8]   H. J. Song, J. Y. Kim, K. Ajito, N. Kukutsu, and M. Yaita, "50-Gb/s Direct Conversion QPSK Modulator and Demodulator MMICs for Terahertz Communications at 300 GHz," *IEEE Trans. Microw. Theory Tech.*, vol. 62, no. 3, pp. 600–609, Mar. 2014.

[9]   K. Katayama *et al.*, "A 300 GHz CMOS Transmitter With 32-QAM 17.5 Gb/s/ch Capability Over Six Channels," *IEEE J. Solid-State Circuits*, vol. 51, no. 12, pp. 3037–3048, Dec. 2016.

[10]   E. a. J. Marcatili, "Dielectric Rectangular Waveguide and Directional Coupler for Integrated Optics," *Bell Syst. Tech. J.*, vol. 48, no. 7, pp. 2071–2102, Sep. 1969.

[11]   "Ultralow loss dielectric ribbon waveguide for millimeter/submillimeter waves," *Appl. Phys. Lett.*, vol. 54, no. 12, pp. 1183–1185, Mar. 1989.

[12]   C. Yeh, F. Shimabukuro, and P. H. Siegel, "Low-loss terahertz ribbon waveguides," *Appl. Opt.*, vol. 44, no. 28, pp. 5937–5946, Oct. 2005.

[13] S. Fukuda *et al.*, "A 12.5+12.5 Gb/s Full-Duplex Plastic Waveguide Interconnect," *IEEE J. Solid-State Circuits*, vol. 46, no. 12, pp. 3113–3125, Dec. 2011.

[14] Y. Kim, L. Nan, J. Cong, and M. C. F. Chang, "High-Speed mm-Wave Data-Link Based on Hollow Plastic Cable and CMOS Transceiver," *IEEE Microw. Wirel. Compon. Lett.*, vol. 23, no. 12, pp. 674–676, Dec. 2013.

[15] W. Volkaerts, N. V. Thienen, and P. Reynaert, "10.2 An FSK plastic waveguide communication link in 40nm CMOS," in *2015 IEEE International Solid-State Circuits Conference - (ISSCC) Digest of Technical Papers*, 2015, pp. 1–3.

[16] K. Schmalz, Y. Mao, J. Borngraber, P. Neumaier, and H. W. Hubers, "Tunable 245 GHz transmitter and receiver in sige technology for gas spectroscopy," *Electron. Lett.*, vol. 50, no. 12, pp. 881–882, Jun. 2014.

[17] Q. Zhong, W. Choi, C. Miller, R. Henderson, and K. K. O, "25.2 A 210-to-305GHz CMOS receiver for rotational spectroscopy," in *2016 IEEE International Solid-State Circuits Conference (ISSCC)*, 2016, pp. 426–427.

[18] "Limiting Sensitivity of a Microwave Spectrometer," *J. Appl. Phys.*, vol. 19, no. 8, pp. 795–796, Aug. 1948.

[19] K. Schmalz, N. Rothbart, P. F. X. Neumaier, J. Borngräber, H. W. Hübers, and D. Kissinger, "Gas Spectroscopy System for Breath Analysis at mm-wave/THz Using SiGe BiCMOS Circuits," *IEEE Trans. Microw. Theory Tech.*, vol. PP, no. 99, pp. 1–12, 2017.

[20] A. Shamim, L. Roy, N. Fong, and N. G. Tarr, "24 GHz On-Chip Antennas and Balun on Bulk Si for Air Transmission," *IEEE Trans. Antennas Propag.*, vol. 56, no. 2, pp. 303–311, Feb. 2008.

[21] A. Babakhani, X. Guan, A. Komijani, A. Natarajan, and A. Hajimiri, "A 77-GHz Phased-Array Transceiver With On-Chip Antennas in Silicon: Receiver and Antennas," *IEEE J. Solid-State Circuits*, vol. 41, no. 12, pp. 2795–2806, Dec. 2006.

[22] W. Steyaert and P. Reynaert, "A 0.54 THz Signal Generator in 40 nm Bulk CMOS With 22 GHz Tuning Range and Integrated Planar Antenna," *IEEE J. Solid-State Circuits*, vol. 49, no. 7, pp. 1617–1626, Jul. 2014.

[23] Z. Wang, P. Y. Chiang, P. Nazari, C. C. Wang, Z. Chen, and P. Heydari, "A CMOS 210-GHz Fundamental Transceiver With OOK Modulation," *IEEE J. Solid-State Circuits*, vol. 49, no. 3, pp. 564–580, Mar. 2014.

[24] S. Pan, D. Wang, C. Guclu, and F. Capolino, "High impedance layer for CMOS on-chip antenna at millimeter waves," in *2011 IEEE International Symposium on Antennas and Propagation (APSURSI)*, 2011, pp. 903–906.

[25] H. Chu, L. Qingyuan, and Y.-X. Guo, "60-GHz broadband CMOS on-chip antenna with an artificial magnetic conductor," in *2016 IEEE MTT-S International Microwave Workshop Series on Advanced Materials and Processes for RF and THz Applications (IMWS-AMP)*, 2016, pp. 1–2.

[26] M. Cohn, J. E. Degenford, and B. A. Newman, "Harmonic Mixing with an Antiparallel Diode Pair," *IEEE Trans. Microw. Theory Tech.*, vol. 23, no. 8, pp. 667–673, Aug. 1975.

[27] C. H. Lin, Y. A. Lai, J. C. Chiu, and Y. H. Wang, "A 23 to 37 GHz Miniature MMIC Subharmonic Mixer," *IEEE Microw. Wirel. Compon. Lett.*, vol. 17, no. 9, pp. 679–681, Sep. 2007.

[28] C. M. Lin, H. K. Lin, Y. A. Lai, C. P. Chang, and Y. H. Wang, "A 10 to 40 GHz Broadband Subharmonic Monolithic Mixer in 0.18 m CMOS Technology," *IEEE Microw. Wirel. Compon. Lett.*, vol. 19, no. 2, pp. 95–97, Feb. 2009.

[29] D. Shim, S. Sankaran, and K. K. O, "Complementary Antiparallel Schottky Barrier Diode Pair in a 0.13- Logic CMOS Technology," *IEEE Electron Device Lett.*, vol. 29, no. 6, pp. 606–608, Jun. 2008.

[30] C. L. Kuo, C. C. Kuo, C. H. Lien, J. H. Tsai, and H. Wang, "A Novel Reduced-Size Rat-Race Broadside Coupler and Its Application for CMOS Distributed Sub-Harmonic Mixer," *IEEE Microw. Wirel. Compon. Lett.*, vol. 18, no. 3, pp. 194–196, Mar. 2008.

[31] "Wiley: Microwave Engineering, 4th Edition - David M. Pozar." [Online]. Available: http://www.wiley.com/WileyCDA/WileyTitle/productCd-EHEP002016.html. [Accessed: 07-Mar-2017].

[32] "https://www.microwaves101.com/ | Magic Tees." [Online]. Available: https://microwaves101.com/encyclopedias/magic-tees. [Accessed: 18-Jul-2018].

[33] L. Zhou, C. C. Wang, Z. Chen, and P. Heydari, "A W-band CMOS Receiver Chipset for Millimeter-Wave Radiometer Systems," *IEEE J. Solid-State Circuits*, vol. 46, no. 2, pp. 378–391, Feb. 2011.

[34] J. D. Park, S. Kang, S. V. Thyagarajan, E. Alon, and A. M. Niknejad, "A 260 GHz fully integrated CMOS transceiver for wireless chip-to-chip communication," in *2012 Symposium on VLSI Circuits (VLSIC)*, 2012, pp. 48–49.

[35] Y. Shang, H. Yu, C. Yang, Y. Liang, and W. M. Lim, "A 239-281GHz Sub-THz imager with 100MHz resolution by CMOS direct-conversion receiver with on-chip circular-polarized SIW antenna," in *Proceedings of the IEEE 2014 Custom Integrated Circuits Conference*, 2014, pp. 1–4.

[36]   E. Ojefors, B. Heinemann, and U. R. Pfeiffer, "Subharmonic 220- and 320-GHz SiGe HBT Receiver Front-Ends," *IEEE Trans. Microw. Theory Tech.*, vol. 60, no. 5, pp. 1397–1404, May 2012.

[37]   J. Han, Y. Lu, N. Sutardja, and E. Alon, "6.2 A 60Gb/s 288mW NRZ transceiver with adaptive equalization and baud-rate clock and data recovery in 65nm CMOS technology," in *2017 IEEE International Solid-State Circuits Conference (ISSCC)*, 2017, pp. 112–113.

[38]   J. Lee, P. C. Chiang, and C. C. Weng, "56Gb/s PAM4 and NRZ SerDes transceivers in 40nm CMOS," in *2015 Symposium on VLSI Circuits (VLSI Circuits)*, 2015, pp. C118–C119.

[39]   T. Shibasaki *et al.*, "3.5 A 56Gb/s NRZ-electrical 247mW/lane serial-link transceiver in 28nm CMOS," in *2016 IEEE International Solid-State Circuits Conference (ISSCC)*, 2016, pp. 64–65.

[40]   P. Reynaert *et al.*, "Polymer Microwave Fibers: A blend of RF, copper and optical communication," in *ESSCIRC Conference 2016: 42nd European Solid-State Circuits Conference*, 2016, pp. 15–20.

[41]   W. Volkaerts, N. V. Thienen, and P. Reynaert, "10.2 An FSK plastic waveguide communication link in 40nm CMOS," in *2015 IEEE International Solid-State Circuits Conference - (ISSCC) Digest of Technical Papers*, 2015, pp. 1–3.

[42]   Z. Wang, P. Y. Chiang, P. Nazari, C. C. Wang, Z. Chen, and P. Heydari, "A CMOS 210-GHz Fundamental Transceiver With OOK Modulation," *IEEE J. Solid-State Circuits*, vol. 49, no. 3, pp. 564–580, Mar. 2014.

[43]   J. Lee, Y. Chen, and Y. Huang, "A Low-Power Low-Cost Fully-Integrated 60-GHz Transceiver System With OOK Modulation and On-Board Antenna Assembly," *IEEE J. Solid-State Circuits*, vol. 45, no. 2, pp. 264–275, Feb. 2010.

[44]   C. W. Byeon, J. J. Lee, K. C. Eun, and C. S. Park, "A 60 GHz 5 Gb/s Gain-Boosting OOK Demodulator in 0.13 CMOS," *IEEE Microw. Wirel. Compon. Lett.*, vol. 21, no. 2, pp. 101–103, Feb. 2011.

[45]   S. Kang, S. V. Thyagarajan, and A. M. Niknejad, "A 240 GHz Fully Integrated Wideband QPSK Transmitter in 65 nm CMOS," *IEEE J. Solid-State Circuits*, vol. 50, no. 10, pp. 2256–2267, Oct. 2015.

[46]   E. Bloch and E. Socher, "An F-band 20.6Gbp/s QPSK transmitter in 65nm CMOS," in *2014 IEEE Radio Frequency Integrated Circuits Symposium*, 2014, pp. 299–302.

[47]   F. Xiong, *Digital Modulation Techniques*. Artech House, 2000.

[48]	K. Katayama *et al.*, "20.1 A 300GHz 40nm CMOS transmitter with 32-QAM 17.5Gb/s/ch capability over 6 channels," in *2016 IEEE International Solid-State Circuits Conference (ISSCC)*, 2016, pp. 342–343.

[49]	K. Takano *et al.*, "17.9 A 105Gb/s 300GHz CMOS transmitter," in *2017 IEEE International Solid-State Circuits Conference (ISSCC)*, 2017, pp. 308–309.

[50]	P. Heydari and R. Mohanavelu, "Design of ultrahigh-speed low-voltage CMOS CML buffers and latches," *IEEE Trans. Very Large Scale Integr. VLSI Syst.*, vol. 12, no. 10, pp. 1081–1093, Oct. 2004.

[51]	A. Azizzadeh and L. Mohammadi, "Degradation of BER by Group Delay in Digital Phase Modulation," in *2008 Fourth Advanced International Conference on Telecommunications*, 2008, pp. 350–354.

[52]	D. Zhao and P. Reynaert, "An E-Band Power Amplifier With Broadband Parallel-Series Power Combiner in 40-nm CMOS," *IEEE Trans. Microw. Theory Tech.*, vol. 63, no. 2, pp. 683–690, Feb. 2015.

[53]	D. Zhao and P. Reynaert, "A 60-GHz Dual-Mode Class AB Power Amplifier in 40-nm CMOS," *IEEE J. Solid-State Circuits*, vol. 48, no. 10, pp. 2323–2337, Oct. 2013.

[54]	D. Zhao and P. Reynaert, "A 40-nm CMOS E-Band 4-Way Power Amplifier With Neutralized Bootstrapped Cascode Amplifier and Optimum Passive Circuits," *IEEE Trans. Microw. Theory Tech.*, vol. 63, no. 12, pp. 4083–4089, Dec. 2015.

[55]	S. Moghadami, J. Isaac, and S. Ardalan, "A 0.2-0.3 THz CMOS Amplifier With Tunable Neutralization Technique," *IEEE Trans. Terahertz Sci. Technol.*, vol. 5, no. 6, pp. 1088–1093, Nov. 2015.

[56]	W. L. Chan and J. R. Long, "A 58-65 GHz Neutralized CMOS Power Amplifier With PAE Above 10% at 1-V Supply," *IEEE J. Solid-State Circuits*, vol. 45, no. 3, pp. 554–564, Mar. 2010.

[57]	M. S. Gupta, "Power gain in feedback amplifiers, a classic revisited," *IEEE Trans. Microw. Theory Tech.*, vol. 40, no. 5, pp. 864–879, May 1992.

[58]	H. Vahdati and A. Abdipour, "Generalization of Kurokawa's stability criterion considering the dynamic nonlinearities in microwave oscillators," in *2005 Asia-Pacific Microwave Conference Proceedings*, 2005, vol. 2, pp. 5 pp.-.

[59]	S. V. Thyagarajan, A. M. Niknejad, and C. D. Hull, "A 60 GHz Drain-Source Neutralized Wideband Linear Power Amplifier in 28 nm CMOS," *IEEE Trans. Circuits Syst. Regul. Pap.*, vol. 61, no. 8, pp. 2253–2262, Aug. 2014.

[60] M. Bassi, J. Zhao, A. Bevilacqua, A. Ghilioni, A. Mazzanti, and F. Svelto, "A 40-67 GHz Power Amplifier With 13 dBm and 16% PAE in 28 nm CMOS LP," *IEEE J. Solid-State Circuits*, vol. 50, no. 7, pp. 1618–1628, Jul. 2015.

[61] F. Vecchi *et al.*, "A Wideband Receiver for Multi-Gbit/s Communications in 65 nm CMOS," *IEEE J. Solid-State Circuits*, vol. 46, no. 3, pp. 551–561, Mar. 2011.

[62] C. H. Li, C. N. Kuo, and M. C. Kuo, "A 1.2-V 5.2-mW 20-30-GHz Wideband Receiver Front-End in 0.18- CMOS," *IEEE Trans. Microw. Theory Tech.*, vol. 60, no. 11, pp. 3502–3512, Nov. 2012.

[63] S. C. Tseng, C. Meng, C. H. Chang, C. K. Wu, and G. W. Huang, "Monolithic Broadband Gilbert Micromixer With an Integrated Marchand Balun Using Standard Silicon IC Process," *IEEE Trans. Microw. Theory Tech.*, vol. 54, no. 12, pp. 4362–4371, Dec. 2006.

[64] H. Jia, B. Chi, L. Kuang, and Z. Wang, "A W-Band Power Amplifier Utilizing a Miniaturized Marchand Balun Combiner," *IEEE Trans. Microw. Theory Tech.*, vol. 63, no. 2, pp. 719–725, Feb. 2015.

[65] K. Okada *et al.*, "A 60-GHz 16QAM/8PSK/QPSK/BPSK Direct-Conversion Transceiver for IEEE802.15.3c," *IEEE J. Solid-State Circuits*, vol. 46, no. 12, pp. 2988–3004, Dec. 2011.

[66] D. Fritsche, P. Stärke, C. Carta, and F. Ellinger, "A Low-Power SiGe BiCMOS 190-GHz Transceiver Chipset With Demonstrated Data Rates up to 50 Gbit/s Using On-Chip Antennas," *IEEE Trans. Microw. Theory Tech.*, vol. 65, no. 9, pp. 3312–3323, Sep. 2017.

[67] N. Sarmah *et al.*, "A Fully Integrated 240-GHz Direct-Conversion Quadrature Transmitter and Receiver Chipset in SiGe Technology," *IEEE Trans. Microw. Theory Tech.*, vol. 64, no. 2, pp. 562–574, Feb. 2016.

[68] S. Carpenter *et al.*, "A D-Band 48-Gbit/s 64-QAM/QPSK Direct-Conversion I/Q Transceiver Chipset," *IEEE Trans. Microw. Theory Tech.*, vol. 64, no. 4, pp. 1285–1296, Apr. 2016.

BIOGRAPHICAL SKETCH

Qian Zhong was born in Jiangsu, China on January 29th, 1990. He received B.S degree in Electronic Engineering from University of Electronic Science and Technology of China, China in 2012. He is currently working toward the Ph.D. degree in Electrical and Computer Engineering in the University of Texas at Dallas, USA. His research interests are high-frequency building blocks and Millimeter-Wave and Terahertz receiver and transmitter design.

<center>**CURRICULUM VITAE**</center>

EDUCATION

Ph.D, Electrical Engineering,   **2013-2018**

- The University of Texas at Dallas, Dallas, TX

- GPA:3.9/4.0

B.S, Electrical Engineering   **2008-2012**

- University of Electronic Science and Technology of China, China

- GPA:3.7/4.0

WORK EXPERIENCES

Texas Instrument, Dallas, TX   **May to Aug 2016**

- Investigate LO chain quadrature phase mismatch and quadrature LO generation

NXP Semiconductor, Chandler, AZ   **Jan to May 2018**

- In mm-wave CMOS phase modulated automotive radar group

- Design LNA, PA for phase modulated radar in CMOS

PUBLICATIONS

- Q.Zhong, W.Choi, K.K.O, "Terahertz RF Front End Employing Even Order Subharmonic MOS Symmetric Varactor Mixers in 65nm CMOS for Hydration Measurements at 560 GHz Communication,"*2018 Symposia on VLSI Circuits (VLSI)*, June 2018.

- Q.Zhong, Z.Chen, N.Sharma, S.K Shattry,W.Choi, K.K.O, "300-GHz CMOS QPSK Transmitter for 30-Gbps Dielectric Waveguide Communication,"*IEEE*

Custom Integrated Circuits Conference (CICC), April 2018.(***Best Student Paper Nominee***)

- Q.Zhong et al, "CMOS Terahertz Receivers,"*IEEE Custom Integrated Circuits Conference (CICC)*, April 2018.(***invited***)

- Q.Zhong, W.Choi, C.Miller, R.Henderson, K.K.O, "A 210-to-305GHz CMOS Receiver for Rotational Spectroscopy,"*IEEE International Solid-State Circuits Conference (ISSCC)*, January 2016.

- Q.Zhong, W.Choi, N.Sharma, Z.Ahmad, J.P.McMillan, C.F.Neese, F.C.Delucia, K.K.O, "225-280 GHz receiver for rotational spectroscopy,"*Radio Frequency Integrated Circuits Symposium (RFIC)*, May 2016.

- N.Sharma Q.Zhong, Z.Chen, W.Choi, J.P.McMillan, C.F.Neese, F.C.Delucia, K.K.O, "225-280 GHz transmitter for rotational spectroscopy,"*VLSI Technology, 2016 IEEE Symposium on (VLSI).*

- N.Sharma, J.Zhang, Q.Zhong, W.Choi, J.P.McMillan, C.F.Neese, F.C. DeLucia, K.K.O, "85-to-127 GHz CMOS Transmitter for Rotational Spectroscopy,"*IEEE Custom Integrated Circuit Conference (CICC)*, September 2014.

- J.Zhang, N.Sharma, W.Choi, D.Shim, Q.Zhong, K.K.O, "85-to-127 GHz CMOS Signal Generation Using a Quadrature VCO With Passive Coupling and Broadband Harmonic Combining for Rotational Spectroscopy" *IEEE Journal of Solid-State Circuits(JSSC)*, September 2014.